Fakultät für Chemie

Der Technischen Universität München

Max-Planck-Institut für Biochemie

Abteilung für Molekulare Strukturbiologie

The nanoscale architecture of the mouse rod outer segment elucidated by cryo-electron tomography

Matthias Pöge

Vollständiger Abdruck der von der Fakultät für Chemie der Technischen Universität München zur Erlangung des akademischen Grades eines Doktors der Naturwissenschaften (Dr. rer. nat.) genehmigten Dissertation.

Vorsitzender

Prof. Dr. Johannes Buchner

Prüfer der Dissertation

1. Hon.-Prof. Dr. Wolfgang Baumeister
2. Prof. Dr. Matthias Feige

Die Dissertation wurde am 18.03.2021 an der Technischen Universität München eingereicht und durch die Fakultät für Chemie am 27.05.2021 angenommen.

Abstract

Rod photoreceptor cells are responsible for vision in dim light. Phototransduction, the process converting a light stimulus into a neuronal signal, is triggered when the visual pigment Rhodopsin (Rho) absorbs a single photon. Rho resides within the rod outer segment (ROS) which is a stack of equally shaped and tightly packed membrane disks. Rho occupies around 50% of the disk membrane area in ROS. Consequently, the high density of Rho within the membrane architecture of ROS increases the probability of photon capture, linking the remarkable light sensitivity of ROS to their ultrastructural organization. While the biochemistry of phototransduction is well established, the formation and maintenance of the ROS disk stack is poorly understood. In this thesis, the fundamental questions about the nanoscale architecture of ROS are addressed by cryo-electron tomography (cryo-ET).

Initially, a novel cryo-preparation workflow of ROS was established, followed by the characterization of the ROS membrane architecture. Two key features were identified: (i) the close stacking of membrane disks and (ii) the high membrane curvature at disk rims. The close stacking of membrane disks was further investigated with the tomographic data suggesting the existence of molecular connectors between disks. These connectors were then picked with a customized segmentation software and statistically analyzed. The results indicated two distinct types of connectors: a short, abundant species at the disk rim and longer, scarcer connectors in the disk interior. Based on literature data, these were hypothesized to be GARP2 and PDE6, respectively. A subsequent control experiment, however, failed to confirm this. Furthermore, numerous cytosolic densities were observed in ROS tomograms and studied by subvolume averaging. The obtained low-resolution averages revealed no structural information, likely due to the small size, flexibility, and heterogeneity of the proteins.

In the last part of this thesis, the high membrane curvature at disk rims is addressed. It is organized by PRPH2-ROM1 tetramers forming a continuous scaffold of three interconnected rows along the outer disk periphery. The tooth-shaped PRPH2-ROM1 tetramers are anchored by two diverging domains inside the membrane followed by a globular domain inside the disk lumen. The luminal domain seems to facilitate the assembly of the disk rim scaffold by rendering the binding interface between tetramers within the rows and by cross-linking neighboring rows, likely by disulfide bonds. In summary, this thesis provides structural information of the ROS disk stack at unprecedented level of detail. It elaborates the understanding of the ROS organization and has implications for the pathological pathway of PRPH2 mutations leading to blindness.

Zusammenfassung

Stäbchenzellen erlauben uns das Sehen bei dämmrigen Lichtverhältnissen. Phototransduktion, als der Prozess welcher ein Licht- in ein Nervensignal umwandelt, wird ausgelöst, wenn das visuelle Pigment Rhodopsin (Rho) ein einzelnes Photon absorbiert. Rho kommt in den äußeren Segmenten von Stäbchenzellen vor (engl. Rod outer segments, ROS). ROS sind ein Stapel von gleichartig geformten und dicht gepackten Membrandisks. Rho besetzt etwa 50% der Membranoberfläche in ROS. Die resultierende hohe Rhodopsindichte innerhalb der ROS Membranarchitektur erhöht die Wahrscheinlichkeit der Photonenabsorption. Somit ist die bemerkenswerte Lichtsensitivität von ROS mit deren Ultrastruktur verbunden. Während die Biochemie der Phototransduktion gut aufgeklärt ist, bleibt die Bildung und Aufrechterhaltung von ROS größtenteils unbekannt. In dieser Doktorarbeit wird die ROS Architektur im Nanobereich mit Kryoelektronentomographie untersucht.

Zuerst wird eine neuartige Kryopräparationsmethode für ROS eingeführt. Daraufhin wird die ROS Membranarchitektur charakterisiert und dessen zwei maßgeblichen Merkmale identifiziert: (i) die dichte Stapelung der Membrandisks und (ii) die hohe Membrankrümmung an den Diskrändern. Die aufgenommenen Tomogramme suggerieren die Existenz von molekularen Konnektoren zwischen den Disk. Diese Konnektoren wurden mit einer angepassten Segmentierungssoftware lokalisiert und statistisch analysiert. Die Ergebnisse deuten auf zwei unterschiedliche Konnektorarten hin: eine kurze und häufig auftretende Spezies an den Diskrändern sowie längere und seltener vorkommende Konnektoren im inneren der Disks. In Übereinstimmung mit erhältlicher Fachliteratur wird vermutet, dass es sich dabei jeweils um GARP2 und PDE6 handelt. Darüber hinaus enthüllen die Tomogramme zahlreiche Dichten im ROS Zytosol. Diese wurden über die Mittelung von Subvolumen untersucht. Die erhaltenen, niedrig aufgelösten Mittelungen geben allerdings keine Strukturinformationen preis, vermutlich aufgrund der geringen Größe, Flexibilität und Heterogenität der Proteine.

Der letzte Teil der Arbeit befasst sich mit der Membrankrümmung an den Diskrändern. Diese wird von PRPH2-ROM1 Tetrameren organisiert, welche ein kontinuierliches Gerüst aus drei miteinander verbunden Reihen entlang der äußeren Diskperipherie bilden. Die zahnförmigen PRPH2-ROM1 Tetramere sind durch zwei divergierende Domänen in der Membrane verankert, gefolgt von einer globularen Domäne im Disklumen. Die luminale Domäne scheint den Zusammenhalt des Gerüsts zu ermöglichen, indem es die Bindungsfläche zwischen Tetrameren der selben Reihe darbietet. Zusätzlich vernetzt es benachbarte Reihen, vermutlich über Disulfidbrücken. Diese Arbeit liefert Strukturinformationen der ROS Architektur mit bisher unerreichtem Detailreichtum. Sie erweitert das Verständnis über die Organisation von ROS und hat Implikationen für den pathologischen Mechanismus bestimmter PRPH2 Mutationen die zu Blindheit führen.

Contents

List of figures

List of tables

1 Introduction

1.1 Rod outer segments and phototransduction

The human eye is a remarkably sensitive detector for light. Even a flash of one single photon is likely to be registered on our retina (Tinsley et al., 2016). The photoreceptor cells which are responsible for vision in dim light conditions are rods, highly specialized neurons with a strictly polarized structure (Figure 1 A) (Goldberg et al., 2016). The rod inner segment (RIS) performs all functions necessary for cell survival. On one side the RIS expose a synaptic terminal to downstream neurons and on the other side it is linked via the connecting cilium (CC) to the rod outer segment (ROS). ROS are the cellular compartment where the light stimulus is converted into a neuronal signal. This process, called phototransduction, is triggered when a photon is absorbed by the visual pigment rhodopsin (Rho) (Palczewski, 2006).

ROS have a cylindrical shape and in mice, the model system used in this work, they have a diameter of 1.32 µm and a height of 23.8 µm (Nickell et al., 2007). They are composed of a pancake-like stack (Figure 1 A) of ~800 equally shaped and precisely spaced disks stacked along the ROS axis and are enveloped by the plasma membrane (PM). Each disk has a diameter of 1.27 µm (Nickell et al., 2007) and is composed of two parallel disk membranes (DM) connected at their periphery by a hairpin-like disk rim (DR). The disk membranes are interrupted by a single, straight and narrow gap spanning from the outer disk periphery ~90% of the distance to the center of the disk (Liang et al., 2004). This disk incisure (DI) is aligned on consecutive disks along the ROS axis creating a passageway for longitudinal diffusion (Makino et al., 2012) (Figure 1 A). Approximately 50% of the ROS disk membrane area is occupied by Rho (Palczewski, 2006). The tight packing of Rho within disk membranes in concert with the close stacking of disks, accommodates millions of copies of Rho in a single ROS, up to concentrations of 3 mM (Pugh et al., 2000). This remarkably high Rho concentration increases the odds of photon capture tremendously. Therefore, the elaborate membrane architecture of ROS is of great importance for the function and the extraordinary sensitivity of rods.

The biochemistry of phototransduction is well studied. Phototransduction is initiated when Rho absorbs a single photon triggering a conformational change in Rho and opening a pocket on its cytosolic side. This allows binding of the G-protein transducin (G_t) which in turn dissociates into two subunits. The α-subunit (Gα) stimulates the activity of phosphodiesterase 6 (PDE6) which hydrolyses cyclic-guanosine monophosphate (cG) to guanosine monophosphate (GMP). The locally reduced concentration of cG closes cyclic nucleotide-gated cation channels (CNGC) in the ROS PM. This stops the influx of calcium ions (Ca^{2+}), hyperpolarizes the rod cell and culminates in a signal to the visual cortex. This is followed by the termination of phototransduction. It starts with the rhodopsin kinase (RK) phosphorylating cytosolic residues of Rho which allows arrestin (Arr) to cap the G_t binding pocket of Rho. Additionally, guanylyl cyclase (GC) restores the cG level resulting in the reopening of CNGCs which ultimately resets the ROS into its ground state (Figure 1 B). The whole process is more complex than explained here. It is regulated by several other proteins and its response is also modulated by the Ca^{2+} concentration. A more detailed description can be found in (Pugh et al., 2000). Important to note is that most of these proteins are either transmembrane or membrane-associated proteins. Therefore, successful encounters between them require lateral diffusion along the disk membrane surface which is of vital importance for the efficiency of phototransduction in the narrow and crowded membrane environment of the ROS disk stack (Pugh et al., 2000).

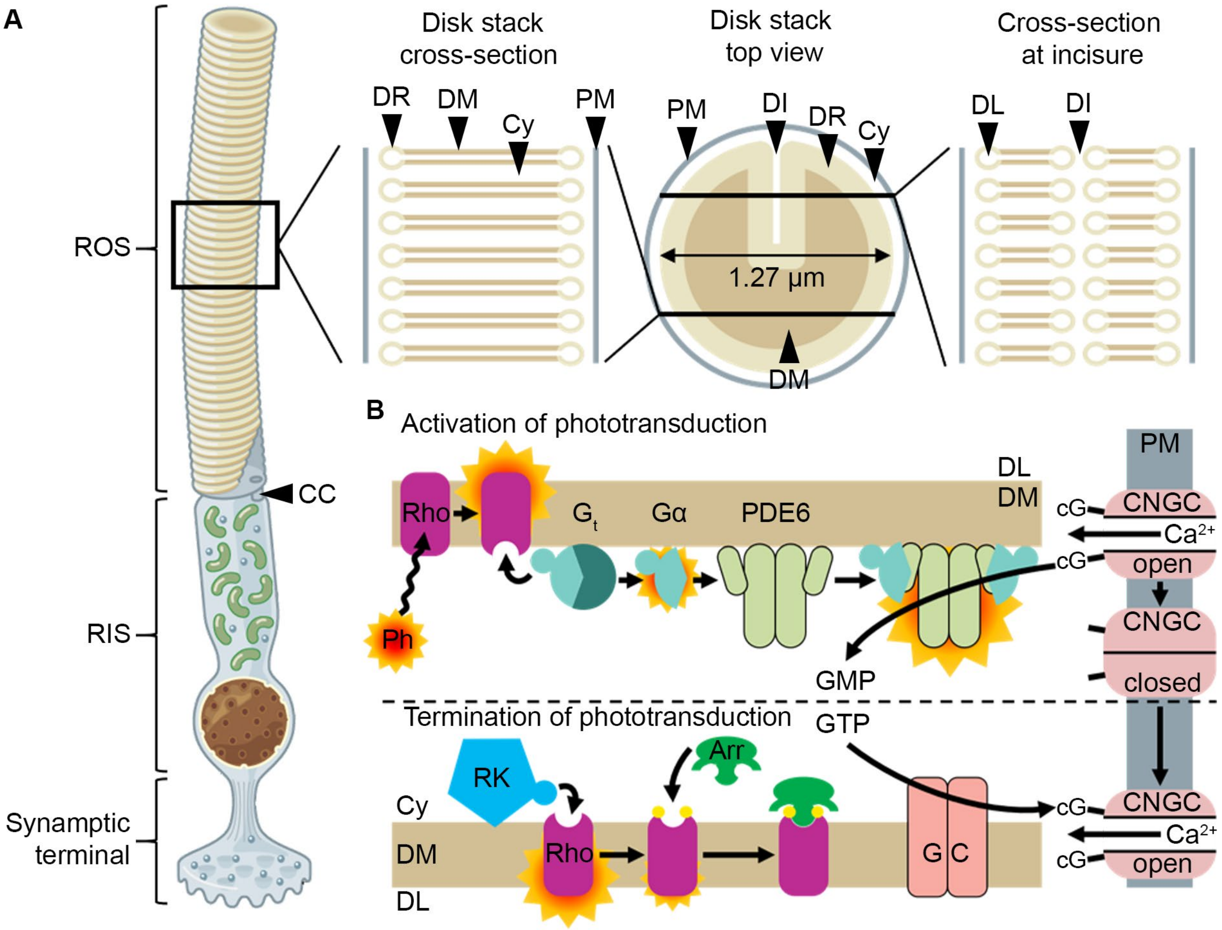

Figure 1: Sketch of a rod cell and phototransduction in the rod outer segment.
A) Sketch of a rod photoreceptor cell (left panel, britannica.com/science/rhodopsin). The rod inner segment (RIS) performs all vital cell functions and the rod outer segment (ROS) houses a stack of membrane disks within which phototransduction occurs. The organization of the disk stack is shown in the right panel. It is composed of equally shaped and precisely spaced disks, enveloped by the plasma membrane (PM). Each disk consists of two parallel disk membranes (DMs) surrounded by a hairpin-like disk rim (DR). DMs are interrupted by the disk incisure (DI). The disk lumen is indicated by DL and the cytoplasm by Cy. The sketch is not drawn to scale. **B)** Activation and termination of phototransduction in ROS. Rhodopsin (Rho) is activated by absorption of a photon (Ph) which allows transducin (G_t) to bind and to dissociate. The G_t α-subunit (Gα) stimulates the activity of phosphodiesterase 6 (PDE6) which hydrolyses cyclic-guanosine monophosphate (cG) to guanosin monophosphate (GMP). The lower cG concentration closes cyclic nucleotide gated cation channels (CNGC) in the PM stopping the influx of calcium ions (Ca^{2+}) and initiating the neuronal signal. To terminate phototransduction, the rhodopsin kinase (RK) phosphorylates Rho, which allows Arrestin (Arr) to cap the G_t binding pocket of Rho. Additionally, the guanylyl cyclase (GC) converts guanosine triphosphate (GTP), restoring the initial level of cG and CNGCs are reopened. The scheme is a simplified version adapted from (Pugh et al., 2000). Regulatory proteins and modulation by Ca^{2+} concentration were ignored.

The overall ultrastructure of ROS was described decades ago by conventional electron microcopy (Sjöstrand, 1949, 1953). However, its organization on the molecular level remained largely elusive. Previous studies suggested that disk stacking may be assisted by continuity of neighboring disk membranes (Robertson, 1965) while others indicated the existence of molecular connectors between adjacent disks as well as between disk rims and the PM. Still, the results obtained by different groups with various methods remain controversial (Goldberg et al., 2016). Early electron microscopy (EM) studies identified a molecular assembly at disk rim referred to as terminal loop complex (Corless et al., 1987) which was proposed to enforce high membrane curvature. This complex, composed of a crescentic density along the disk perimeter inside the disk lumen, is linked by a transmembrane component to intraloop densities which, in turn, connect neighboring disk rims. The complex appeared to form a 2D lattice surrounding the two disk membranes. It was hypothesized that one component of the complex is a large membrane protein localized at disk rims (Papermaster et al., 1978) which was later identified as the photoreceptor cell specific ATP-binding cassette transporter (ABCA4). Today it is known that ABCA4 is of no structural importance for ROS (Weng et al., 1999) but required for the long-term viability of the retina (Tsybovsky et al., 2013).

Further experiments identified two other proteins which are abundant in ROS and exclusive localized to disk rims: peripherin-2 (PRPH2) (Molday et al., 1987) and ROS membrane protein 1 (ROM1) (Bascom et al., 1992). Both are small transmembrane proteins of the tetraspanine family and are homologues of one another (Kevany et al., 2013). Non-covalent homo- and hetero-tetramers of these two proteins are the minimal stable subunits purified from native source, which assemble into oligomers stabilized by disulfide bonds(Goldberg et al., 1996; C. J. R. Loewen et al., 2000). Upon reconstitution into lipid membranes, the tetramers induce membrane curvature *in vitro* (Kevany et al., 2013) however, the mechanism of membrane curvature formation at the disk rim remains unclear.

It has been shown that PRPH2 interacts with glutamic acid-rich proteins (GARPs) (Poetsch et al., 2001). The three GARP isoforms present in ROS are encoded by the *CNGB1* gene (Colville et al., 1996): the β-subunit of the CNGC and the alternatively spliced proteins GARP1 and GARP2. The CNGC is a transmembrane protein at the PM, whereas GARP1 and GARP2 are soluble proteins which are associated with membranes under physiological conditions (Körschen et al., 1999). All three GARPs are exclusively localized to disk rims or the adjacent PM (Körschen et al., 1999) and exhibit a large degree of intrinsic disorder (Batra-Safferling et al., 2006).

Based on these results, a model for the organization of the ROS disk stack was proposed (Batra-Safferling et al., 2006). PRPH2 and ROM1 are expected to organize the disk rim curvature by an unknown mechanism. Due to the interactions of PRPH2 with GARPs, it was hypothesized that CNGCs form connectors between PM and disk rims while GARP2 forms connectors between adjacent disk rims (Batra-Safferling et al., 2006). This hypothesis is supported by data from mice lacking all three GARP isoforms. They develop a phenotype with misaligned and irregularly shaped ROS disks suggesting the importance of GARPs for the structural integrity of ROS (Y. Zhang et al., 2009).

ROS, especially of mice, have been extensively studied in the past. On the one hand, because a broad library of naturally occurring or genetically engineered mouse strains with vision-related disorders are available. Due to similarity of these mouse models to human physiology and anatomy, they have direct relevance for the understanding of human disease (Chang et al., 2005; Won et al., 2011). On the other hand, because ROS are an easily accessible, prototypical system to study G-protein mediated signal transduction as fundamental process in biology (Pugh et al., 2000). ROS are supposed to fulfill only one single function: phototransduction. Therefore, ROS contain only a small number of highly concentrated proteins of structural and functional importance. Several decades of research, have identified, localized and quantified the most abundant of these proteins (Table 1). Additionally, high-resolution information is available for several proteins involved in the signal cascade of phototransduction (Rho: (Teller et al., 2001), G_t: (Gao et al., 2019), PDE6: (Gulati et al., 2019), Arr: (Kang et al., 2015), RK: (Singh et al., 2008)).

Despite all this knowledge, two pressing questions remain unanswered: (i) How does phototransduction occur within ROS? The efficiency of phototransduction is depended on diffusion processes in the narrow and crowded environment of ROS, yet, in mice ROS the peak of the ROS light response is reached after 250 ms and the whole system set back to the ground state in 500 ms for dim flashes (Ingram et al., 2016). (ii) How is the ROS ultrastructure organized and maintained on the molecular level? Many mutations perturb ROS architecture and induce various vision disorders, including blindness of millions of people worldwide, while the underlying pathological pathways are poorly understood (Boon et al., 2008; Daiger et al., 2013). These questions could not previously be answered due to the lack of high-resolution information of the molecular landscape of ROS in a close-to-native state. This gap of knowledge can be addressed by cryo-electron tomography.

Table 1: List of important and most abundant proteins in ROS.
This lists only proteins required for the understanding of this work. For a more complete list, the reader is referred to (Kwok et al., 2008). In the location column, DM denotes disk membrane, Cy cytosol, PM plasma membrane and DR disk rim. If not otherwise indicated, the values were taken from (Pugh et al., 2000).

Protein	**Abr.**	**Location**		**MW (kDa)**	**Ratio of Rho to protein**	**Density per disk area (µm^{-2})**
		Where	**How**			
			Phototransduction proteins			
Rhodopsin	Rho	DM	transmembrane	36	1	25000
Transducin	G_t	DM	associated	81	10	2500
Posphodiesterase 6	PDE6	DM	associated	215	50	500
Arrestin	Arr	Cy	cytosolic	48	8	-
Rhodopsin kinase	RK	DM	associated	65	500	500
Guanyly cyclase	GC	DM	transmembrane	224	500	50
Cyclic nucleotide-gated cation channel	CNGC	PM	transmembrane	606	1700	500
			Potential structural proteins			
ATP-binding cassette transporter A4	ABCA4	DR	transmembrane	260	>300[1]	-
Peripherin-2	PRPH2	DR	transmembrane	39	~90[2]	-
ROS membrane protein 1	ROM1	DR	transmembrane	37	~90[2]	-
Glutamic acid-rich protein 1	GARP1	DR	associated	65	1000[3]	-
Glutamic acid-rich protein 2	GARP2	DR	associated	32	50[3]	-

[1] (Papermaster et al., 1978), [2] (Goldberg et al., 1996), [3] (Batra-Safferling et al., 2006)

1.2 Electron Microscopy and imaging of biological materials

If we want to understand how something works, the easiest way is to just look at it. However, if we are interested in life that becomes difficult because the most fundamental life processes are happening at the molecular level and are not resolved by our eyes. Therefore, scientists developed devices which allow to generate magnified images of our surrounding world – microscopes. Light microscopy (LM) has revolutionized our understanding of nature by revealing the world of cells to us ("Milestones in Light Microscopy," 2009). However, the theoretical resolution limit of a microscope is, as a rule of thumb, half the wavelength of the radiation used for imaging. In the case of visible light, the minimal wavelength is in the order of 400 nm, therefore restricting the theoretical resolution of conventional LM to around 200 nm.

Unfortunately, the magic of life happens at the molecular level and most key players there are at least two orders of magnitude smaller. The invention of electron microcopy (EM) opened new avenues in life sciences (Ruska, 1980). The principles of optics are largely the same for LM and EM. The fact that electrons are charged particles with a mass allows to tune the wavelength with the acceleration voltage. For example, electrons accelerated by a voltage of 300 kV have a wavelength around 2 pm therefore promising high spatial resolution (Williams et al., 2009).

There are two main types of EM: Scanning electron microscopy (SEM) and transmission electron microscopy (TEM). In SEM, the sample is scanned with a condensed electron beam and back-scattered or secondary electron are detected (Zhou et al., 2006) which can be used to visualize the topography of a conductive sample. Alternative approaches for volume imaging are serial sectioning- and serial milling- and block face imaging. Here, either a diamond knife or a focused ion beam (FIB) is used to consecutively remove a layer of the bulk material and the new block face is imaged by a scanning electron microscope. Block face imaging recovers 3D information of a bulk sample (Briggman et al., 2012). However, resolution is limited by the size of the electron probe and the dimensions of the volume in which electrons interact with the sample (Zhou et al., 2006). Thus, the resolution in SEM is typically restricted to several nanometers.

This work is primarily focused on the other type of EM, namely TEM. In a transmission electron microscope, the beam is operated in bright-field mode to illuminate an extended area on the sample and the transmitted electrons are projected onto a detector (Williams et al., 2009). Unfortunately, several factors, caused by the strong interaction of high-energy electrons with matter, complicate the TEM investigations of biological samples:

1. The TEM column must be kept at ultra-high vacuum, typically below 10^{-10} bar, to prevent the scattering of all electrons by gas molecules before reaching the sample.
2. The samples must be thin enough to allow electron transmission.
3. The incident electrons damage the sample which successively disrupts the sample structure.
4. Irradiation induces sample drift which distorts the image.

Decades have been spent to establish preparation techniques to stabilize the sample for the extreme conditions of the microscope column, while limiting distortions of the sample itself. Moreover, special data collection and processing methods have been developed to minimize and deal with the damage introduced by the electron beam.

1.2.1 Preparation of biological samples for transmission electron microscopy

The simplest way to examine isolated macromolecular complex or virus by TEM is negative staining. For this, the sample is applied to an EM-grid, a small metal grid (Ø ≈ 3 mm) with an additional support material (Passmore et al., 2016). Then a solution of heavy metal ions is added which coat the structure of interest upon drying (Gallagher et al., 2019; Orlova et al., 2011). TEM imaging of more complex samples like cells is complicated by their high water content, which would instantaneously evaporate in the low column pressure and destroy the very structure under investigation. The classical workaround is to cross-link the sample, stain membranes with heavy metals and replace the water by a plastic resin (Winey et al., 2014). This 'fixed' sample is stable in the extreme conditions of the microscope column, however, the replacement of water with a resin disrupts the cellular ultrastructure. Due to the denaturing character of these traditional methods the resolution on the molecular level is heavily restricted.

Better structural preservation can be achieved with methods which transition the water directly into a solid state. Unfortunately, simple freezing is not applicable, as the volume of water expands upon ice crystal formation and severely damages the cellular ultrastructure. When the sample is cooled below -135°C, however, at cooling rates greater than 10^4 K/s, molecular motion is slowed down so quickly that water molecules literally have no time to form crystalline ice. The sample becomes vitrified, trapping it in a glass-like, fully hydrated, close-to-native state which avoids artifacts typically observed in conventional sample fixation techniques. To obtain vitreous ice in EM, cryo-preparation methods have been developed (Passmore et al., 2016), the most straight-forward being plunge-freezing (Adrian et al., 1984). For this, the sample is applied to an EM-grid and the excess of buffer is blotted away with a filter paper leaving a thin film of the sample on the grid support. Then the grid is plunged it into a cryogen, typically ethane, propane, or mixtures thereof, cooled close to its freezing temperature by liquid nitrogen (Tivol et al., 2008). Plunge-freezing is readily implemented for isolated protein complexes, viruses, small bacteria, cellular organelles or small eukaryotes as long as the sample thickness is below 5 µm (Dubochet et al., 1988). Thicker samples like most eukaryotic cells or tissues do not permit fast enough cooling rates to allow full vitrification. In this case, specimens with a thickness up to 200 µm (McDonald et al., 2010) can be prepared by high-pressure freezing (HPF). In the very moment of freezing, a pressure of ~2000 bar is applied to the sample which counteracts the volume expansion associated with ice crystal formation, therefore, suppressing their nucleation and growth (Moor, 1987).

A challenge for vitrified biological samples is that from the moment of freezing, they must not be warmed above -140°C, the glass-transition temperature of water and are therefore stored in liquid nitrogen, at -196°C. Furthermore, special specimen holders and devices had to be designed for imaging and manipulation of the cryo-samples in otherwise warm microscopes. Especially tricky are transfers in and out of the high vacuum of electron microscopes: the sample can warm up, its cold surface can be contaminated by ice crystals derived from humid air and the sample can be damaged as consequence of the handling with tweezers.

Another prerequisite for TEM samples is that they must be thin enough to allow for electron transmission. The obtainable resolution scales with thickness of the biological material and samples thinner than 500 nm are required for high-resolution data acquisition (Plitzko et al., 2019). This is only the case for isolated macromolecular complexes and viruses while most cellular samples need additional thinning. ‘Fixed’ samples can be cut into thin sections with a diamond knife in an ultramicrotome and for cryo-preparations, cryo-ultramicrotomes are available. However, the mechanical cutting process compresses the sample while knife marks and crevices are introduced (Al-Amoudi et al., 2005). These artefacts can make tomographic data acquisition a challenging or even a pointless task and cannot be compensated for by computational processing. A less artifact-prone approach is the use of dual-beam cryo-focused ion beam and scanning electron microscope (cryo-FIB/SEM). For this technique, plunge-frozen samples are first coated with a conductive layer of metallic platinum which enhances the imaging capabilities of the microscope and eases the identification of target objects, like cells. After a region of interest is localized, the FIB is shooting Gallium ions (Ga^+) at a shallow angle onto the sample to ablate material above and below the region of interest while the progress of FIB-milling is monitored by SEM imaging (Marko et al., 2007). The remaining thin sheet of the biological material supported on both sides by bulk material is referred to as a lamella. To prevent ion beam erosion at the front face of the lamella and to assure homogeneous thinning, a protective layer of organometallic platinum is deposited on the sample prior to FIB-milling. This method has been shown to cause no devitrification or other artifacts in vitrified biological samples (Marko et al., 2006).

If a specific site or a rare structure is targeted, correlative light and electron microscopy (CLEM) can be used to guiding FIB-milling (Arnold et al., 2016; Rigort et al., 2010). For this, the target site is labelled by a fluorescent marker and the images obtained with a cryo-confocal fluorescence light microscope are correlated with FIB and SEM images allowing for site-specific FIB-milling. Moreover, thicker specimen, like HPF samples, require special milling procedure: after the target site has been identified, a thick slice of material is cut from the bulk sample, lifted out by a cryo-gripper and placed in a new holder where the milling to the electron-transparency is completed (Schaffer et al., 2019). However, the lift-out methodology is still a technical challenge and very time-consuming compared to on-grid lamella milling (Mahamid et al., 2015).

1.2.2 Imaging in a transmission electron microscope

Once a suitable sample for TEM data acquisition is prepared, the question arises how the image is formed in TEM. Due to the large depth of field of the transmission electron microscope, TEM images are 2D projections of the sample convoluted with the point spread function (PSF) of the microscope. Due to the convenient representation and fast computation speed of modern algorithms, image formation and processing are often performed in Fourier space (Erickson et al., 1971). Any image can be decomposed in a set of trigonometric waves with certain directionalities and wavelengths. The wavelengths are often referred to as spatial frequencies and their possible values are dictated by the image and the pixel size. Furthermore, each wave is characterized by an amplitude and a phase shift. Low spatial frequency components, meaning waves with large wavelength, carry the information about the overall shape of the image while high spatial frequencies encode the fine details. When image formation is treated in Fourier space, the convolution of the projection with the PSF is reduced to a product of the Fourier transforms (FTs) of both entities. The FT of the PSF is called contrast transfer function (CTF) which modulates the amplitudes of the Fourier components in the FT of the projection. In a perfect microscope, the image of a point would simply be a point without blurring. This translates into point-shaped PSF and its FT, the CTF, being unity over all spatial frequencies, meaning that all spatial frequencies are perfectly transferred into the image.

Unfortunately, the imaging capabilities of transmission electron microscopes are far from perfect (Lenz, 1971). This is partially caused by imperfections in the electromagnetic lenses of the microscope and in the case of biological samples, it is also closely related to the mechanism of contrast formation. To understand the latter, the interactions of electrons with the sample must be considered. Of the incident electron wave, a fraction will be transmitted through the sample while not interacting with it. For those electrons interacting with the sample, two outcomes exist: either they are elastically scattered, meaning they are deflected at an angle without losing energy, or they are scattered inelastically by transferring some of their energy to the sample (Reimer, 1984). As a rule of thumb, the heavier an atom, the more likely it is to scatter and the stronger it will scatters the electron. From these interactions arise two main types of contrast formation. In the case of negative staining or ‘fixed’ samples, heavy metal ions which scatter electrons strongly, leading to fewer electrons being detected below stained regions. Due to the regional variation of transmission and the large degree of scattering, the amplitude of the transmitted electron wave is significantly changed, and the resulting contrast is known as amplitude contrast.

This work, however, focuses on unstained, vitrified biological samples which typically contain weak scatterers and are composed of elements with similar low atomic number. In this case, the largest fraction of the incident electrons is transmitted through the sample while only a small amount is scattered. Hence, the amplitude of the incident electron wave is not significantly changed when passing through the sample. Contrast is still generated because scattered and unscattered waves have a phase shift with respect to one another. This phase shift is dependent on the scattering angle and determines whether the waves interfere constructively or destructively on the detector. This results in an oscillatory behavior of the CTF where the microscope’s defocus determines the ”speed” of the oscillation. Here, defocus is the distance between the imaging plane and the actual focal plane. Additionally, the CTF of a TEM has an envelope which drops to zero towards higher spatial frequencies causing fine details to blur in the image. The steepness of that falloff is dependent on microscope properties, mainly the lens aberrations and the defocus (Orlova et al., 2011). If a TEM is operated at zero defocus, meaning in focus, the CTF envelop drops slowest and preserves the high-resolution image details best. However, the ‘slow’ sine-like CTF oscillations quench contrast transfer of the lowest frequencies generating low-contrast images that cannot be interpreted. Traditionally, this problem is solved by defocusing the microscope leading to faster CTF oscillations allowing for more signal transfer of the low frequency at the cost of high-resolution information. The use of phase plates can circumvent this problem (Danev et al., 2017). They introduce an additional phase shift, ideally of π/2, between the scattered and unscattered waves which converts the sine-like CTF oscillations into a cosine. This permits full transfer of the lowest spatial frequencies and generates high contrast images even when the microscope is operated in focus (Danev et al., 2014).

It is important to note that only single elastically scattering events contribute positively to image formation of thin, unstained biological samples. Electrons which were inelastically scattered or scattered multiple times contribute to the background noise. The negative influence of inelastically scattered electrons can be prevented by employing energy filters. They can be considered as magnetic prisms where electrons with different energy are deflected on distinct paths (Trinick et al., 1987). The path of unscattered and elastically scattered electrons with their full 300 keV of initial energy are focused through a slit while inelastically scattered electrons with lower energy are filtered out at the aperture of the energy filter. The noise contributed by multiple elastic scattering events cannot be filtered out. The probability of these events, however, decreases with reduced sample thickness, again emphasizing the importance of thin sample preparation for high quality TEM data (Koster et al., 1997).

Additionally, vitrified biological samples are very sensitive to radiation damage. The energy introduced by inelastically scattered electrons imposes changes to the structure of the sample. First, the fine image details deteriorate, and between electron doses of 100 $e^-/Å^2$ and 200 $e^-/Å^2$ the formation of large bubbles completely disturbs the image (Glaeser, 2016). For this reason, the electron dose applied to the region of interest must be limited. Low-dose software routines have been implemented which allow to perform the necessary focusing and tracking steps outside of this region, minimizing the structural perturbation in the actual acquisition area (Cheng et al., 2016).

On top of the radiation damage, the illuminated area moves locally and globally upon irradiation with the electron beam (Brilot et al., 2012). Classical electron detectors based on CCD camera chips generate a single image per exposure. Therefore, CCD cameras average over the sample movement, blurring the image (Krivanek et al., 1993). These problems were addressed after the introduction of direct electron detectors (DEDs), a new generation of cameras (McMullan et al., 2016). In comparison to CCD cameras, DEDs detect electrons more efficient with improved signal-to-noise ratio (SNR), particularly at low electron dose. Additionally, the fast read-out speed of DEDs allows the recording of movies during the exposure time and the counting of electrons which is beneficial for the camera performance (McMullan et al., 2016). DEDs permit to further enhance the image quality with additional processing steps after data acquisition. The movies allowed to quantify the radiation damage as result of the accumulated electron dose (Grant et al., 2015). So-called dose-filtering is now routinely applied to down-weight or remove corrupted signal components on a frame-by-frame basis. Furthermore, images can be corrected for beam-induced motion by bringing the movie frames into register and averaging them (Li et al., 2013). The combined effects of dose-filtering and motion correction with the better performance of DEDs revolutionized the field of cryo-EM (Ripstein et al., 2016).

But what is the best resolution that can be obtained for vitrified biological sample? Traditionally, the resolution limit was defined at the spatial frequency of the first CTF node because of the inconsistent contrast transfer beyond it (Scherzer, 1949). Today, however, it is possible to correct for the distortions introduced by the microscopes CTF. Its modulations can be observed as Thon rings in the power spectrum of the recorded image (Thon, 1966). Thus, the CTF parameters can be estimated and used to deconvolute the image in a processing step called CTF-correction (K. Zhang, 2016). Even so, in projection images of vitrified biological samples with CTF-correction, large protein complexes are only resolved as blobs while their high-resolution features are hidden below the high noise levels.

Additionally, information is only obtained in the plane of the projection while all information perpendicular to it is lost (Plitzko et al., 2019). Still, cryo-EM allows the recovery of high-resolution 3D information of the sample, aided by specific data acquisition and processing steps.

1.2.3 Recovering 3D information from TEM data

There are two methods available to recover 3D information from the 2D projections obtained by TEM: Single particle analysis (SPA) and electron tomography (ET). SPA is only applicable if images contain many copies of repetitive objects in different orientation (Cong et al., 2010). First these objects must be selected and cropped from the noisy projection image (Figure 2 A). The set of subimages is then subjected to 2D classification which sorts out the different views of the objects, aligns them with respect to each other and then averages the subimages in the respective classes. The averaging of aligned subimages significantly enhances the SNR compared to the raw data and recovers some high-resolution information (Figure 2 A). Relative positions and orientations of the individual subimages are then determined with respect to a 3D reference. If they are brought into precise register, the projection images can be superimposed, and the resulting average contains 3D information at higher spatial resolution and SNR than the raw data (Figure 2 A). However, SPA is only applicable for isolated macromolecular complexes or certain viruses.

The emphasis of this project is on unique, pleomorphic structures like organelles or cells. Here, the 3D organization can be investigated using electron tomography (Plitzko et al., 2019). Single 2D images, even of very thin sections, are insufficient for a complete structural characterization. A cylinder oriented along its axis and a sphere appear similar in the projection as round objects (Figure 2 B). Only when rotating the point of view perpendicular to the cylinder axis and acquiring another projection, both can be distinguished from one another. In ET, the sample is rotated inside the TEM with respect to the electron beam and projection images are acquired from different angles in a tilt-series (Figure 2 B). Due to inaccuracies in the mechanical stage movements and the tracking routines, the images of the tilt-series must be aligned. Typically, gold fiducials are used for tracking, but if their introduction into the sample is not possible, patches of features can also be used (Mastronarde et al., 2017). The aligned tilt-series is then computationally reconstructed into a tomogram. Most commonly used is the weighted back-projection which reliably preserves the high-resolution information (Turoňová et al., 2016).

Unfortunately, several factors complicate ET in practice, particularly cryo-ET of vitrified biological samples (Plitzko et al., 2019). Their sensitivity to beam-induced damage already restricts the total electron dose between 50 $e^-/Å^2$ and 150 $e^-/Å^2$, dependent on the material and the details that are to be resolved. This low dose, however, must now be distributed over a series of projections. Therefore, the single images are recorded with even lower electron dose further reducing their SNR. Several tilt schemes have been developed with trade-offs between fast acquisition and least perturbed information at highest possible SNR (Wan et al., 2016). The unidirectional scheme, tilts directly from one angular extreme to the other. It is the fastest acquisition scheme, but it obtains the least disturbed data at high tilts where the increased sample thickness causes a low SNR. The bidirectional scheme acquires the tilt-series in two separate branches. The first branch starts a low tilt angle and walks up to the first angular extreme while the second branch completes the tilt-series to the other side. Here, information of the unperturbed structure is obtained at low angles and thus high SNR. However, the progressive sample damage during acquisition of the first branch complicates the alignment of both branches. The dose-symmetric tilt scheme combines best preserved information at highest possible SNR by starting at 0° and the ramping up to the angular extremes in a zig-zag manner. The extensive amount of stage movements makes it the slowest acquisition scheme (Hagen et al., 2017).

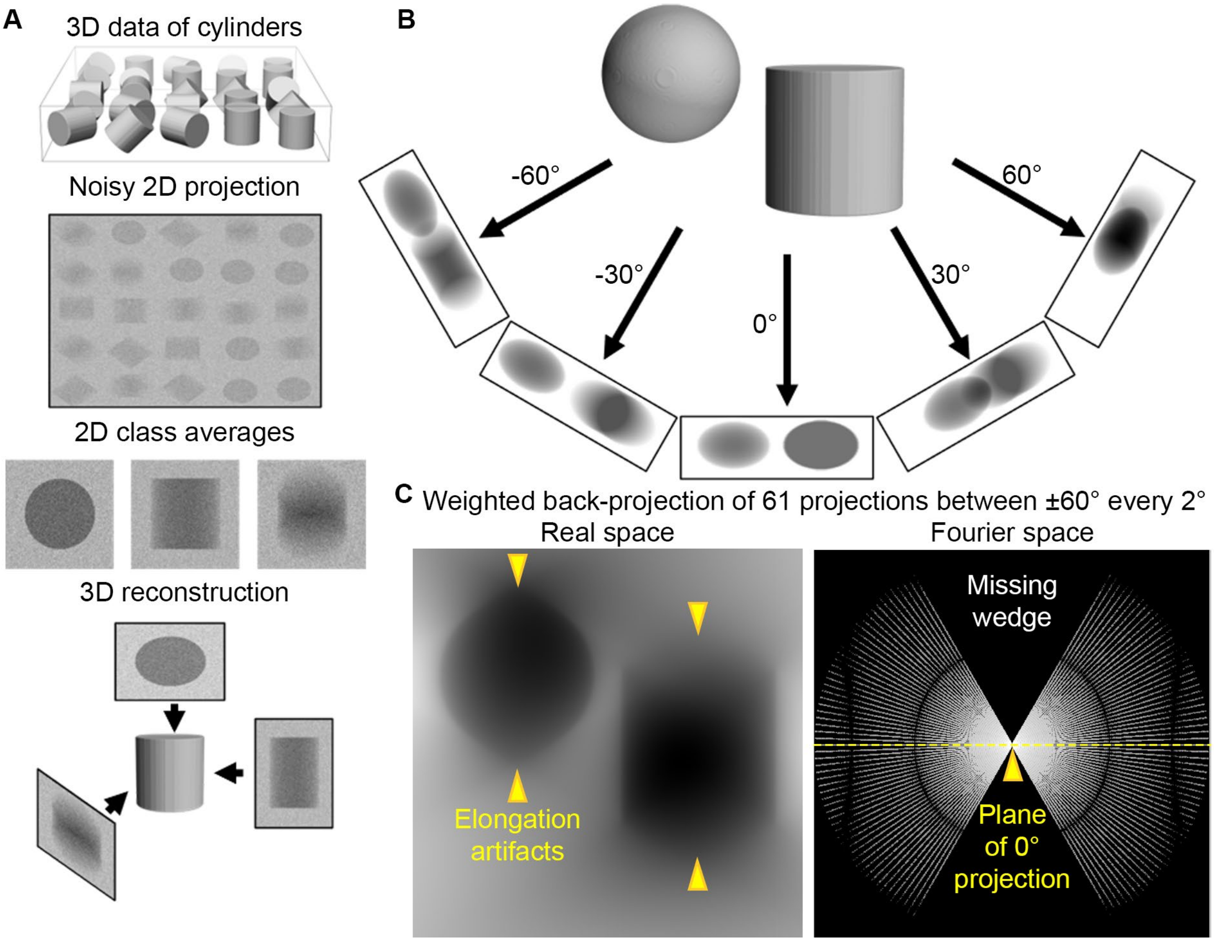

Figure 2: Recovering 3D information from projection data in cryo-EM.
A) Single particle analysis (SPA) is employed for multiple copies of identical objects captured in different orientations within projection images. Example here is a set of 3D cylinders with different orientations. In SPA, objects are picked in the noisy projection images and subimages cropped. 2D classification, sorts the different views, aligns and averages them. Eventually the shifts and rotations of the subimages are determined with respect to a 3D reference. Their superposition recovers 3D information at higher signal-to-noise ratio (SNR) than the raw data. **B)** ET can be used to elucidate the 3D arrangement of unique structures. The projections of a of cylinder along its axis and a sphere appear similar in the projection. In ET the sample is tilted with respect to the electron beam and projections acquired at different angles. The obtained tilt-series can be reconstructed into a tomogram. **C)** Central slice of the reconstruction of the object in B by weighted back-projecting of a tilt-series acquired between ±60° with a tilt increment of 2°. The incomplete sampling causes distortions in the reconstruction. Missing information is apparent in Fourier space where only slices are filled with a missing wedge of information between the two angular extremes. The plane of the 0° projection is indicated by a yellow dashed line.

Moreover, images cannot be obtained over the whole angular range of 180° because at high tilt angles the increased effective sample thickness and the geometry of the sample holder prohibit electron transmission. Therefore, typical acquisition schemes cover a tilt-range of ±60° with an angular increment between 0.5° and 5° (Plitzko et al., 2019). This incomplete sampling is a fundamental problem in cryo-ET. It becomes apparent in Fourier space where each projection fills only on slice of information in fan-like manner with a missing wedge of information between the highest collected tilts (Figure 2 C). This causes distortions in the reconstructed tomogram (Turoňová et al., 2016). Especially the missing wedge introduces elongation artifacts perpendicular to the plane of the 0° projection (Figure 2 C).

The high noise levels in tomograms of vitrified biological specimen make their interpretation particularly challenging. Raw tomograms are visualized as stacks of 2D slices where dense structure appear dark, translating into a low grey value. Several methods have been developed to suppress the high noise levels in the raw data, from simple convolution with a Gaussian to neural networks trained to distinguish structural features from noise (Buchholz et al., 2019). These denoising filters support the automated segmentation of cellular structures like membranes (Martinez-Sanchez et al., 2014), which in turn can be rendered and visualized in 3D. Methods based on thresholding can then segment smaller structures that form connectors between membranes (Lučić et al., 2016). Additionally, software tools have been established for unbiased, template-free detection and classification of transmembrane and membrane-attached densities (Martinez-Sanchez et al., 2020). In many cases, a specific object cannot easily be identified and selected by manual inspection of the data. If the molecular structure of the object is known, it can be localized within a tomogram by template matching. Cross-correlations are calculated between the template in different orientations and the tomogram (Böhm et al., 2000). The voxels (3D pixels) with the highest scores are potential positions and the angles of the highest scoring template a measure for the orientation of the object within the tomogram. However, due to the high noise levels in tomograms, this method can only be applied to large structures and visual inspection is required to remove false positives.

The most reliable approach to enhance the SNR and to account for image distortions caused by the incomplete sampling in cryo-ET is subvolume averaging of repetitive objects with different orientations (Wan et al., 2016). Similar to SPA, objects are picked within tomograms, either by hand or automated approaches, and 3D subvolumes are cropped. The shifts and rotations of these subvolumes are determined by comparing them to a common reference with a cross-correlation-like similarity metric. This information is then used to average the subvolumes which recovers high-resolution information. Furthermore, the different subvolume orientations fill in the missing information in Fourier space. The average is then used as reference for the next iteration. To avoid bias, the reference is typically low-pass filtered. Masks are used to constrain the alignment on the object without background or even to focus on a specific region within the object. Additionally, classification of 3D subvolumes can sort conformational or structural heterogeneity into more homogeneous subsets (Bharat et al., 2015). Several software packages are available for subvolume averaging with different functionalities, employing either deterministic or maximum-likelihood algorithms (Wan et al., 2016). Recently, a new generation of software tools use subvolumes as fiducials to further refine the alignment of the tilt-series. This approach promises to improve both the quality of the subvolume average and the tomogram itself (Tegunov et al., 2020).

Once a subvolume average is obtained, how can its resolution be estimated? Unlike X-ray crystallography, where the signal can be distinguished from the noise, in EM both are indistinguishably superimposed. The standard used in EM is the Fourier shell correlation (FSC) (Harauz et al., 1986). To calculate this, the data is split into two equivalent half-sets which are then processed separately, generating two independent averages or half maps. These are then correlated in Fourier space and the resulting normalized cross-correlation plotted against shells of equal spatial frequency. The 1D FSC curve is a measure of the consistency between the two half maps. As the overall shape of the two half maps is typically similar, the low frequencies correlate with the maximum value of one. The FSC drops towards higher spatial frequencies when the influence of noise causes deviations between the half maps. The gold-standard for the resolution estimate nowadays is the spatial frequency where the correlation drops to the value of 0.143 (Rosenthal et al., 2003), but also other more conservative thresholds like 0.5 are in use (Hrabe et al., 2012).

The list of disadvantages and technical challenges can seem daunting for cryo-ET. However, it is momentarily the only available technique to image the complex molecular landscape of cells, label-free, in a close-to-native state. This work is focusing on ROS. The full proteome of ROS has previously been quantified by mass spectrometry. Low to medium resolution fluorescence LM and immune histochemistry experiments were used to localize the proteins within ROS and in many cases structural biology methods provided high resolution information of isolated complexes. For a comprehensive understanding of ROS, however, it is necessary to image the unperturbed molecular sociology of ROS and to integrate this with existing data. This gap of resolution can be closed by cryo-ET.

1.3 Objective and aims

The efficiency of light reception in the rod outer segment (ROS) is linked to its elaborate membrane architecture. While the biochemistry of phototransduction is well established, the formation and maintenance of the ROS disk stack is poorly understood, due to the shortage of molecular resolution images of intact ROS. Previous data on the organization of ROS was obtained with various methods and the results of different experiments are contradicting each other. This thesis seeks to answer the fundamental questions about the nanoscale architecture of ROS with cryo-ET.

The first objective is to establish a novel cryo-preparation workflow of ROS for cryo-ET. This includes a gentle and fast ROS extraction procedure, thinning of ROS to electron transparency and TEM imaging at high spatial resolution with high contrast. Second objective is the characterization of the ROS membrane architecture. Two key features of the disk stack are identified: (i) the close stacking of membrane disks and (ii) the high membrane curvature at disk rims. The third objective is to understand the organization and maintenance of these key features on the molecular level. Connectors between membranes are segmented and the disk rims analyzed. The last objective was to study the organization proteins involved in phototransduction within the narrow and crowded environment of ROS. Altogether, this thesis provides images of the ROS disk stack at unprecedented level of detail and elaborates the understanding of its organization.

2 Materials and methods

2.1 Materials

2.1.1 Chemicals and consumables

Table 2: List of chemical and consumables with name of the corresponding supplier.

Chemical or consumable	Source
2-Chlor-acetamid (CAA)	Sigma
Anti-Rabbit IgG (Fc), AP Conjugate	Promega
AP substarte solution (NBT/BCIP, Pierce™)	Thermo Fisher Scientific
Calcium Chloride ($CaCl_2$)	Merck
Coomassie Protein-Assay buffer (Pierce™)	Thermo Fisher Scientific
EM-grids (Cu 200 mesh, holy carbon film R2/1)	Quantifoil
Ethane/Propane (37% ethane/63% propane)	Linde
Ethylenediaminetetraacetic acid (EDTA)	Merck
Glue (Single-use super glue gel)	Scotch
InstantBlue™	Abacam
Loading buffer (4X, Novex™ NuPAGE™ LDS loading buffer)	Thermo Fisher Scientific
Magnesium chloride ($MgCl_2$)	Merck
Methanol (MeOH)	Sigma
Microscope dish (clear bottom µ-dish, Ø = 35 mm, high)	ibidi GmbH
MOPS SDS running buffer (20X, Novex™ NuPAGE™)	Thermo Fisher Scientific
N-2-Hydroxyethylpiperazine-N’-2-ethanesulfonic acid (HEPES)	Biomol
PDE6A Polyclonal Antibody	Thermo Fisher Scientific
PDE6B Polyclonal Antibody	Thermo Fisher Scientific
Potassium chloride (KCl)	Merck
Protease Inhibitor (cOmplete, EDTA-free, tablets)	Merck
Protein lader (10 to 180 kDa, PageRuler™)	Thermo Fisher Scientific
PVDF/Filter Paper Sandwich (0.2 µm, 8.3x7.3 cm)	Thermo Fisher Scientific
SDS-PAGE gels (NuPAGE™ 4-12 % Bis-Tris gel, 1.0 mm, 10-Well)	Thermo Fisher Scientific
Skim milk powder	Sigma
Sodium cloride (NaCl)	Merck
Sodium deoxicholate (SDC)	Merck
Sodium deoxicholate (SDC)	Merck
Sodium dodecyl sulfate (SDS)	Roth
Thick filter paper (blotting filter papers, 2.5mm thick, 7.5x8.4 cm)	Thermo Fisher Scientific
NuPage™ Transfer buffer (20x)	Thermo Fisher Scientific

Tris base	Sigma
Tris(2-carboxyethyl)phosphin -hydrochlorid (TCEP)	Thermo Fisher Scientific
Tween 20	Merck
β-Actin Monoclonal Antibody	Cell Signaling Technology

2.1.2 Buffers

All buffers were produced using deionized water from a Milli-Q Plus Ultrapure Water Purifier.

Table 3: List of the buffers with the corresponding ingredients.

Buffer	Ingredients
Blocking buffer	TBS-T, 5% (wt/vol) skim milk powder
Mass spec compatible buffer I	25 mM Tris-HCl, 150 mM NaCl, 1% (vol/vol) SDC, 1% (vol/vol) SDS, 1x protease inhibitor
Mass spec compatible buffer II	100 mM Tris-HCl, 40 mM CAA, 10 mM TCEP, 1% (vol/vol) SDC
Ringer's buffer	10 mM HEPES, 130 mM NaCl, 3.6 mM KCl, 12 mM MgCl2, 1.2 mM CaCl2, 0.02 mM EDTA, pH 7.4
RIPA buffer	25 mM Tris-HCl, 150 mM NaCl, 1% (vol/vol) Triton X-100, 1% (vol/vol) SDC, 0.1% (vol/vol) SDS, 1x protease inhibitor
TBS-T	50 mM Tris-HCl, 150 mM NaCl, 1% (vol/vol) Tween 20
Transfer buffer	2x NuPage Transfer buffer, 10% (vol/vol) MeOH

2.1.3 Mouse strains

Three different mouse strains that were used for the work in this thesis:

1. Wild type (WT) C57BL/6J mice were purchased from the Jackson Laboratory (Jackson Laboratory, Bar Harbor, USA)
2. Female C57BL/6J mice were crossed with male C3H/HeOuJ. Latter are homozygous for the *rd1* mutation (Chang et al., 2002). Consequently, the first-generation offspring (B6C3HF1/J) was heterozygous for the *rd1* mutation and will be referred to as *rd1/+* mice in this thesis. The breeding was carried out by the animal facility of the Max Planck Institute of Biochemistry.
3. Mice lacking the photoreceptor-specific ABC transporter ABCA4 ($ABCA4^{-/-}$) were generated as described in (Weng et al., 1999) by the Palczewski lab (UCI, California, USA).

The age of the animals for the experiments was between 5 and 8 weeks.

2.1.4 Software

Table 4: List of the used software with the corresponding supplier.

Software	Source
Amira	Thermo Fisher Scientific
CryoCARE	Buchholz et al., 2019
Fiji	Schindelin et al., 2012
Gctf	Zhang, 2016
IMOD (version 4.10.18)	Kremer et al., 1996
M (version 1.0.9)	Tegunov et al., 2020
MAPS (version 2.1)	Thermo Fisher Scientific
MatLab (version R2015b)	MathWorks
MotionCor2	Zheng et al., 2017
PySeg	Martinez-Sanchez et al., 2020
Pyto	Lučić et al., 2016
Relion (version 3.0)	Zivanov et al., 2018
SerialEM	Mastronarde, 2005
TOM software toolbox	Nickell et al., 2005
TomoSegMemTV	Martinez-Sanchez et al., 2014
UCSF chimera	Pettersen et al., 2004
Warp (version 1.0.9)	Tegunov et al., 2019

2.2 Methods

2.2.1 ROS extraction and cryo-preparation

Five to eight week-old wild type (WT) mice (C57BL/6J, Jackson Laboratory, Bar Harbor, USA), mice heterozygous for the *rd1* mutation (*rd1/+*) and mice lacking the photoreceptor-specific ATP binding cassette transporter ABCA4 (*Abca4*$^{-/-}$) (Weng et al., 1999), were used for the isolation of rod outer segments (ROS). To minimize the interval between dissection and plunge-freezing, only one mouse was used for each preparation. The mouse was euthanized by exposing it to CO_2 for 3-5 min followed by cervical dislocation. The first eyeball was excised with curved scissors and glued (Scotch® Single-use super glue gel) with its sclera side down to a plastic Petri dish. The petri dish was filled with ice cold Ringer's buffer to fully cover the eyeball. The eye was dissected as follows. First, a slit was made with a scalpel blade, and one blade of a fine scissors inserted into the slit. The cornea was cut away and then the lens removed with fine forceps. To separate the retina from the retinal pigment epithelium, Ringer's buffer was applied gently between the layers with a P200 pipet. The retina was transferred into a 0.5 ml tube using a P1000 pipet. To prevent damaging the retina during transfer, the opening of the pipet tip was widened by cutting off its tip. The same procedure was applied to the second eye. After collecting two retinas in one tube, Ringer’s buffer was removed and 25µL of fresh Ringer’s buffer added. The retinas were vortexed at 3200 rpm for 1 min to detach ROS. The sample was centrifuged at 100 rcf for 1 min at 4°C using an Eppendorf 5415R Centrifuge with an F 45-24-11 rotor. The centrifugation step enriched ROS in the supernatant which was transferred into a fresh tube. To collect more ROS, 25 µL Ringer's buffer were added to the retinas, which were then subjected to the same ROS collection procedure. The combined supernatant was gently mixed by repetitive pipetting four times. The resulting sample was used for plunge-freezing. The total extraction time was 10-20 min. This ROS extraction procedure was developed by Dr. Sanae Sakami (Case Western Reserve University, Ohio, USA).

For each glow-discharged copper grid (Quantifoil Cu 200 mesh, holy carbon film R2/1) 4 µl of the supernatant were applied. The grids were plunge-frozen in a liquid ethane/propane mixture (Tivol et al., 2008) at close to liquid nitrogen temperature using a Vitrobot® Mark 4 (Thermo Fisher Scientific, Waltham, Massachusetts, USA). The blotting chamber conditions were set to 37°C, 90% humidity, blot force 10 and 10 s blot time. The grids were blotted with a filter paper and a Teflon sheet from the reverse and front side, respectively. Grids were stored in liquid nitrogen until use.

For the light microscopy, 4 µL of the supernatant were placed on a clear bottom µ-dish (Ø = 35 mm, high, Ibidi GmbH, Gräfelfing, Germany). The images were taken on a CorrSight microscope (Thermo Fisher Scientific) operated at room temperature (light path: wide-field, Objective: Zeiss EC Plan-Neofluar 40/0.9 NA Pol M27air objective (Zeiss, Oberkochen, Germany), working distance = 410 µm, Detector: Digital Camera C10600 ORCA-R2 (Hamamatsu Photonics Deutschland, Herrsching am Ammersee, Germany), image acquisition software: MAPS (version 2.1, Thermo Fisher Scientific).

Plunge-frozen grids were fixed into custom-made autogrids, mounted into a shuttle (Rigort et al., 2010) and then transferred into a dual-beam Focused Ion Beam and Scanning-Electron Microscope (FIB/SEM, Quanta 3D FEG, Thermo Fisher Scientific) using a cryo-transfer system (PP3000T, Quorum

Technologies, Lewes, UK). During FIB operation, samples were kept at a constant liquid nitrogen temperature using an in-house developed open nitrogen-circuit 360° rotatable cryo-stage (Rigort, Bäuerlein, Laugks, et al., 2010). To improve sample conductivity and to reduce curtaining artifacts during FIB-milling, the samples were first sputter-coated with platinum in the Quorum prep-chamber (10 mA, 30 s) and then coated with organo-metallic platinum using an *in situ* gas injection system (GIS, Thermo Fisher Scientific) operated at 26°C, at 12 mm stage working distance and 7 s gas injection time. Lamellae were prepared using a Gallium ion beam at 30 kV. FIB-milling was performed in a stepwise manner using rectangle patterns following similar procedures as in (Schaffer et al., 2017). The initial step was conducted at a stage tilt angle of 25° with a beam current of 1 nA 10-20 µm away from the final lamella area. After rough milling the stage was tilted to 20° and the ion current gradually reduced to lower currents as the thinning progressed (500 pA until 4 µm, 300 pA until 1 µm). For the final cleaning step, a low current of 50 pA was used to obtain lamellae thinner than 250 nm. The progress of FIB-milling was monitored using the scanning electron beam operated at 10 kV and 42 pA. For improved conductivity of the final lamella, the grid was again sputter-coated after cryo-FIB preparation with platinum in the Quorum prep-chamber (10 mA, 1 s) as previously reported in (Mahamid et al., 2016).

2.2.2 Cryo-ET data acquisition

Cryo-transmission electron microscopy (cryo-TEM) observations were performed using a Titan Krios operated at 300 kV (Thermo Fisher Scientific). This microscope is equipped with a field-emission gun, a quantum post-column energy filter (Gatan, Pleasanton, USA), and a Volta phase plate (VPP, Thermo Fisher Scientific) (Danev et al., 2014). The electron optical parameters were set as follows: objective lens focal length f = 3.5 mm; spherical aberration coefficient, C_s = 2.7 mm. Tilt-series were collected using SerialEM software (Mastronarde, 2005) between ± 50° or ± 60° with a tilt increment 2° and a total exposure dose of ~100 $e^-/Å^2$. The exposure dose for the projection at 0° $\text{dose}_{\alpha=0}$ was 1.6 $e^-/Å^2$ fractionated over 5 frames. For higher tilts, the dose was adjusted as a function of the tilt angle α according to the following equation:

$$\text{dose}(\alpha) = \text{dose}_{\alpha = 0} / \cos(\alpha)$$

by acquiring more frames at higher tilt angles. The individual projection images were recorded as movies (dose fractionation mode) on a K2 Summit (Gatan) 3838 x 3710 pixels direct electron detector camera with an image pixel size of 2.62 Å. A fraction of the tomographic tilt-series in this work were acquired with the VPP (Danev et al., 2014). Alignment and operation of the Volta phase plate were carried out as described previously (Fukuda et al., 2015). During automated tilt-series acquisition an autofocusing routine was performed using zero defocus offset with 5 mrad and 10 mrad beam tilt for conventional tilt series and data acquisition with VPP, respectively. For tilt series recorded in focus, the effect of the microscope's spherical aberration on the measured defocus was accounted for by setting the defocus target to 270 nm (Danev et al., 2016). Tomographic tilt-series were collected using standard automated acquisition procedures. All datasets are listed in Table 5.

Prior to the acquisition of the tilt-series, montage images at lower magnification (pixel size of ~2 nm) were taken of the entire lamella. The montage tiles were aligned using the IMOD (version 4.10.18)

(Kremer et al., 1996) command ‘justblend’. Each lamella contained several ROS. In some cases, the ROS ultrastructure was partially distorted. However, the distortions were locally confined and tomographic tilt-series were exclusively acquired on well-preserved ROS.

2.2.3 Tomogram reconstruction

Prior to tilt-series alignment, the projection images were corrected for beam-induced motion with MotionCor2 (Zheng et al., 2017). The CTF parameters for the projections with non-zero defocus were determined with Gctf (K. Zhang, 2016). The CTF-correction was performed prior to tomogram reconstruction with the IMOD function ‘ctfphaseflip’ and dose-filtered as described in (Grant et al., 2015) with a MatLab implementation for tilt-series (Wan et al., 2017). Data acquired with VPP in focus was not CTF-corrected. Tilt-series alignment and tomographic reconstructions were performed using the IMOD software package (version 4.10.18). Platinum particles originating from the protective platinum layer which were deposited over the lamella surface during FIB-milling served as fiducials. Final alignment of the tilt-series images was performed using the linear interpolation option in IMOD. For tomographic reconstruction, the weighted back-projection algorithm in IMOD was used with the radial filter options left at their default values (cut off = 0.35; fall off = 0.05). Micrographs or tomographic slice were visualized in IMOD. In these cases, the density appears dark, i.e. with a low grey value.

2.2.4 Tomogram denoising

Tomograms were denoised using the Cryo-CARE software (Buchholz et al., 2019). The denoising network had a depth of three layers and 32 feature channels in the first layer which were doubled every successive layer. For each tomogram, the network was trained separately. First, two independent, 4x binned tomograms (pixel size = 10.48 Å) were reconstructed: one contained only the information of the odd the other only of even frames. 1200 subvolumes with a size of 64^3 voxels were cropped from the independent tomograms at the same positions. The subvolumes were used to train the network for 200 epochs with 75 steps which was then used to denoise the tomograms.

2.2.5 Tomogram preprocessing in Warp

Tomograms which were acquired with defocus were preprocessed with Warp (Tegunov et al., 2019). Instead of using entire preprocessing capabilities implemented in Warp, the motion corrected, non-CTF-corrected, non-dose-filtered projections of tilt-series were imported into Warp with the corresponding tilt-series alignment files. In a first step, the CTF parameters were calculated for each projection in Warp. The patch size for the CTF estimation was set to 512 x 512 pixels^2, the spatial frequency range used for fit was between 34 Å and 12 Å and the defocus value was searched within ± 2 µm of the tilt-series’ target defocus. For tilt-series acquired with VPP, a phase shift was introduced as additional parameter for the CTF estimation. In a second step, the CTF was estimated for the whole tilt-series taking the tilted geometry of the individual projections into account. For this, the same settings as in the first CTF estimate were used, only the spatial frequency range was expanded to 7 Å.

2.2.6 Measuring of ROS

To measure the repetitive distances of ROS disk membranes, contours of varying length perpendicular to the disk stack were defined in the disk interior (e.g. contour **h** of length h = ||**h**|| in Figure 3 A). The contours were generated in 3dmod by opening the tomographic volume in the Zap window and creating a new model using the ‘Bead Fixer’ tool. Each contour included two points spanning across at least two ROS disks. Cuboids were cropped along these contours (Figure 3 B). The base of the cuboids was a square shaped with an edge length a of 21 voxels (base edges labeled ‘a’ in Figure 3 B). The cuboid voxels were averaged along the base area to obtain a 1D intensity profile of length h (Figure 3 C). The distances were measured from the points where the membrane signals reached 50% of the maximum intensity (marked as red circles in Figure 3 C).

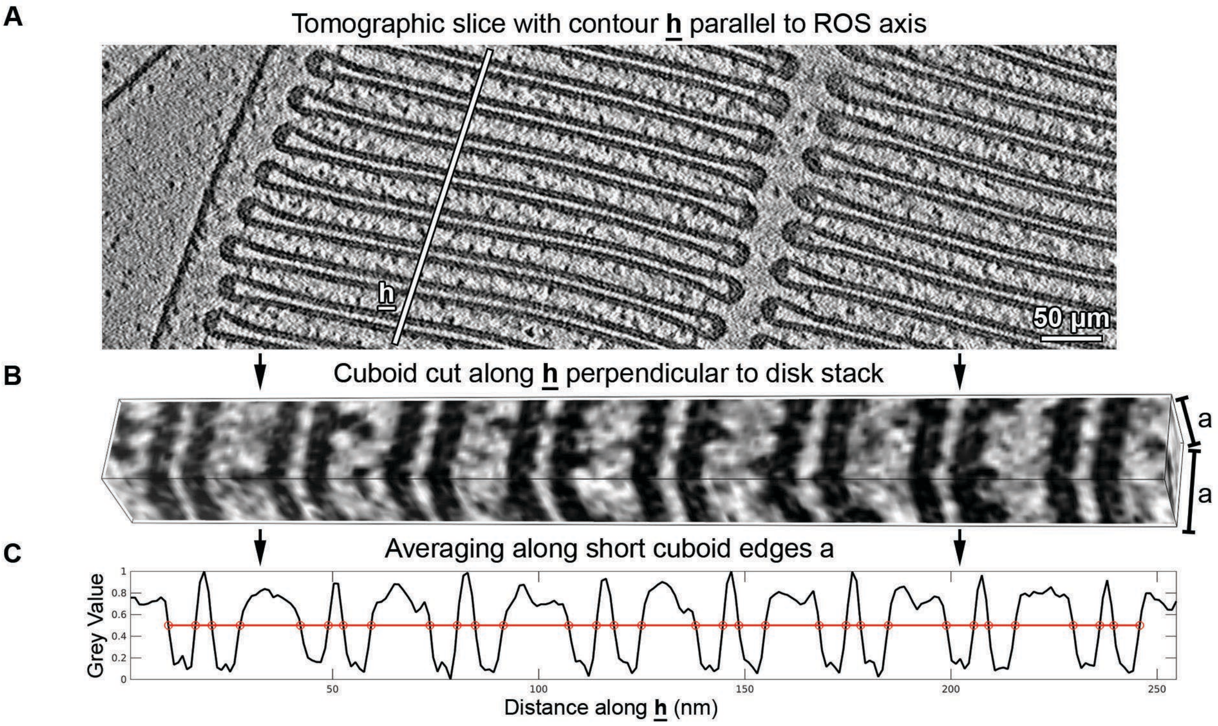

Figure 3: Measurement of the repetitive distances between ROS disk membranes.
A) Contours **h** perpendicular to the disk stack were defined in 4x binned tomograms. **B)** Cuboids were cropped along **h** with length h and square base area with edge length a = 21 voxels. **C)** Cuboids were averaged along the base edges to generate 1D density profiles of length h. Points, where the membrane signal dropped to 50% of the maximum intensity are marked by red circles. They were used to calculate distance between membranes and membrane thicknesses.

For the thickness calculation of the plasma membrane (PM) d_{PM}, a total of 430 subvolumes were extracted from 5 tomograms along the PM, aligned and subvolume averages were calculated for each tomogram. The PM thickness was determined in the 1D intensity profiles along **H** perpendicular to the PM where the signal was 50% of the maximum intensity (Figure 4 A). A similar approach was used to compute the maximum diameter of the disk rim d_{DR} parallel to the ROS cylinder axis. A total of 3000 subvolumes from 6 tomograms were aligned to a common reference and subvolume averages calculated for each tomogram. The 1D intensity profile along **K** was used to determine d_{DR} (Figure 4 B). To calculate the width of the cytosolic gap at the disk incisure d_{IN} and the distance between the PM and the disk rim d_{PR}, the refined coordinates of the disk rim subvolumes were utilized. d_{Shift} was determined as the distance from the center of the subvolume average to the outer periphery of the disk rim along **<u>L</u>** (Figure 4 B). The subvolumes were separated into three groups: group 1 and group 2 comprised subvolumes on opposite sides of the disk incisure. Group 3 contained subvolumes close to the PM. The gap at the incisure d_{IN} was computed as follows:

$$d_{IN} = d_1 - 2\, d_{Shift}$$

with d_1 as the shortest distance of a coordinate in group 1 to a plane defined by its nearest neighbors in group 2 and *vice versa* (Figure 4 C). For the distance between PM and the disk rim d_{PR}, the central plane of the PM was segmented with TomoSegMemTV (Martinez-Sanchez et al., 2014). Then, d_{PR} was calculated according to:

$$d_{PR} = d_2 - d_{Shift} - d_{PM}/2$$

with d_2 as the shortest distance between a coordinate in group 3 and the central plane of the PM as determined by the segmentation (Figure 4 D). Besides subvolume averaging, the distance calculations and the required image processing steps were performed in MatLab aided by the TOM software toolbox (Nickell et al., 2005).

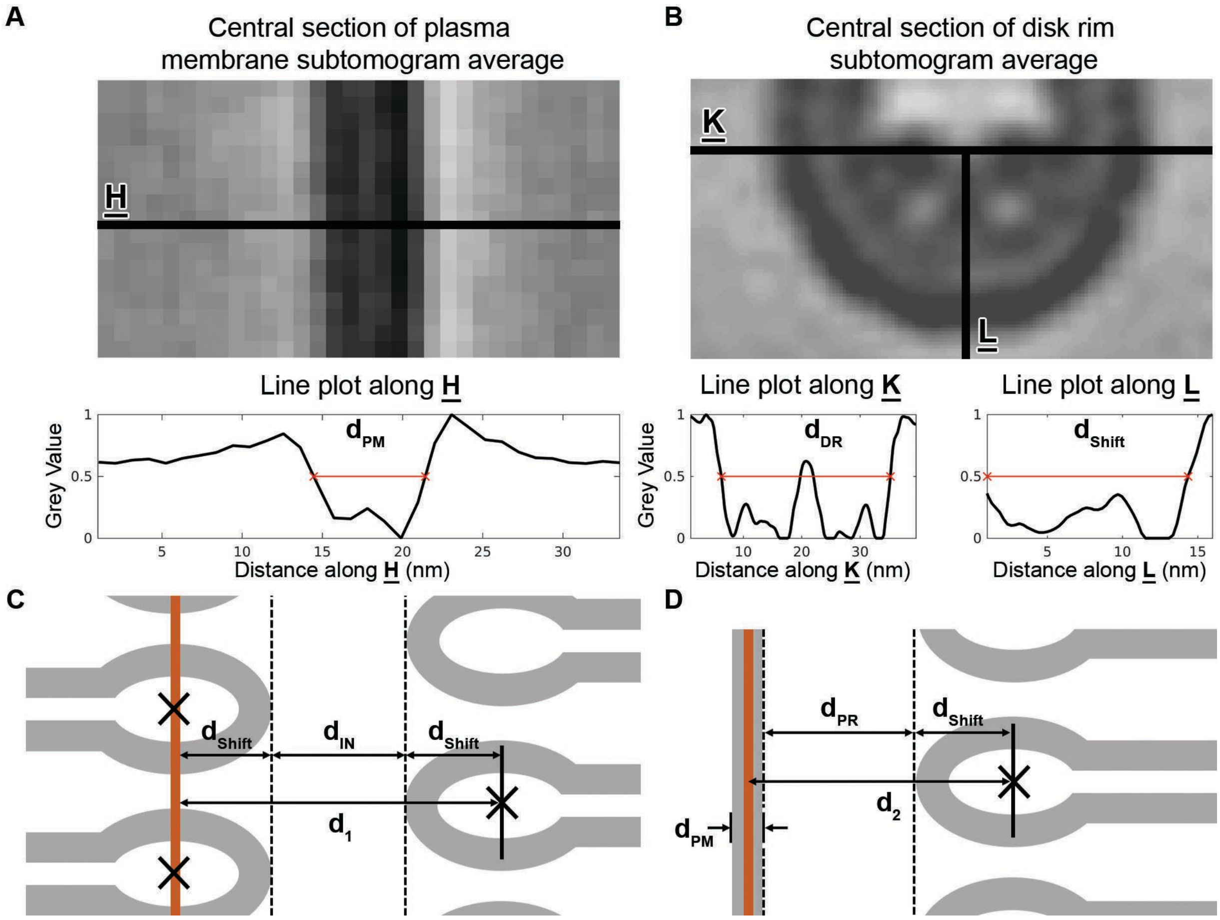

Figure 4: Measurements related to the plasma membrane and the disk rim.
A) and **B)** thickness of the plasma membrane and measurement of the disk rim, respectively. The upper panels depict subvolume averages and defines the directions **<u>H</u>**, **<u>K</u>** and **<u>L</u>**. The lower panels show density profiles along these directions. Characteristic distances are indicated as red lines. **C)** Measurement of the cytosolic gap at the disk incisure d_{IN}. **D)** Measurement of the cytosolic gap between the disk rim and the plasma membrane d_{PR}. The brown line represents the central plane of the PM as estimated by segmentation.

2.2.7 Connector segmentation

All segmentations were performed on 4x binned tomograms, corresponding to a pixel size of 10.48 Å. More dense structures, like proteins, appear darker in tomographic slices which translates into a lower grey value. First, all ROS membranes were automatically segmented by tensor voting (Martinez-Sanchez et al., 2014). The results of the automated segmentation and the original tomograms were loaded in Amira (v.6.2.0, Thermo Fisher Scientific). By comparing the two volumes, segmented patches which did not correspond to membranes were identified and manually removed. Afterwards, the membranes were sorted into disk membranes (DM) and plasma membrane (PM). This type of segmentation was performed with all tomograms irrespective of the data collection method. However, without further processing, the segmentation of connectors was only possible in VPP tomograms, while conventional tomograms had to be denoised with Cryo-CARE. Most processing steps were executed with custom-developed scripts in MatLab. The tensor voting script was adapted from (Martinez-Sanchez et al., 2014). Only the Pyto software package and Cryo-CARE were executed in a python shell. The software was derived from (Lučić et al., 2016) and (Buchholz et al., 2019), respectively.

2.2.7.1 Segmentation of connectors between disks

For the connector segmentation, the membranes of adjacent disks were grouped into pairs. The results of the initial automated membrane segmentation correspond to the central membrane plane. By adding a layer of three voxels on either side to central plane, the segmentation was grown to a thickness of 7 nm. This was then used to mask the membranes which had an apparent thickness of ~6.8 nm in raw tomograms. Additionally, these masks defined the borders of the cytosolic gap which a connector must bridge. The cytosolic voxels between the membrane masks were normalized separately for each membrane pair to a mean value of zero and a standard deviation of one. This extinguished gradients in the grey value distribution throughout a tomogram caused by heterogeneous lamella thickness and compensated for contrast differences between tomograms. To pick the connectors, the Pyto software was used (Lučić et al., 2016). The original workflow segments connectors between the membranes of adjacent disks by evaluating all cytosolic voxels between the membrane masks as described below. The algorithm runs a grey value ramp from a user defined lowest grey value g_{min} to a highest grey value g_{max}, with a step size g_{step} according to:

$$g_i = g_{min} + (i - 1)g_{step} \cap i = 1, 2, 3, \dots , g_{max}/g_{step}$$

At each iteration i, the algorithm performs a connectivity segmentation by selecting j groups of voxels v_i^j based on four conditions:

1. all voxels in the group v_i^j have a grey value smaller or equal to g_i,
2. the voxels of v_i^j are in direct contact (face-to-face),
3. v_i^j links the membrane masks of two adjacent disks,
4. no voxels of the group v_i^j is in direct contact with any other voxel of a group v_i^k with $k \neq j$.

During the next iteration with the grey value threshold at g_{i+1}, groups of voxels v_{i+1}^j are selected that inevitably contain the v_i^j with additional voxels of grey value $g_i \leq g(v_{i+1}^j - v_i^j) < g_{i+1}$ in direct contact with v_i^j. This defines a relation between all connectors picked at the individual grey value steps. Connectors with $v_i^j \neq v_i^k$ are independent while connectors with $v_i^j \in v_{i+1}^j$ are related by an ancestor-descendant relation. The connector segmentation as output contains only independent groups of voxels which do not have ancestors. The original Pyto workflow is sketched in Figure 5 A.

For the customized Pyto workflow, an additional mask was applied to the tomographic volume. First, a binary mask was created that is one for all voxels with grey value below g_{max} and elsewhere zero. Second, this binary mask was subjected to watershed transform (Fernand Meyer Algorithm (Meyer, 1994) implemented in MatLab) with catchment basins filled from the center between the two membranes. Third, a volume with the watershed lines set to zero and elsewhere one was multiplied with the binary mask. The resulting mask was applied to the original tomographic volume. Then the Pyto software was used to segment connectors in the masked tomogram. A sketch of the customized Pyto workflow and its steps applied to one real data membrane pair are depicted in Figure 5 B and C, respectively.

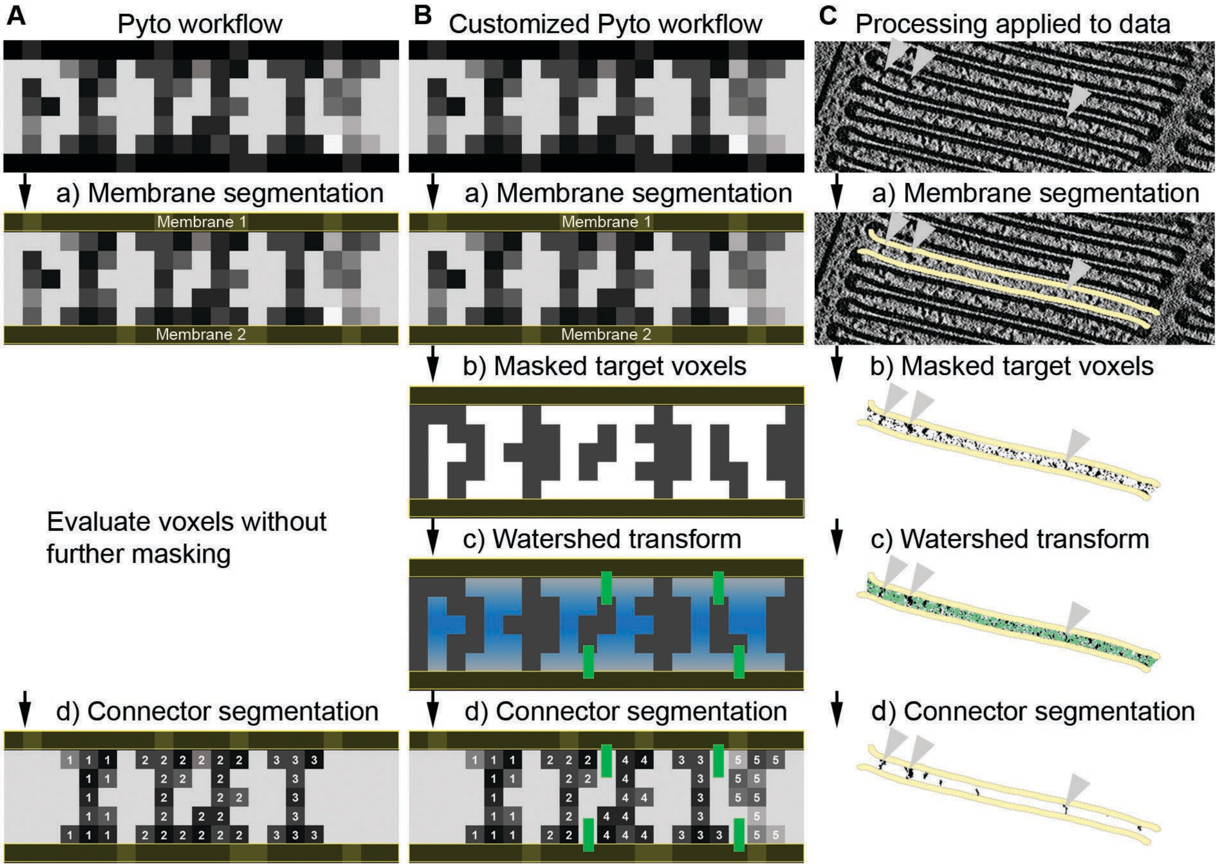

Figure 5: Sketch of the automated segmentation methods.
A) The original Pyto workflow. **B)** The customized Pyto workflow. It involves the creation of a binary mask with a single threshold. The binary mask is then subjected to watershed transform with catchment basins filled from the center between the membranes towards outside as indicated by the gradient of blue color in step c). Watershed lines are shown as green bars. **C)** The customized Pyto workflow applied to actual data on the example of one membrane pair. Membrane masks are depicted yellow, watershed lines in green and segmented connectors in black. Connectors that can be tracked throughout the processing pipeline are marked by grey arrow heads.

The threshold ramp for Pyto was always started at the minimum grey value of -2 and ended at maximum grey value of -0.68 and -0.48 for VPP and conventional, denoised tomograms, respectively. The step size was in all cases 0.02.

The manual segmentation of connectors was performed as follows: initially, the membranes in the tomograms were masked as done for the automated segmentation. Tomographic volumes with the membrane mask applied were loaded into Amira (v.6.2.0, Thermo Fisher Scientific) and evaluated slice by slice. Groups of voxels that by visual inspection connect the membrane masks of adjacent disks were selected with the 'Magic Wand' tool (Amira v.6.2.0).

2.2.7.2 Statistical analysis of connectors between disks

The segmented connectors and the membrane surface area were divided into two fractions. The disk rim fraction was within 40 nm from the outer periphery of disks rims. The reminder was considered the disk interior fraction. The local connector concentrations in the membrane fractions were calculated as the number of connectors $n_{fraction}$ per surface area $A_{fraction}$:

$$\rho_{fraction} = n_{fraction}/A_{fraction} \cap \text{fraction} = \text{rim, interior}$$

To compare the determined local concentrations with literature values for ROS proteins, the connector concentrations per full disk membrane were calculated. The total disk membrane area A^{tot} was estimated based on the morphological considerations specified in Figure 6 A (Makino et al., 2012; Nickell et al., 2007) according to:

$$A^{tot} = \pi r_{out}^2 - r_{in} d_{cleft} = 1.3 \mu m^2$$

The total area of the fractions per disk $A_{fraction}^{tot}$ were evaluated based on the distance threshold of 40 nm from the rim and the assumptions in Figure 6 A:

$$A_{rim}^{tot} \approx \pi(r_{out}^2 - r_{in}^2) + 2d_{rim} r_{in} = 0.2\ \mu m^2 \qquad A_{interior}^{tot} = \pi r_{in}^2 - r_{in}(d_{cleft} + 2d_{rim}) = 1.1\ \mu m^2$$

The ratio $f_{fraction}$ of the total membrane area per fraction to the total disk area was calculated as:

$$f_{fraction} = A_{fraction}^{tot}/A^{tot} \cap \text{fraction} = \text{rim, interior}$$

$$f_{rim} = 0.2 \qquad f_{interior} = 0.8$$

The connector concentration per disk is defined as:

$$\rho_{fraction}^{tot} = \rho_{fraction} f_{fraction}/2$$

The division by 2 was introduced because a connector links two membranes. Therefore, the segmentation approach detects each connector effectively twice, in contrast to a density attached to only one membrane.

To do the spatial analysis, each connector was assigned with a central coordinate C_{con} located in the center between the two neighboring membranes (Figure 6 B). A coordinate based on the center of mass of all connector voxels would result in off-center positions (Figure 6 B) which would induce errors in the spatial analysis. Nearest-neighbor distances between connectors were calculated based on C_{con}. To estimate the connector length L_{con}, the two membrane contact points P_{mb1} and P_{mb2} of a connector with both disk membranes were determined (Figure 6 B). L_{con} was calculated as the sum of the distances between the central coordinate and the two contact points according to:

$$L_{con} = ||\underline{C_{con}P_{mb1}}|| + ||\underline{C_{Con}P_{mb2}}||$$

with $||\underline{C_{con}P_{mb1}}||$ and $||\underline{C_{Con}P_{mb2}}||$ denoting the distance between C_{con} and the contact point P_{mb1} and P_{mb2}, respectively (Figure 6 B). The mean grey value was defined as the average grey value of all connector voxels. The statistical significance of differences between disk rim and disk interior connectors was established with the two-sample Kolmogorow-Smirnow test in MatLab.

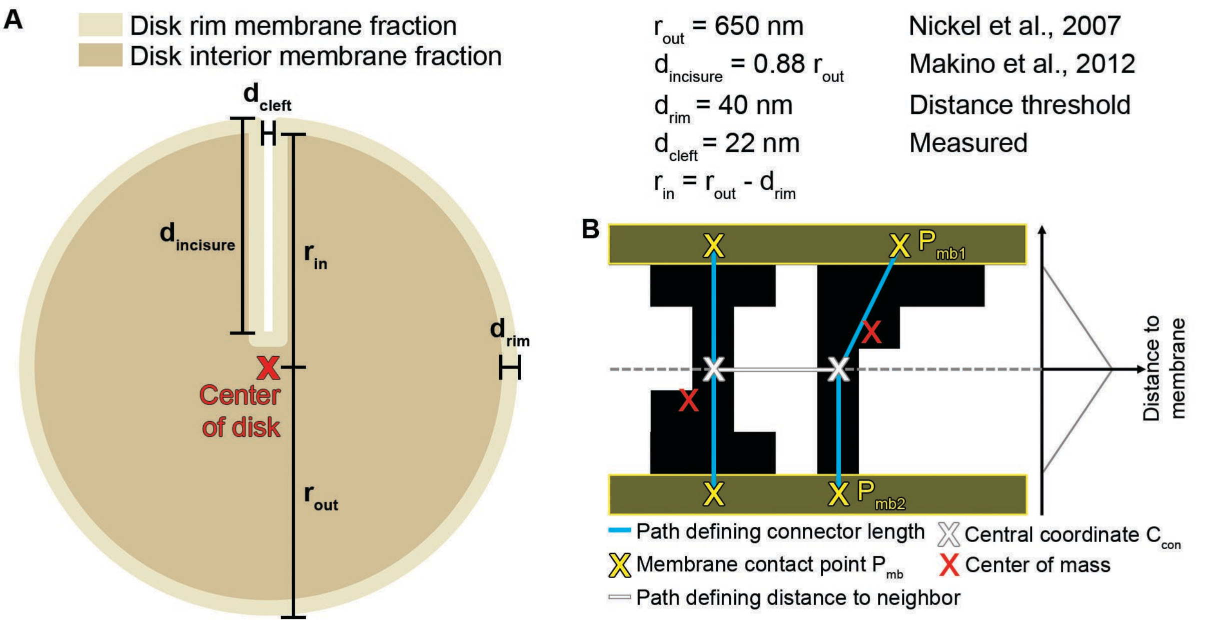

Figure 6: Considerations for the statistical analysis of connector segmentation.
A) Disk morphological considerations to calculate the rim, interior and total membrane area. **B)** Sketch of two connectors illustrating the characteristic connector points. For each connector, the membrane contact points P_{mb} and the central point C_{con} were used to calculate the connector length. C_{con} of neighboring connectors was used to compute the nearest-neighbor distances.

2.2.7.3 Segmentation of connectors between plasma membrane and disk rim

All ROS membranes were initially segmented by tensor voting (Martinez-Sanchez et al., 2014) and the results manually refined in Amira. The plasma membrane (PM) and disk membranes within 30 nm of the outer disk periphery were selected and grown to a thickness of 7 nm and 9 nm, respectively. These membrane masks defined the boundaries for connectors between PM and disk rims (Figure 7 B). The customized Pyto workflow was used to pick connectors. Catchment basins for the watershed transform were filled from the middle between PM and disk rims (Figure 7 C). The threshold ramp started at g_{min} = -2 and ended at g_{max} = 0 with a step size g_{step} = 0.02 (Figure 7 D).

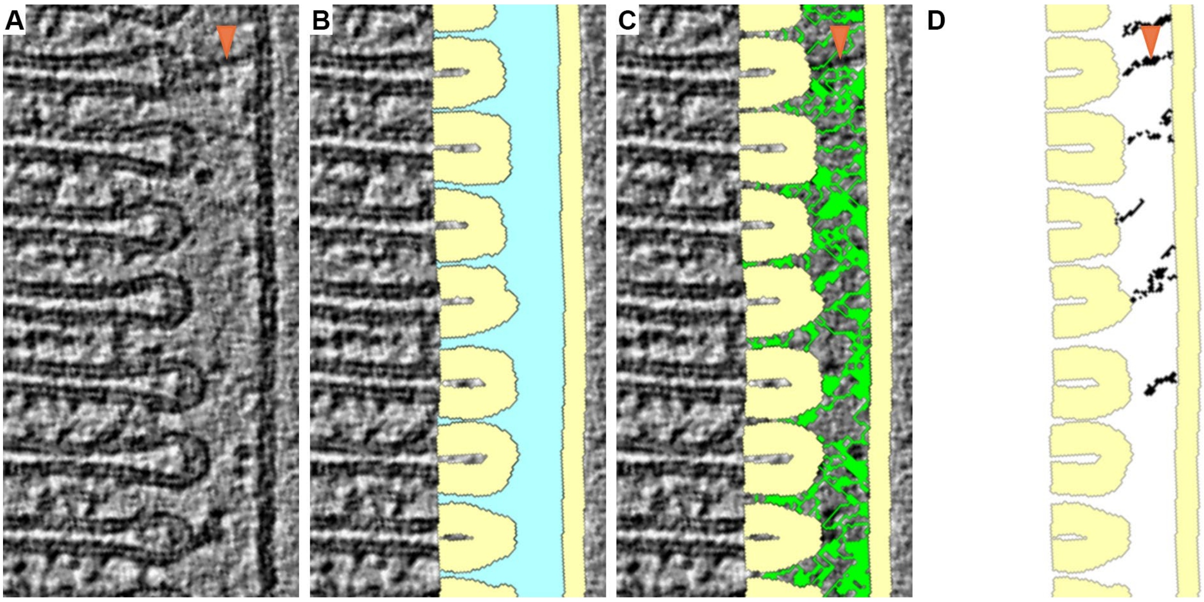

Figure 7: Segmentation of connectors between plasma membrane and disk rim.
A) Tomographic slice of A ROS tomogram. **B)** The membrane masks are shown in yellow, the area searched for connectors in cyan. **C)** The watershed transform as additional masking step in the customized Pyto workflow. The watershed lines are depicted in green. **D)** Final output of the customized Pyto segmentation. Segmented connector are black. One density that appears as a connector throughout the processing steps is marked by an orange arrowhead.

2.2.8 Subvolume averaging workflows

The initial subvolumes were extracted from dose-weighted and, if possible, CTF-corrected tomograms. Their initial alignment was performed with the in-house developed software based on scripts derived from TOM, AV3 and Dynamo (Schur et al., 2016). Classification of 3D subvolumes and the final alignments were performed in Relion (version 3). For tilt-series acquired with defocus, the subvolumes were extracted with Warp. Warp automatically generates a CTF model for each subvolume which is needed for Relion (Tegunov et al., 2019). For the in-focus VPP tomograms a simple ‘fan’-shaped CTF model (Bharat et al., 2015) was created which was one for all information-containing slices in Fourier space and zero elsewhere. To describe the orientation of subvolumes within the tomograms, triplets of Euler angles in ‘ZXZ’ convention are used in this thesis. This comprises the angles phi, theta, and psi. Phi is the angle of the first rotation around the z-axis which is also referred to as in-plane rotation. Theta describes the second rotation around the new y-axis and psi the third rotation around the new z-axis. For the grey value representation of subvolume averages, the scale was inverted compared to tomographic slices. Therefore, density in slices through subvolume averages appears bright, translating into a high grey value. Slices of subvolume averages were depicted in IMOD. Isosurface representations and subvolume positions within the context of a tomogram in UCSF chimera (Pettersen et al., 2004).

2.2.8.1 Subvolume averaging of connectors between disks

The initial subvolumes extraction points of connectors between disks were defined at their two membrane contact points P_{mb1} and P_{mb2} (Figure 6 B) as elucidated by the segmentation (2.2.7.1). Initial Euler angles for psi and theta were determined so that the subvolume z-axis was parallel to the local normal vector of the disk membrane. The phi angles were randomized. First, subvolumes were extracted from 4x binned tomograms (pixel size = 10.48 Å, box size = 64^3) and aligned with shifts only allowed perpendicular to the membrane plane. For the disk interior connectors, the angle of the in-plane rotation was not searched. For the disk rim connectors, a search for the phi angle was conducted which covered the whole 360° to allow alignment of the disk rims with respect to each other. The initial alignment brought the membranes into register and refined the initial orientations. The heterogeneity of the subvolumes impaired alignment and classification of 3D subvolumes in Relion. Therefore, for each subvolume rotational averages around the z-axis were calculated and the resulting 2D images classified. For this, the 'plane_align_class.py' script was used as part of the PySeg package (Martinez-Sanchez et al., 2020). A cylindrical mask focused the classification on the cytosol between disks. Subvolumes of classes indicating a density between the membranes were considered most promising. They were extracted from 2x binned tomograms (pixel size = 5.24 Å, box size = 64^3) and aligned in Relion. Custom-made alignment masks usually caused artifacts in the averages. Hence, simple sphere masks with 200 Å diameter were used for the alignment.

2.2.8.2 Averaging of connectors between plasma membrane and disk rim

To pick densities between the plasma membrane (PM) and disk rims, two different strategies were employed. The first method exploited the results of the connector segmentation (2.2.7.3). The contact points of the connectors with the PM were used as subvolume extraction points. From each of these coordinates a vector was calculated, pointing in the direction of the shortest distance to the disk rim. The initial Euler angles for theta and psi were defined so that the subvolume z-axis coincided with this vector. The angle phi of the in-plane rotation was randomized. Subvolumes were extracted in 4x binned tomograms (pixel size = 10.48 Å, box size = 64^3) and aligned to a common reference. This method was only used for the WT dataset acquired with VPP and defocus ($WT_{VPP\text{-}def}$).

Aim of the second method was to find densities attached to the disk rim. Splines were manually picked along disk rims and extraction points defined every 0.5 nm along the splines. Subvolumes were extracted from 4x binned tomograms (pixel size = 10.48 Å, box size = 64^3) and aligned. The resulting average displayed the expected hairpin-like shape of the disk rim. Subvolumes were shifted to center the outer periphery of the disk rim in the center of the subvolume box and reoriented so that the subvolume z-axis pointed away from the PM. This method was applied to the $WT_{VPP\text{-}def}$ and the conventional dataset WT_{conv}. To classify the densities picked by both methods, rotational averages were calculated around the subvolume z-axis and the 2D images classified (Martinez-Sanchez et al., 2020). The cylindrical mask for classification focused on the cytosol between PM and disk rim. Subvolumes of class averages indicating membrane-attached densities were extracted from 2x binned tomograms (pixel size = 5.24 Å, box size = 64^3) with Warp and aligned in Relion.

2.2.8.3 Averaging of disk membrane densities

First, the central plane of ROS membranes were segmented by tensor voting (Martinez-Sanchez et al., 2014) (Figure 8 A). The highly curved membranes at the disk periphery were discarded. Based on the segmentation, membrane masks were created with a thickness of 7 nm and separated into odd and even numbered membranes (Figure 8 B). Densities were only picked within these membrane masks with an implementation of discrete Morse theory as part of the PySeg software package (Martinez-Sanchez et al., 2020). The resulting coordinates were projected back onto the central membrane plane (Figure 8 C) and distance-cleaned. This assured of minimum distance of 3 nm between picked densities in the central plane of the membrane (Figure 8 D). Afterwards, for each coordinate picked within an odd numbered membrane a vector was calculated which pointed in the direction of the shortest distance to an even numbered membrane and *vice versa*. Subvolumes were extracted at the coordinates from 4x binned tomograms (pixel size = 10.48 Å, box size = 32^3) and the z-axis oriented in the direction of the vector (Figure 8 D). Thus, initial values for two Euler angles were obtained and the cytosolic and luminal side in subvolumes of odd and even membranes oriented in the same direction. The phi angles were randomized. Then subvolumes were aligned to bring the membranes into register. 2D rotational averages around the subvolume z-axis were classified with a mask focusing on the cytosol. Subvolumes of the most promising classes with densities attached to the disk membrane were extracted from 2x binned tomograms (pixel size = 5.24 Å, box size = 64^3) and aligned in Relion.

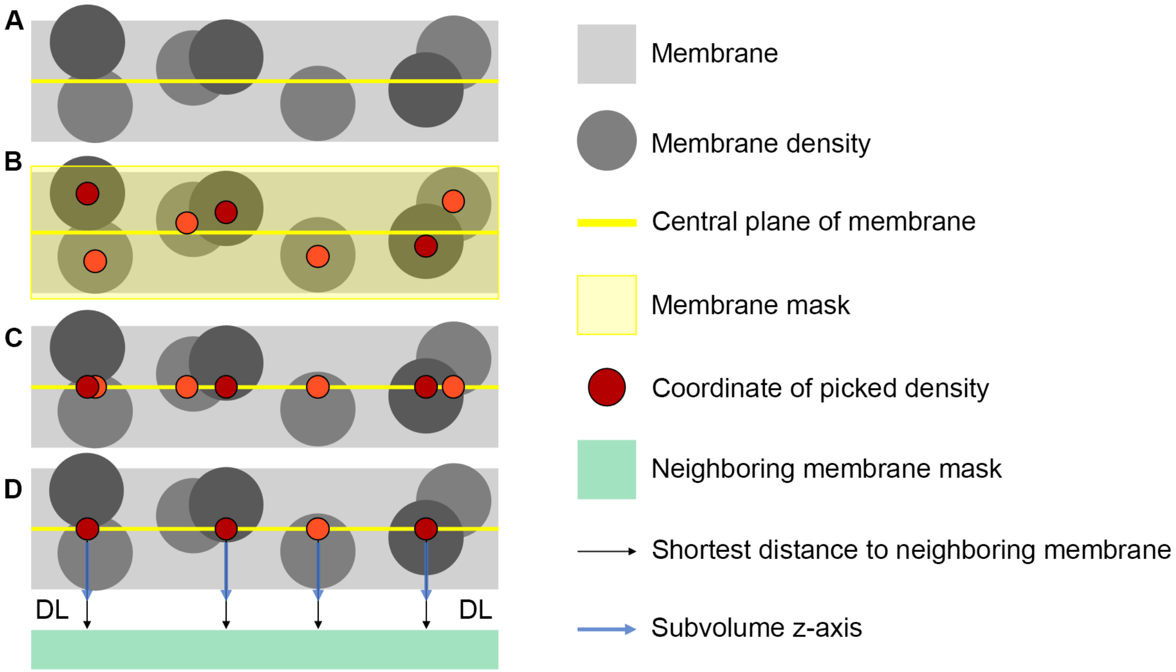

Figure 8: Sketch of membrane density picking.
A) The initial membrane segmentation determined the central plane of the membrane (yellow line). **B)** Membrane masks were created by growing the central plane to a thickness of 7 nm (yellow box). Densities were picked within the membrane masks as described in (Martinez-Sanchez et al., 2020). **C)** Coordinates were projected onto the central membrane plane. **D)** Distance-cleaning assured a minimum distance of 3 nm between neighboring densities. The z-axis of subvolumes was oriented in the direction of the shortest distance to the nearest neighboring disk membrane. DL denotes the disk lumen.

2.2.8.4 Subvolume averaging of disk rims

Splines were manually picked along disk rims. For that, the tomographic volume was visualized in the 3dmod ZAP window, and a new model created using the ‘Bead Fixer’ tool. A new contour was defined for each disk rim by adding points along its outer periphery (Figure 9 A). Initial subvolume extraction points were set along the splines with 1 nm distance. Initial Euler angles for psi and theta were assigned so that the local spline direction dictates the orientation of the subvolume z-axis. The phi angles of the in-plane rotation were randomized (Figure 9 B). Initially, 4x binned subvolumes (pixel size = 10.48 Å, box size = 64^3) were extracted. The initial average was composed of a strong density along the z-axis. During the initial alignments, the translations along the spline were restricted to 1 nm and the entire phi range was sampled, while the search range for psi and theta was restricted to ± 15°. Later, this search was refined. For the initial reference, a subset of 300 subvolumes was aligned against the unstructured, first average. After several iterations, the symmetry was broken until the average converged into a shape that resembled the hairpin-like structure of the disk rim. During this step, the subvolume positions converged to the disk rims and a first estimate for all three Euler angles was obtained (Figure 9 C). Two-times binned subvolumes were extracted (pixel size = 5.24 Å, box size = 64^3) at the refined coordinates and aligned to their average low-pass filter to 30 Å.

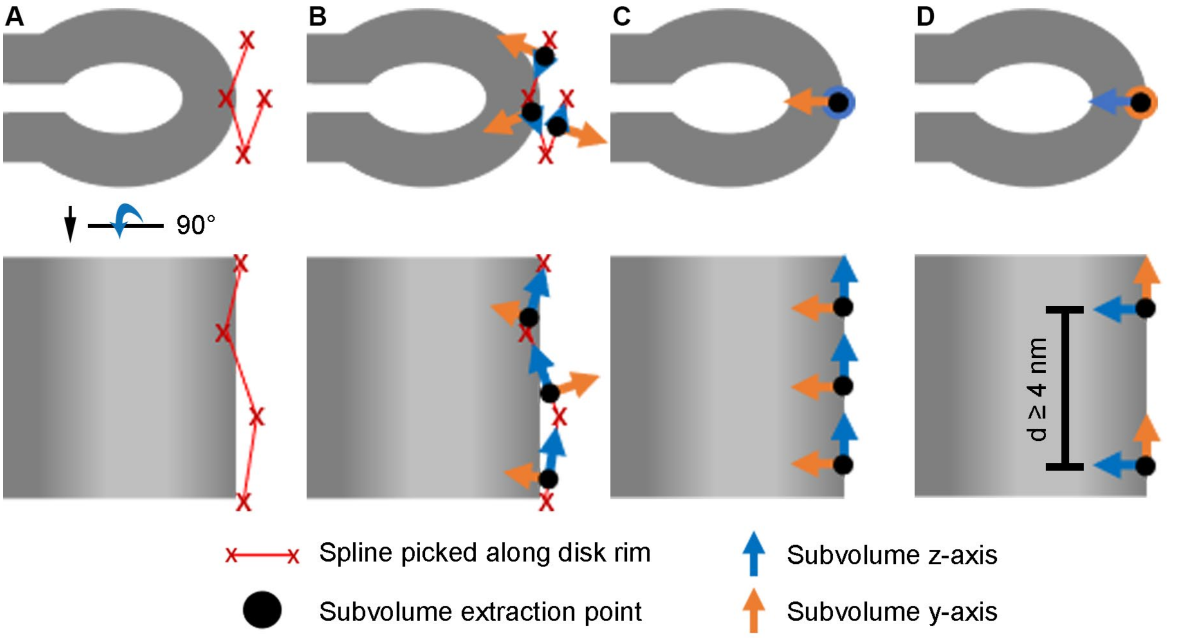

Figure 9: Sketch of initial picking and alignment of disk rim subvolumes.
A) Manually picked splines along the disk rim are marked in red. **B)** Initial extraction points and subvolume orientation. The subvolume z-axis (blue arrow) is oriented along the local direction of the spline. The in-plane rotation was randomized. **C)** During the initial alignment subvolume positions converged to the disk rim and the orientations were refined. **D)** Afterwards Subvolumes were distance-cleaned and reoriented. The z-axis is now pointing parallel to the disk membranes into the disk lumen.

The subvolume average revealed a periodic scaffold with a repeat of ~4 nm and subvolume positions partially converging into the same points along the disk rim (lattice points) which had an average distance of ~4 nm. This information was used to perform so-called distance-cleaning. At each of the lattice points, the particle with the highest similarity to the subvolume average, estimated by the cross-correlation score, was kept and all others discarded, which resulted in a minimal distance of 4 nm between subvolume coordinates. To potentially take the symmetry of the repeats into account, the subvolumes were reoriented by rotating the subvolume z-axis to point into the disk lumen parallel to the disk membranes and the y-axis parallel to the ROS cylinder axis (Figure 9 D). By now, the subvolume average revealed a central and two peripheral rows of density at the disk rim.

Unbinned subvolumes (pixel size = 2.62 Å, box size = 128^3) were extracted and processed in Relion. As the previous alignment steps determined the orientations of the subvolumes with reasonable precision, the Euler angles in the Relion input star-file were set with a 'Prior' which allows to restrict the angular search around these angles. The alignment was focused on the central row of density with a wedge-shaped mask that covered 4 repeats (Figure 10 A). After a first round of alignment, the subvolumes were classified without particle alignment, allowing 10 to 15 classes and 'regularization parameter T' set to 0.1. Classes which indicated a highly ordered, symmetric disk rim scaffold were selected, distance-cleaned and separately aligned in Relion. The averages obtained by processing two independent half-sets of the data were used to calculate Fourier shell correlation (FSC) curve (Bharat et al., 2016). The global resolution was estimated as the spatial frequency where the FSC drops to 0.5 which is a more conservative threshold than 0.143 according to the 'gold-standard'. The final density maps were sharpened with a *B*-factor of -400 Å^2. Subvolume averaging of disk rims was performed on 4 different data sets: disk rims of WT ROS in (1) conventional tomograms without VPP ($\mathrm{WT}_{\mathrm{conv}}$), (2) with VPP in focus ($\mathrm{WT}_{\mathrm{VPP\text{-}inf}}$), with VPP and defocus ($\mathrm{WT}_{\mathrm{VPP\text{-}def}}$) and (4) of ROS in *Abca4*$^{-/-}$ mice with VPP in focus (*Abca4*$^{-/-}_{\mathrm{VPP\text{-}inf}}$).

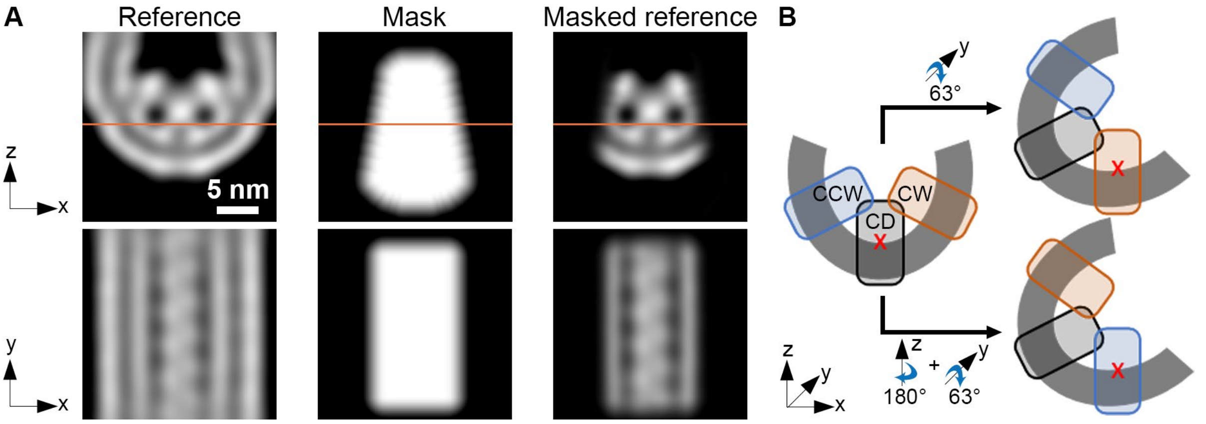

Figure 10: Alignment of central and peripheral density rows at disk rims in Relion.
A) Reference and mask for the alignment of unbinned subvolumes. The initial reference, the mask and the masked reference are shown in the left, middle and right panel, respectively. The orange line in the upper panel indicates the position of the slice in the lower panel. **B)** Sketch to illustrate the symmetry operations used to align the clockwise- (CW) and counterclockwise (CCW) row of density with respect to each other. Starting points were the orientations of the central density (CD) row. The subvolume extraction points are marked by red crosses.

For $\mathrm{WT}_{\mathrm{conv}}$ further processing steps were applied. The output of the alignment with the classified subvolumes was imported into the *M* software (version 1.0.9, (Tegunov et al., 2020)). *M* perfomed a refinement of the tilt-series alignment using subvolumes as fiducials. The default refinement parameters were used with an image and volume warp grid of 3x3 and 2x2x2x10, respectively. Furthermore, particle positions and stage angles were refined but not the CTF estimate. Afterwards, all subvolumes before classification were re-extracted from tomograms with refined tilt-series alignment and processed by the same Relion pipeline as used before running *M*.

Furthermore, the peripheral rows of the $\mathrm{WT}_{\mathrm{conv}}$ dataset were analyzed. To generate the initial extraction points, the unbinned coordinates of the central row were modified. First, the peripheral rows were centered and rotated to assume a similar orientation as the central row before. Additionally, clockwise

(CW) and counterclockwise (CCW) row were aligned to each other. For CW row, the orientation of CD was rotated by 63° around the y-axis. The CCW required a 180° rotation of the CD orientations around the z-axis followed by 63° around the y-axis. Subvolumes were extracted with Warp from unbinned tomograms and subjected to the same subvolume averaging pipeline as the central density. This included a first round of classification and alignment in Relion, tilt-series refinement in *M*, re-extraction of subvolumes from tomograms with refined tilt-series and a second round of classification and alignments. All alignment steps were performed for CW and CCW separate and both peripheral rows combined.

2.2.9 Cryo-serial milling and block face imaging

Volume imaging of ROS as prepared for cryo-ET by serial milling and block face imaging was performed at Carl Zeiss SMT (Oberkochen, Germany) with the help of Dr. Andreas Schertel. The samples were coated with a layer of conductive metallic platinum and protective organo-metallic platinum. The samples were FIB-milled and imaged in a Zeiss Crossbeam 540 FIB/SEM. Initial rough milling was performed with the Gallium FIB at 30 kV and an ion current of 1 nA to cut a hole into an EM grid squares. To polish the block face and for subsequent data acquisition, the ion current was reduced to 100 pA. The ion beam repeatedly removed ~15 nm of the biological material perpendicular to the grid. The newly cleared block face was imaged using the SEM at 8 kV acceleration voltage and secondary electrons were detected with an in-lens detector (Schertel et al., 2013). The pixel size of the recorded SEM images was 3 nm with an exposure-dose of 0.9 $e^-/Å^2$. Images of the series were aligned according to (Guizar-Sicairos et al., 2008) and rescaled (pixel size = 6 nm) in MatLab.

2.2.10 Lysis of retinas for Western blotting and mass spectrometry

Retinas of WT and *rd1/+* mice were collected in 1.5 mL tubes with one retina per tube and stored in 100 µL Ringer’s buffer at -80°C until usage. The retinas were thawed on ice and the Ringer’s buffer removed before the lysis protocol was started. Three different lysis methods were used:

1. The first method used RIPA buffer for the lysis. 200 µL RIPA buffer were added to the retina and incubated for 2h in a Thermomixer comfort (Eppendorf AG, Hamburg, Germany) at 800rpm and a temperature below 10°C. The lysate was centrifuged at 14000 rcf for 15 min at 4°C. The supernatant was collected into a fresh tube.
2. The second method used the same procedure as method 1 but the mass spectrometry compatible buffer I for the lysis.
3. Method 3 lysed the retinas in 200 µL mass spectrometry compatible buffer II. After incubation for 10 minutes at 95°C, the samples were ultrasonicated with a Sonopuls homogenizer (BANDELIN electronic GmbH & Co. KG, Berlin, Germany) for 2 min with 0.5 s pulse at 50% intensity and 0.2 s pause. Incubation and ultrasonication was repeated for a second time, followed by a final incubation for 2 min at 95°C. The lysis was done by the Biochemistry Core Facility at the Max Planck Institute of Biochemistry.

The protein concentration of the lysates was estimated with the Coomassie Protein-Assay according to the manufacturer instructions. The lysates were stored at -80°C until usage.

2.2.11 Western blotting

First, the proteins contained in the retina lysates were separated by SDS-PAGE. On each gel (NuPAGE™ 4-12 % Bis-Tris, 1.0 mm, 10-Well) six different samples derived from six different mice were loaded. Three of them were obtained from WT and three from *rd1/+* mice. For each lysate, a total protein amount of 10 ng was taken, mixed with loading buffer, cooked at 95°C for 5 min and loaded into a well of the gel. The gels were run for 45 min at 200 V in 1x MOPS running buffer. Proteins were transferred from the SDS-Page gels onto polyvinylidenfluorid (PVDF) membrane by electroblotting. Prior to the assembly of the filter paper sandwich, the gels were washed for 10 min in transfer buffer and filter papers soaked in transfer buffer. The PVDF membrane was activated for 1 min in Methanol and washed with transfer buffer. The sandwich was composed of the gel on the PVDF membrane with a thin and a thick filter paper on either side. The sandwich was placed between the metal plates of a Bio-Rad semi-dry transfer system (Bio-Rad Laboratories, Hercules, USA). Transfer was performed with a maximum voltage of 15 V at constant current of 50mA for 90 min. Afterwards, the PVDF membrane was dried 1 h at room temperature, activated for 1 min in methanol, washed with TBS-T and blocked 1 h at room temperature with blocking buffer. Then the membranes were incubated with the primary antibodies for the β-subunit of PDE6 and β-Actin, both diluted 1:500 in blocking buffer, followed by three washing steps in TBS-T for 5 min. The membrane was incubated with the secondary antibody which had an alkaline phosphatase (AP) conjugate diluted 1:500 in blocking buffer, followed by three washing steps in TBS-T. Finally, the membrane was developed using an AP substrate solution according to the manufacturer instructions. After the membranes dried overnight they were scanned and analyzed in Fiji (Schindelin et al., 2012). The integrated intensity of the PDE6β band divided by the β-Actin band as loading control was used as measure for the expression level of PDE6. Three Western blots were developed per lysis method to obtain technical triplicates of biological triplicates, both for WT and *rd1/+* mice. SDS-PAGE gels were stained by incubating them in InstantBlue^{TM} for 1h on a shaker after washing them with water. Then, the gels were again washed with water overnight and scanned the next day. This protocol for western blotting was established by Dr. David Salom (UCI, California, USA).

2.2.12 Mass spectrometry

Lysates obtained with mass spectrometry compatible buffers were analyzed by mass spectrometry (MS) which was conducted by the Biochemistry Core Facility at the Max Planck Institute of Biochemistry. Retina lysates were digested with LysC and Trypsin. The resulting peptides were purified, desalted, and loaded onto a column for liquid chromatography. Eluting peptides were injected by nanospray into a tandem mass spectrometer (Q Exactive HF, Thermo Fisher Scientific). The Data was processed with the MaxQuant software (Cox et al., 2008). Six independent samples where measured, three derived from WT and three from rd1/+ mice, resulting in biological triplicates for both genotypes.

Proteins were quantified across samples using label-free quantification (LFQ) intensities (Cox et al., 2014).

Table 5: List of the dataset used throughout this work.
Tilt-series were consistently acquired with a pixel size of 2.62 Å, a bidirectional tilt-scheme and a total electron dose of ~100e$^-$/Å^2.

Dataset abreviation	WT_{conv}		$WT_{VPP-inf}$	$Abca4^{-/-}{}_{VPP-inf}$	$WT_{VPP-def}$	$\mathit{rd1/+}_{VPP-inf}$
Mouse sample	Wild type		Wild type	$\mathit{Abca4}^{-/-}$	Wild type	*rd1/+*
Volta phase plate	No		Yes	Yes	Yes	Yes
Defocus (µm)	3	4.5	0	0	3	0
# Tomograms	36	12	18	6	20	5
Number of segmented connectors in 5 tomograms: rim/interior connectors						
Raw tomograms	-		800 / 6200	-	500 / 4700	1300 / 6500
Densosed tomograms	600 / 3200		600 / 4700	-	-	1000 / 6000
Disk rim subvolumes for central density (CD)						
# all subvolumes	53000		14300	4600	11800	-
# classified subvolumes	9000		11000	3400	11000	-
Global resolution (Å)	18.6		22.6	27.7	22.7	-
Processing with Warp/*M*	Yes / Yes		No / No	No / No	Yes / No	-
Disk rim subvolumes for peripheral density (CW + CCW)						
# all subvolumes	106000		-	-	-	-
# classified subvolumes	48000		-	-	-	-
Global resolution (Å)	18.2		-	-	-	-

3 Results and discussion

The results presented in this thesis are divided into several parts. First, the ROS sample was characterized, and the quality of the preparation method evaluated. Second, the characteristic distances of the ROS disk stack were measured in tomograms of frozen-hydrated ROS. Then the question is raised how the high degree of order inherent to ROS is maintained which was attributed to two key structural features: (i) the close stacking of membrane disks and (ii) the high membrane curvature at disk rims.

The next part focuses on the disk stacking. The hypothesis of interconnected disk membranes was rejected. The tomographic data suggested the existence of molecular connectors between disks. They were then picked with a customized segmentation software and statistically analyzed. The results indicated two distinct types of connectors: a short, abundant species at the disk rim and longer, scarcer connectors in the disk interior. The rim connectors were hypothesized to be GARP2 proteins and the disk interior connectors to PDE6. To confirm PDE6 as disk interior connector, ROS of a heterozygous mutant mice strain were analyzed and compared to the WT, which failed to prove the hypothesis. Then, the various cytosolic densities in ROS were studied by subvolume averaging. However, the obtained low-resolution averages reveal no structural information, likely due to the small size, the flexibility, and the heterogeneity of the proteins.

The last part characterizes the high curvature at the disk rim. Subvolume averaging resolves a repetitive protein scaffold at the disk rim. With a knockout mouse strain, it is confirmed that the scaffold is composed of PRPH2 and ROM1 proteins, likely as tetramers. Furthermore, the shape of the tetramer is described, and a mechanism of membrane curvature formation proposed. Most of the results presented here are part of the manuscript ‘The nanoscale architecture of the mouse rod outer segment’ which is not yet published by the time this thesis is written. This manuscript was a collaborative effort with the Palczewski lab (UCI, California, USA). Particularly, the ROS extraction was developed by Dr. Sanae Sakami (Case Western Reserve University, Ohio, USA). The protocol for Western Blot against PDE6 was established by Dr. David Salom (UCI, California, USA).

3.1 A novel, fast and gentle preparation method of rod outer segments for cryo-ET.

Rod outer segments (ROS) were extracted by euthanizing mice, one at a time, using carbon dioxide, followed by the removal of the eyeballs. The eyeballs were then dissected, and the lenses removed. Retinas were detached using the flux created by a pipet, collected in a tube, and suspended in Ringers buffer. Vortexing provided the mechanical disruption to detach ROS from the remainder of the retina at the junction of their thin connecting cilium (CC, Figure 11 A).

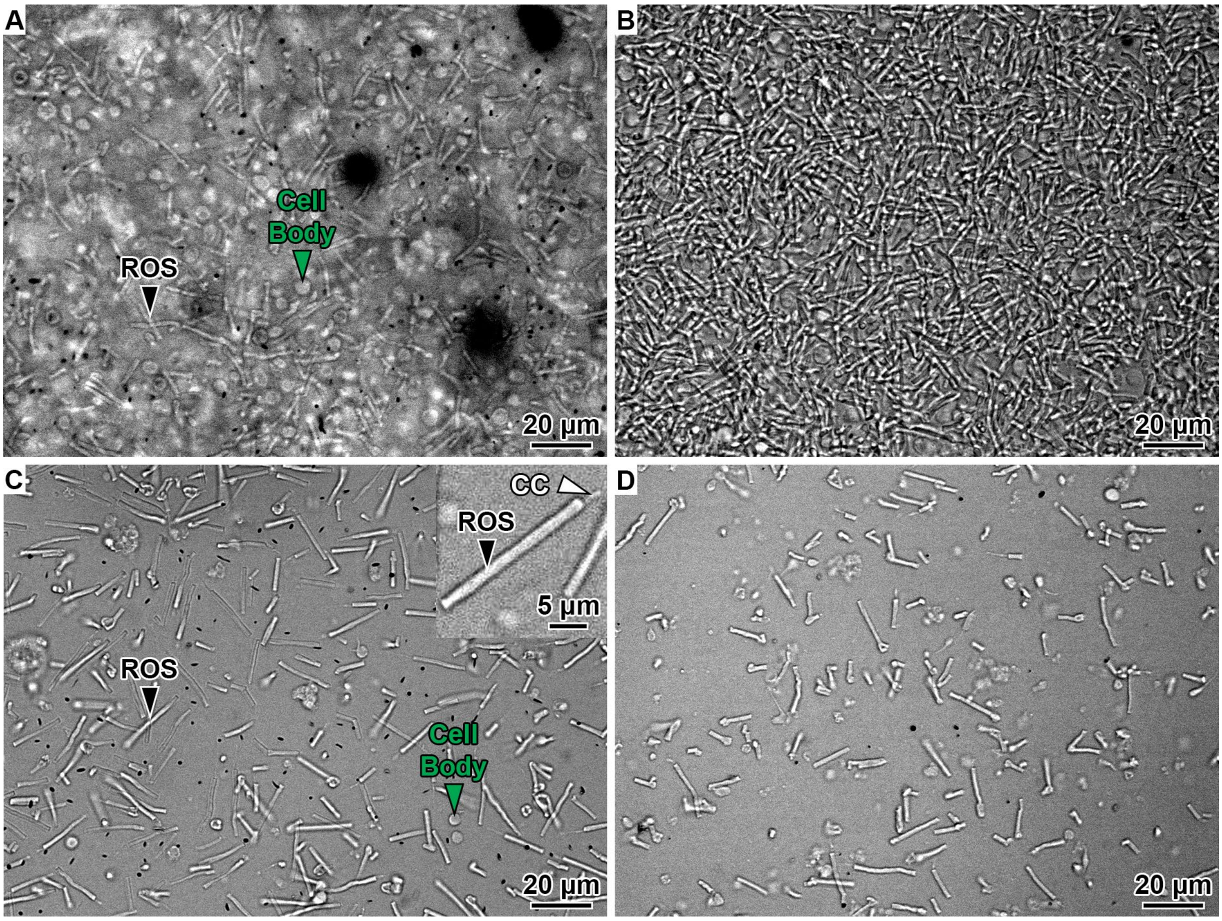

Figure 11: ROS extracts observed with light microscopy.
A) The retinal extract after physical disruption contains ROS as well as plenty of other cellular components. **B)** ROS extract after centrifugation. ROS are enriched in the supernatant. **C)** Dilution of ROS extract in B. ROS appear as straight, cylindrical structures with a length in the order of 20 µm. A small fraction of ROS are kinked or broken into shorter fragments. Inset: Magnified image of a ROS with connecting cilium (CC) attached. **D)** ROS extract depicted in C after 2h on ice. As ROS deteriorate over time the number of damaged ROS and short fragments increases.

To enrich for ROS, the retinal extract was centrifuged. Most cell bodies and inner segments were pelleted while lighter ROS remained in the supernatant (Figure 11 B). Examination of extracted ROS by light microscopy (LM) revealed intact ROS with the expected length in the order of 20 µm (Nickell et al., 2007) (Figure 11 C). Occasionally, the connecting cilium with the basal body were still attached to ROS. Additionally, some ROS were shorter or kinked, a sign of physical damage due to the sample preparation procedure (Figure 11 C). There was also a degree of contamination with other cellular components, seen as large, spherical structures. This problem was negligible for further experiments given the high concentration of ROS. As a quality control, ROS were imaged using LM. After two hours, a larger fraction of ROS was shorter or kinked (Figure 11 D) illustrating quick deteriorate of ROS. Hence, quick freezing is of vital importance and freshly extracted ROS were immediately applied to electron microscopy (EM)-grids and vitrified by plunge-freezing.

In collaboration with Dr. Andreas Schertel at Carl Zeiss SMT (Oberkochen, Germany), cryo-serial milling and block face imaging (cryo-SMBFI) (Schertel et al., 2013) was employed to characterize the frozen samples. Focused ion beam (FIB) milling repeatedly removed 15 nm of material perpendicular to the grid surface while images of the block face were acquired with a scanning electron microscope (SEM) (Figure 12 A). A section through half the width of a grid square is shown in Figure 12 B. It reveals a meniscus of frozen buffer between the carbon support and the grid bar which grows in thickness towards the edge of the grid square where it contributes substantially to the sample thickness. Milling in this area is difficult and time consuming because more material must be removed. Potentially, the material behind the target area is so thick that not all of it can be removed at the used milling angle and can cause redeposition of depleted material onto the lamella. Additionally, the higher sample thickness generates a slower heat transfer during freezing. Therefore, the ice quality decreases with the higher sample thickness close to the grid bar. Thus, areas for lamella milling were targeted in the center of grid squares.

Furthermore, cryo-SMBFI revealed that the biological sample formed a thin film on top of the carbon support. Typically, ROS were flush to the support film, meaning the axes of cylindrical ROS were parallel to the grid surface. Figure 12 C shows a block face image which illustrates the high degree of order inherent to the ROS membrane architecture. One single disk appears as a vertical black line because the two separate disk membranes could not be resolved by cryo-SMBFI. Dependent on the concentration of biological material, ROS formed mono- or multi-layers. In the case of multi-layers, ROS were stacked on top each other which partially bent ROS and locally disrupted the disk stack. An example is given in Figure 12 D where the incisure became misaligned throughout the disk stack as the ROS bent. The shear forces were strongest in regions of high curvature which caused local disruption in the stacking of disk rims. Furthermore, during blotting, the flux of buffer through the holes in the carbon support exerted strong forces on ROS. This occasionally caused whole ROS to break. In the case of Figure 12 E, one ROS was sucked through the hole of the carbon support ripping the disk stack apart. This led to distortion of the precise stacking of membrane disks throughout the entire ROS.

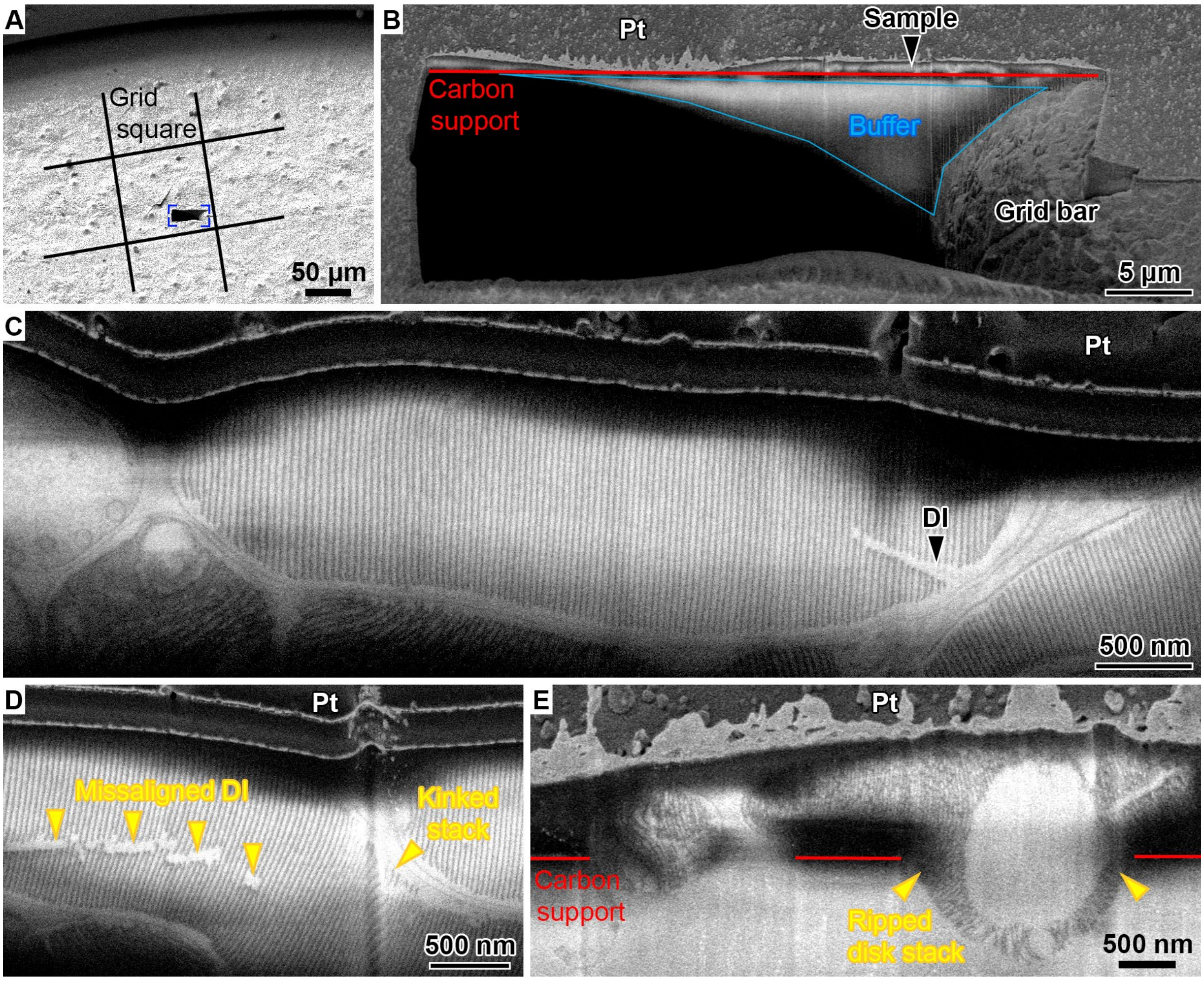

Figure 12: Cryo-serial milling and block face imaging of isolated, frozen ROS on EM-grids.
A) SEM overview image of a grid. The black hash marks the outline of the grid square. The blue frame indicates the field of view in B. **B)** Block face image of a cross-section spanning half the width of a grid square. The carbon support is marked by a red line. The meniscus of frozen buffer between support and grid bar is outlined in light blue. Pt indicates the layer of protective organo-metallic platinum. **C)** Cross-section of ROS with well-preserved disk stack. DI denotes the disk incisure. **D)** Multi-layers of ROS. ROS lying across one another can cause individual ROS to bend which distorts the disk stack. **E)** Monolayer of ROS. During blotting, the ROS was sucked through a hole in the carbon support. The disk stack ripped in the process and membranes were distorted throughout the ROS cross-section.

Isolated ROS on EM grids are too thick for data acquisition in a transmission electron microscope (TEM). Therefore, it was necessary to thin down the biological material to electron transparency. Thin sheets of the material, so-called lamellae, were prepared by FIB-milling (Schaffer et al., 2017). For this, the samples were loaded into a dual beam, cryo FIB and SEM microscope. After applying a conductive layer of metallic platinum (Pt), ROS could be identified as flat, elongated structures in images acquired with the SEM (Figure 13 A) and the FIB (Figure 13 B). Contamination by other retinal components, like cell bodies, appeared as spherical objects. Areas with several adjacent ROS were targeted for lamella milling. The final lamellae had thicknesses between 100 and 250 nm (Figure 13 C and D), allowing for TEM data acquisition with high signal-to-noise ratio.

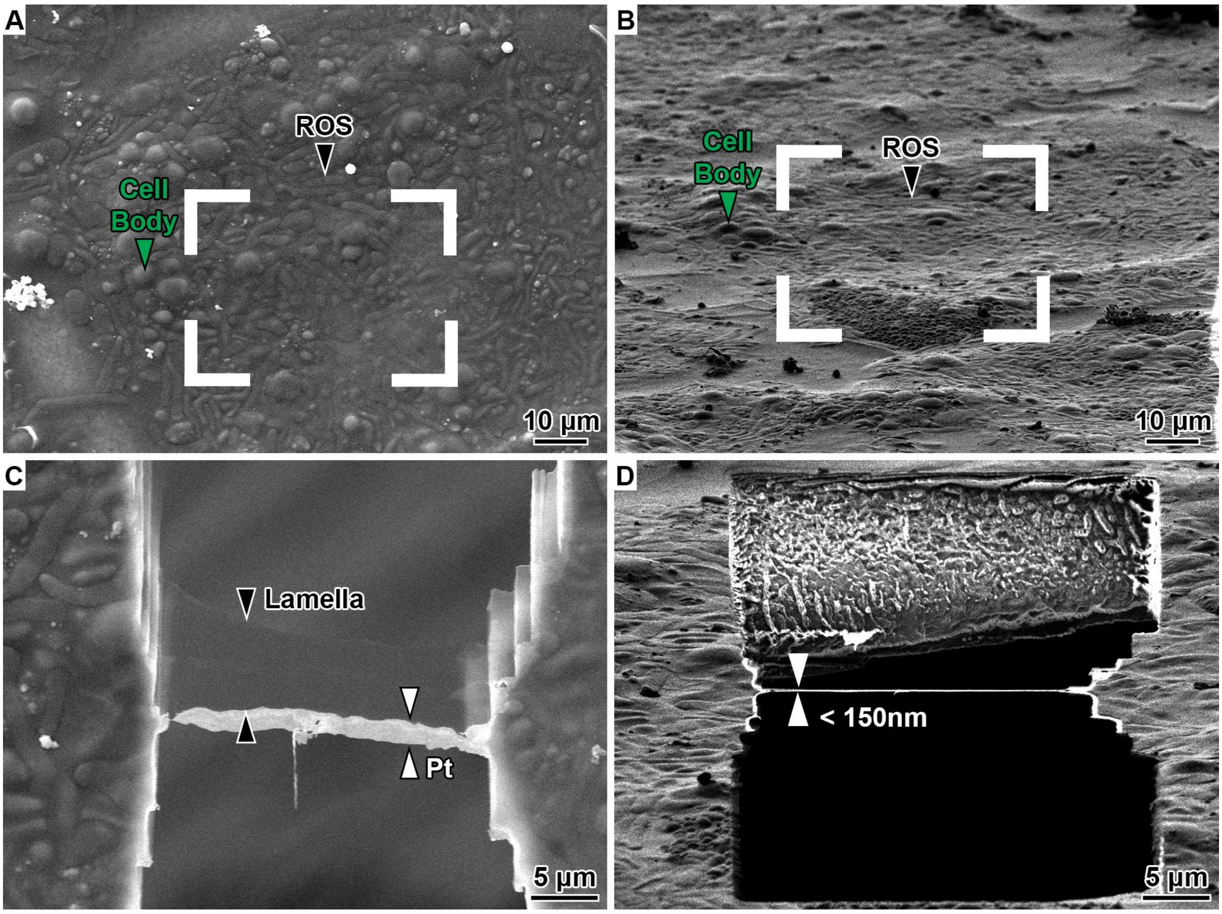

Figure 13: FIB-milling of vitrified ROS.
A) and **B)** SEM and FIB images of grid square before milling, respectively. ROS appear as elongated, sausage-like structures, cell body contaminants as spherical objects. **C)** and **D)** SEM and FIB images of areas outlined in A and C after milling, respectively. Pt indicates the protective layer of organo-metallic Platinum.

Figure 14 A shows a low magnification TEM image of a lamella section. Six parallel oriented ROS are within the field of view, partially indicating the highly ordered stack of membranes characteristic of ROS. While the two ROS in the middle are well preserved, the neighboring ROS show local damage, which appears as imperfection in the disk stack. The three typical types of damage are (i) kinks when the ROS axis abruptly changes, (ii) distorted membranes or (iii) inconsistent distances within the disk stack between neighboring disks or disk rims and the PM.

In agreement with LM and cryo-SMBFI data, damage to ROS can be attributed to the following sources:

1. Detachment of the retina from the back of the eyeball.
2. ROS deterioration, which occurs quickly after ROS extraction.
3. The physical disruption, done to pinch ROS off the retina and pipetting of extracted ROS.
4. Multi-layers of ROS on the grid and forces during blotting distort the disk stack or rupture entire ROS.

The presented cryo-preparation method of isolated ROS is faster and gentler to the tissue than previously reported methods (Nickell et al., 2007). It is economical as it requires only a single mouse for the preparation of more than 10 grids. Isolated ROS are thin enough to assure proper vitrification by plunge-freezing on EM-grids. Vitrified ROS are readily thinned to electron transparency by FIB-milling.

The method, however, is not perfect, as illustrated by the ROS damage in Figure 14 A. High pressure freezing of the entire retina would avoid most sources of damage. However, thinning the retina tissue by cryo-sectioning introduces compression artifacts (Gunkel et al., 2015) and lift-out methodologies would substantially lower the throughput (Schaffer et al., 2019). Since the ROS damage was confined locally, the presented ROS preparation method still allowed the study of the molecular architecture of ROS in a close-to-native state.

Tomographic tilt-series were acquired in areas with well-preserved disk stack and with several dense platinum particles in the field of view (Figure 14 B). The platinum particles are pieces of the protective organo-metallic Pt layer which were occasionally deposited on the lamella during milling. They were used as fiducials in later processing steps for tilt-series alignment. Fiducial were necessary because patch tracking algorithms failed to align the tilt-series due to the repetitive signal of stacked ROS membranes.

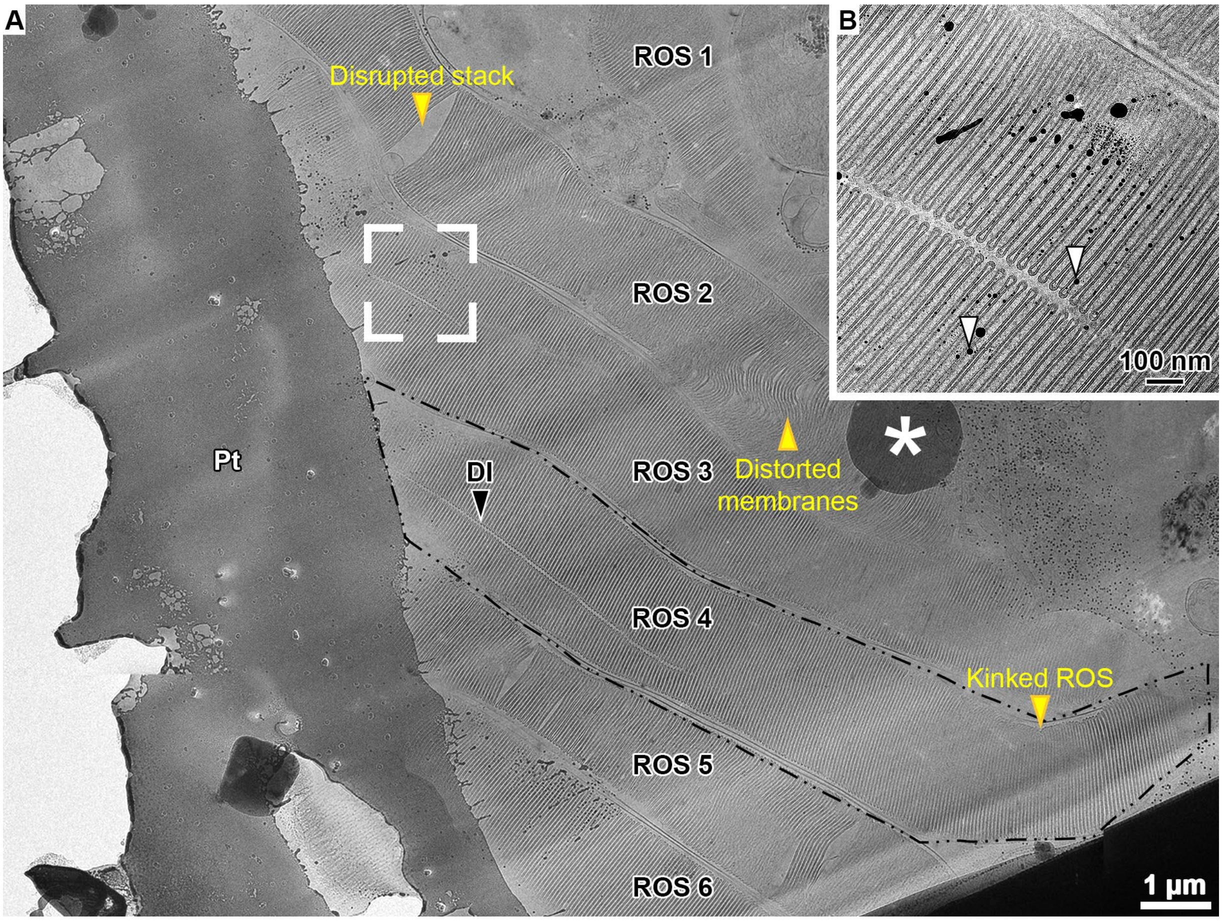

Figure 14: Fraction of the low magnification TEM overview image of a lamella.
A) Fraction of a lamella overview image. It comprises six parallelly oriented ROS. One ROS is outlined in black. Areas with ROS damage are marked by yellow arrow heads. Pt denotes the protective layer of organo-metallic platinum, DI the ROS disk incisure, the white asterisk ice crystal contamination. Tomographic tilt-series were only acquired in areas without obvious ROS damage like the area outlined in white. **B)** projection of a tilt-series acquired on the white framed area in A. Platinum particles which were deposited on the lamella during milling are indicated with white arrow heads.

3.2 Imaging and characterization of the ROS disk stack.

Tomogram acquisition of intact ROS derived from wild type (WT) mice was performed using two acquisition methods: (i) conventional tilt-series taken with defocus ($\mathrm{WT_{conv}}$, Figure 15 A) and (ii) tilt-series taken with Volta phase plate (VPP) in focus ($\mathrm{WT_{VPP\text{-}inf}}$, Figure 15 B). Both acquisitions schemes allowed the visualization of the ROS membrane architecture However, compared to the conventional tomograms, the use of the VPP enhanced the contrast. This allowed for direct observation of cytosolic protein densities in the reconstructed tomographic volumes.

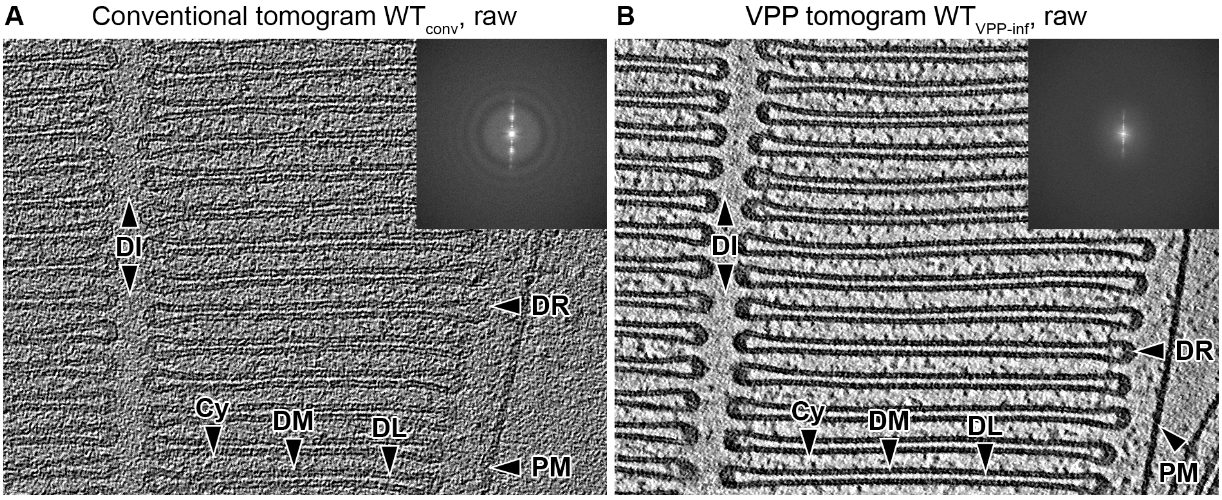
A Conventional tomogram $\mathrm{WT_{conv}}$, raw

B VPP tomogram $\mathrm{WT_{VPP\text{-}inf}}$, raw

C $\mathrm{WT_{conv}}$, denoised with Cryo-CARE

D $\mathrm{WT_{VPP\text{-}inf}}$, denoised with Cryo-CARE

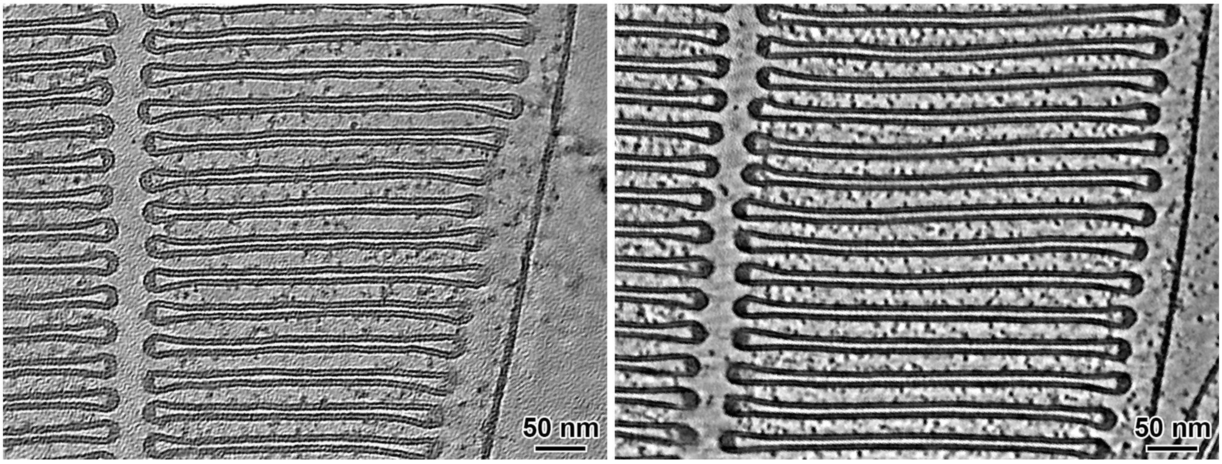

Figure 15: Tomographic volumes of ROS.
A) and **B)** are slices of WT ROS tomograms acquired conventionally with 3 µm defocus ($\mathrm{WT_{conv}}$) and with Volta phase plate (VPP) in focus ($\mathrm{WT_{VPP\text{-}inf}}$), respectively. The highly ordered ROS membrane architecture is resolved with plasma membrane (PM), disk rims (DR), disk membranes (DM), disk lumen (DL), disk incisure (DI) and cytosol (Cy). Insets show power spectra of the zero-degree projection in the tilt-series. **C)** and **D)** are the same tomographic slices as in A and B after denoising with Cryo-Care (Buchholz et al., 2019).

Denoising of the tomograms using Cryo-CARE (Buchholz et al., 2019) enhanced the interpretability of data collected in both cases (Figure 15 C and D). Especially for $\mathrm{WT_{conv}}$, the denoising algorithm recovered the cytosolic densities and generated contrast similar to VPP tomograms (Figure 15 D).

The tomograms resolved the ultrastructural organization of the ROS disk membranes. The disk stacks show the expected order over a range of several micrometers. In contrast to EM studies of plastic embedded ROS sections (Corless & Schneider, 1987), the parallel membranes planes of disks appear straight, the disk rims next to the plasma membrane (PM) and at the incisure are aligned throughout the stack and the spacing of all ROS components is consistent. This illustrates the superior sample preservation of plunge-freezing over traditional techniques involving plastic-embedding. The stack can be described as a 1D membrane crystal with translational symmetry along the ROS axis and a unit cell distance of 32 nm. The asymmetric unit comprises two parallel membranes separated by the disk lumen and the cytosolic space between two adjacent disks. Amplitude spectra of projections perpendicular to the disk stack show clear peaks, emphasizing the high degree of order (Figure 16 A). However, the distinct peaks only reflect the basic unit cell distance as multiples of (32 nm)$^{-1}$.

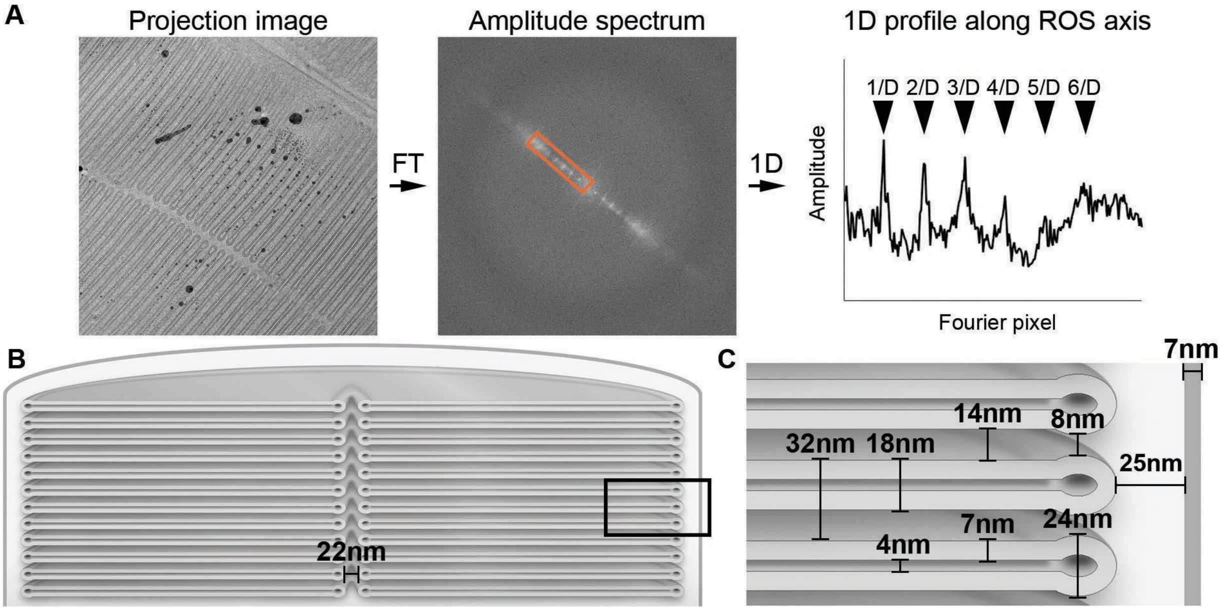

Figure 16: Characteristic distances of the ROS disk stack.
A) The amplitude spectrum (middle panel) of a 4x binned projection image (left panel) exhibits distinct peaks parallel to the ROS axis. The right panel shows the 1D profile along this direction (orange box in middle panel). The peaks occur at multiples of (32 nm)$^{-1}$ which reflects the distance between unit cells along the disk stack. **B)** and **C)** Sketch of ROS cross-section drawn to scale with the characteristic distances measured in real space. The box in B indicates the field of view in C.

All other distances were measured in real space and are summarized in Figure 16 B and C. The disk lumen separates the two membranes within the disk by 4 nm. The width of the cytosol between two adjacent disks is 14 nm and narrows to 8 nm at the disk rims. Other characteristics distances are the 22 nm gap at the disk incisure and 25 nm between disk rims and the PM. At the disk rim the membrane bilayer is bent to a radius of 24 nm which is amongst the highest membrane curvatures reported to date (Jarsch et al., 2016). The measured thickness of ROS membranes was 7 nm. Previous reports using x-ray diffraction (Wilkins et al., 1971) or cryo-EM (Cornell et al., 2020; Heberle et al., 2020) elucidated membrane thickness around 4 nm. This discrepancy is likely caused by the following aspects:

1. Here the membrane thickness was defined as the width at half the maximum intensity across the membrane while previously it was measured as the distance between the two peaks assigned to

the lipid headgroups (Heberle et al., 2020). The acquired TEM images are convoluted with the PSF of the microscope, leading to a delocalization of information and therefore to an uncertainty for both methods. The results with the peak distance method were closer to the expected membrane thickness of ~4 nm. This method, however, could not always be applied because in some cases the two membrane leaflets were not resolved separately. In contrast, the full width at half maximum as threshold to measure membrane thickness could be apllied consistently throughout the datasets.

2. ROS membranes contain a high concentration of Rhodopsin (Rho), a transmembrane protein with a height of approximately ~7 nm. Additionally, other proteins are often embedded in the membrane or tightly associated with it. Thus, the measured membrane thickness could be an average of the actual membrane thickness plus membrane embedded or associated proteins, yielding a membrane that appears thicker than expected. Previously, the impact of membrane proteins on the measured membrane thickness has been reported for solution x-ray scattering experiment (Mitra et al., 2004).

Apart from the membrane thickness, the estimated distances are in excellent agreement with previous studies in mammalian ROS (Nickell et al., 2007) and further refined the measurement to the nanometer scale. Furthermore, the precise distance measurements with corresponding standard deviation are listed in Table 6. the These distances define the 3D spatial framework of the signal cascade following Rho activation. For this reason, this information is vital for the interpretation of available data on diffusion dynamics associated with phototransduction (Calvert et al., 2001).

Table 6: List with distances of the ROS disk stack.
The sketch below assigns the letter in the list to a specific distance with the corresponding mean value (mean) and standard deviation (std).

Distance	A	B	C	D	E	F	G	H	I	J
Mean (nm)	21.7	32.1	17.7	4.1	14.4	6.8	8.1	24.0	24.5	6.8
Std (nm)	5.1	1.9	1.3	0.7	2.1	0.8	2.5	0.6	5.4	0.6

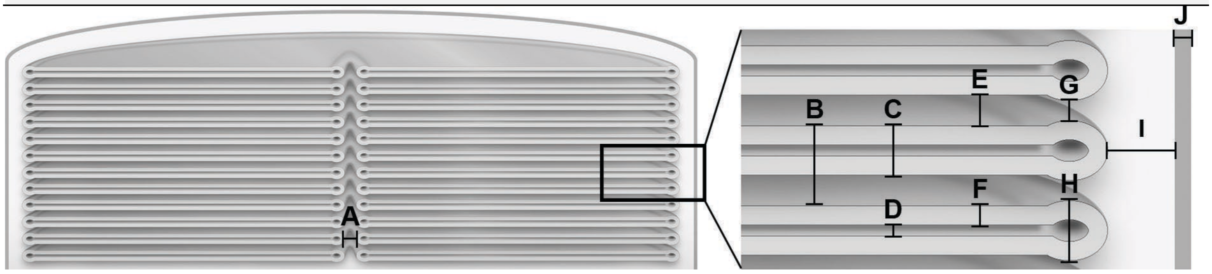

3.3 Membranes of neighboring ROS disks are not interconnected.

A question that remains is how the precise spacing between ROS disk is maintained over the scale of several microns. Previously, it has been proposed that spacing is mediated by membrane connectivity of adjacent disks (Robertson, 1965). This model was derived from 2D micrographs of heavy metal stained, plastic embedded ROS sections which showed zipper-like structures (Figure 17 A). Similar patterns were found in high dose cryo-EM micrographs (Figure 17 B) and single projection images of tilt-series (Figure 17 C).

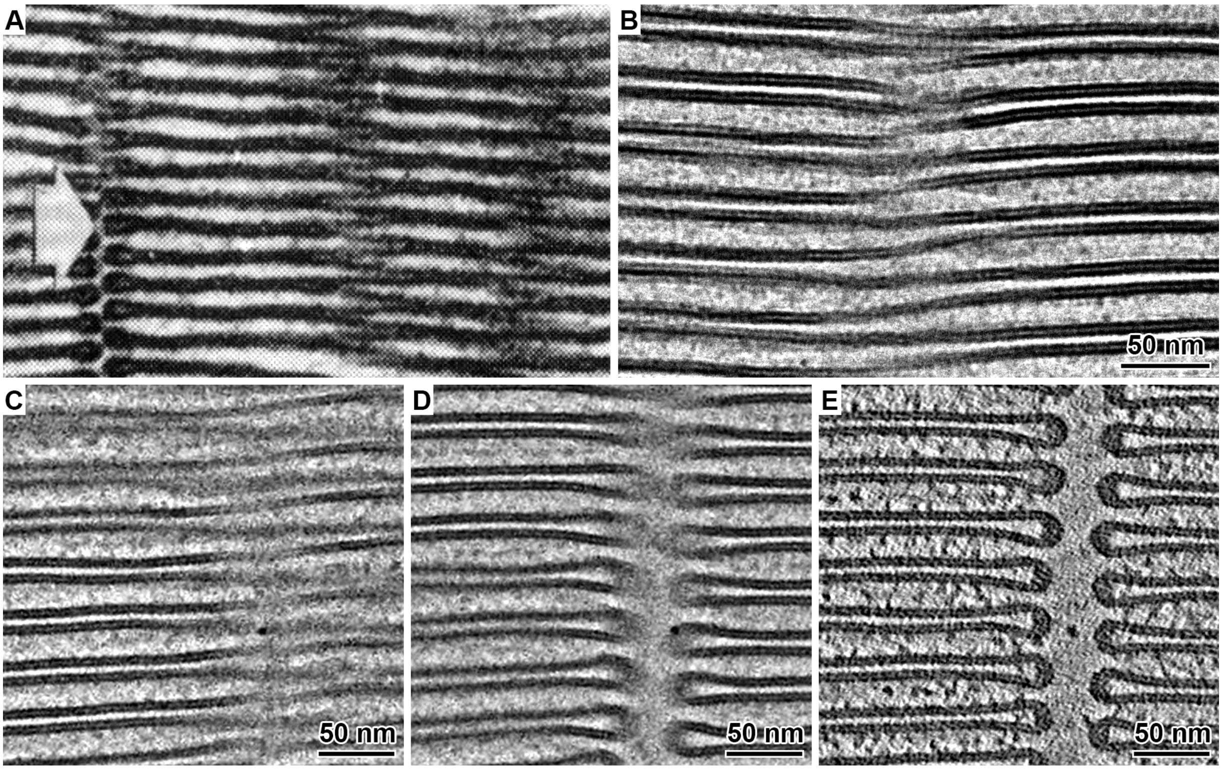

Figure 17: Disk membrane connectivity as artifact of the 2D projection through the disk incisure.
A) Micrographs of a metal stained, plastic embedded ROS section showing a zipper-like pattern. Adapted from (Robertson, 1965). **B)** and **C)** similar patterns in frozen-hydrated ROS observed in micrographs with longer exposure and single projection images of tomographic tilt-series, respectively. **D)** Field of view as in C but tilted 20°, resolving the incisure. **E)** Slice of tomographic volume in the area of C and D. Neighboring disks are not connected.

Compared to Figure 17 A, the lower contrast in B and C is due to the cryo-preparation, which does not use contrast enhancement by metal staining. Here, the contrast arises primarily from phase contrast. Furthermore, non-stained, biological samples are sensitive to radiation damage, which requires imaging at low electron doses (20 and 1.5 $e^{-}/Å^{2}$ in Figure 17 B and C, respectively). Projection images acquired in the same area as Figure 17 C but at a different tilt angle revealed that the zipper-like pattern is a misinterpretation of the 2D projection through the disk incisures (Figure 17 D). The pattern appears only in a few projections of successive tilt angles when two conditions are fulfilled:

1. The rims on adjacent sides of the incisure have an offset in the plane of the projection.
2. The incisure is inclined with respect to the direction of the projection in a way that it is not yet resolved as the characteristic gap in the disk stack.

Tilting of a few degrees violates these conditions causing the pattern to disappear and, eventually, the incisure to become fully resolved. Tomographic reconstruction confirmed that the membranes are not interconnected in these areas (Figure 17 E). An example can be seen in the original publication (Figure 17 A) marked by the white arrow. Below the arrow, the disk incisure is fully resolved as it is not inclined with respect to the direction of the projection. However, above the arrow it bends within the ROS section and appears in the projection as the zipper-like pattern. This demonstrates the power of tomography which provides reliable 3D information of the biological sample and avoids misinterpretation of 2D projections.

3.4 Segmentation and analysis of connectors between disks.

Another proposed mechanism to maintain the membrane proximity in the disk stack is that there are molecular connectors between disks (Nickell et al., 2007; Roof et al., 1982). Depicted below are structures connecting membranes of two adjacent disks that were clearly identified in tomograms of WT ROS acquired with VPP in focus ($WT_{VPP\text{-}inf}$, Figure 18 A). These structures became even more apparent when the tomograms were filtered with a gaussian kernel (σ = 4 voxels, Figure 18 A) but were barely distinguishable in the raw or filtered conventional tomograms (WT_{conv}, Figure 18 B). Connectors in proximity to disk rims were most obvious, both at the outer periphery of the disks (Figure 18 C) and at the disk incisures (Figure 18 D). Often rim connectors linked rims of several consecutive disks that they appeared like thread stitching together several disks. In addition, connector densities were found more scarcely between the parallel membranes in the disk interior (Figure 18 E).

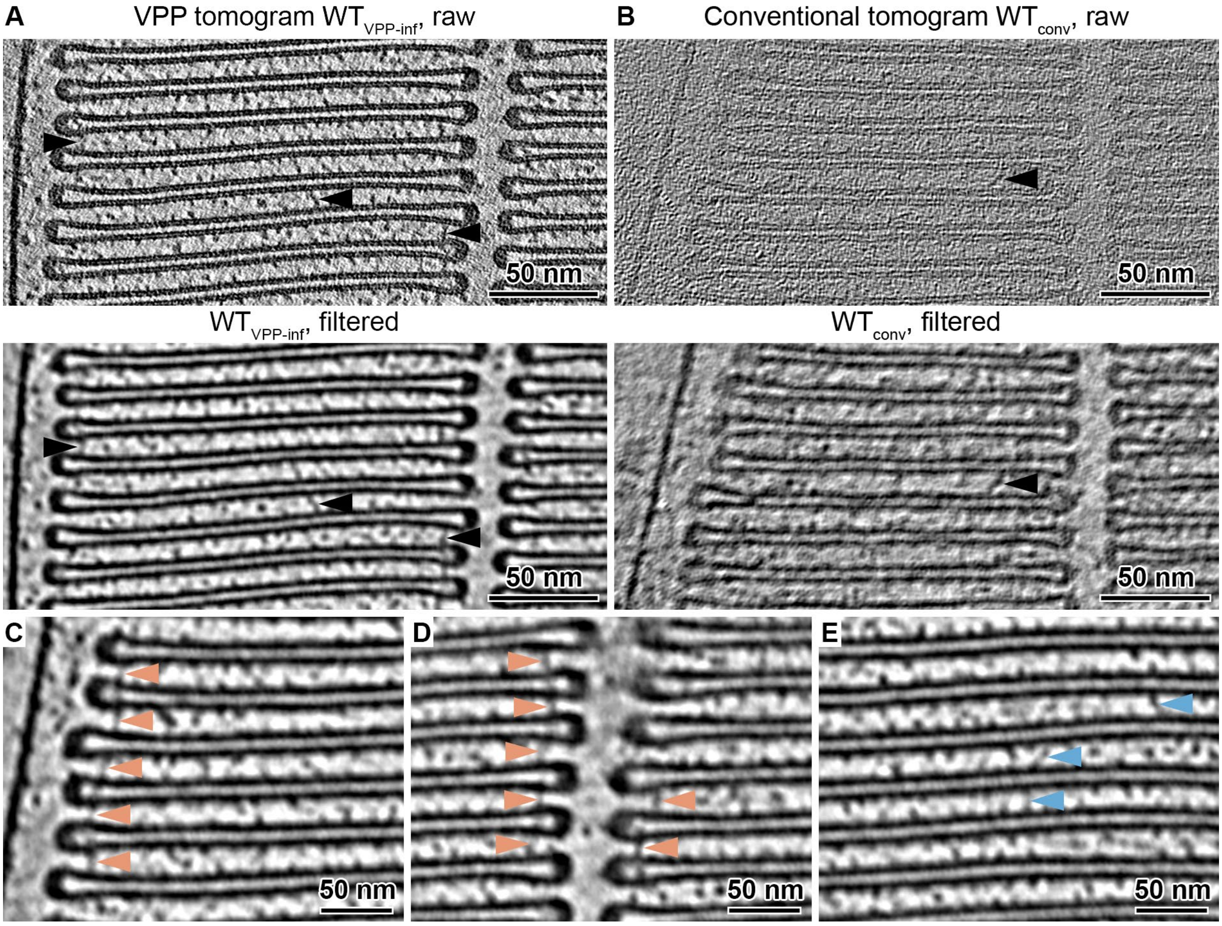

Figure 18: Observation of disk connectors in raw and filtered tomograms.
A) and **B)** slice of raw (top panel) and filtered tomogram (bottom panel) of data acquired with VPP in focus ($WT_{VPP\text{-}inf}$) and conventionally (WT_{conv}), respectively. Black arrowheads indicate connectors which can be distinguished in raw and filtered tomograms. **C-E)** Connectors in filtered $WT_{VPP\text{-}inf}$ tomograms at the disk rim opposite of the plasma membrane in C, at the disk rims of the incisure in D and between the parallel disk membranes in the disk interior in E.

3.4.1 Customization of the Pyto software for enhanced connector segmentations in ROS tomograms.

Connectors between disks could be identified by visual inspection in the raw $WT_{VPP\text{-}inf}$ tomograms due to the high quality of the dataset. This allowed the use of the Pyto software (Lučić et al., 2016) to segment connectors. Pyto requires a segmentation of the disk membranes to define the borders of the cytosolic space which a connector must bridge. Pyto runs a grey scale ramp at a custom set interval starting from a low (dark) grey value threshold with given increment to a maximum threshold. At each step, a connectivity segmentation is performed. First, all voxels with values below the current grey value are selected by thresholding. Then, only those interconnected groups of voxels are identified which are in contact with the two membranes of neighboring disks, thus spanning the space between them. The final output contains only connectors at the threshold when they were first segmented. This is a robust approach. Compared to a connectivity segmentation with a single threshold, Pyto allows picking of connectors with minimal volume and the results are not impaired by contrast variations throughout the tomographic volume, i.e., by changes of the sample thickness.

However, comparing the number and size of the segmented connectors to the raw data revealed that too few connectors were picked, and their volumes were larger than expected (Figure 19 A). The overall problem was the continuity of several individual connectors. At the pixel size of ~1 nm, at which the segmentation was performed, some close-by connectors were not fully resolved as separate structures. Furthermore, the membrane masking was not perfect, particularly in the curved area of the disk rim. Unmasked membrane appeared as dark patches with low grey value that linked several distinct connectors together. This had consequences for the automated segmentation (Figure 5 A). Often, two or more connectors that could be identified by eye as separate structures, were picked as one, yielding volumes that were bigger than expected. Additionally, some brighter connectors were linked to darker connectors. When the brighter connectors were selected first by thresholding, they were segmented in contact with the darker connector that was already selected at a lower threshold. Only this single dark connector appeared in the segmentation results while the brighter connector was discarded, due to the hierarchical segmentation scheme implemented in Pyto. It is important to mention that connectors could not be segmented in filtered tomograms. Even though connectors appeared there less noisy and well pronounced (Figure 18 C-E), the convolution with a Gaussian was spreading the connector densities over a larger volume. This caused nearby connector densities to fuse which prevented to resolve them as separate structures by segmentation.

To circumvent the problem of contacting connectors, an additional masking step was applied before running Pyto on raw tomograms (Figure 5 B). First, a binary mask was created that comprised all voxels with values below the highest (brightest) grey value of the Pyto grey value ramp. This mask was then subjected to the watershed transform (Meyer, 1994) with “catchment basins” filled from the center between the membrane masks. The resulting watershed lines separated large densities composed of several connectors. This mask was applied to the tomographic volume before running the segmentation with Pyto (Figure 19 B).

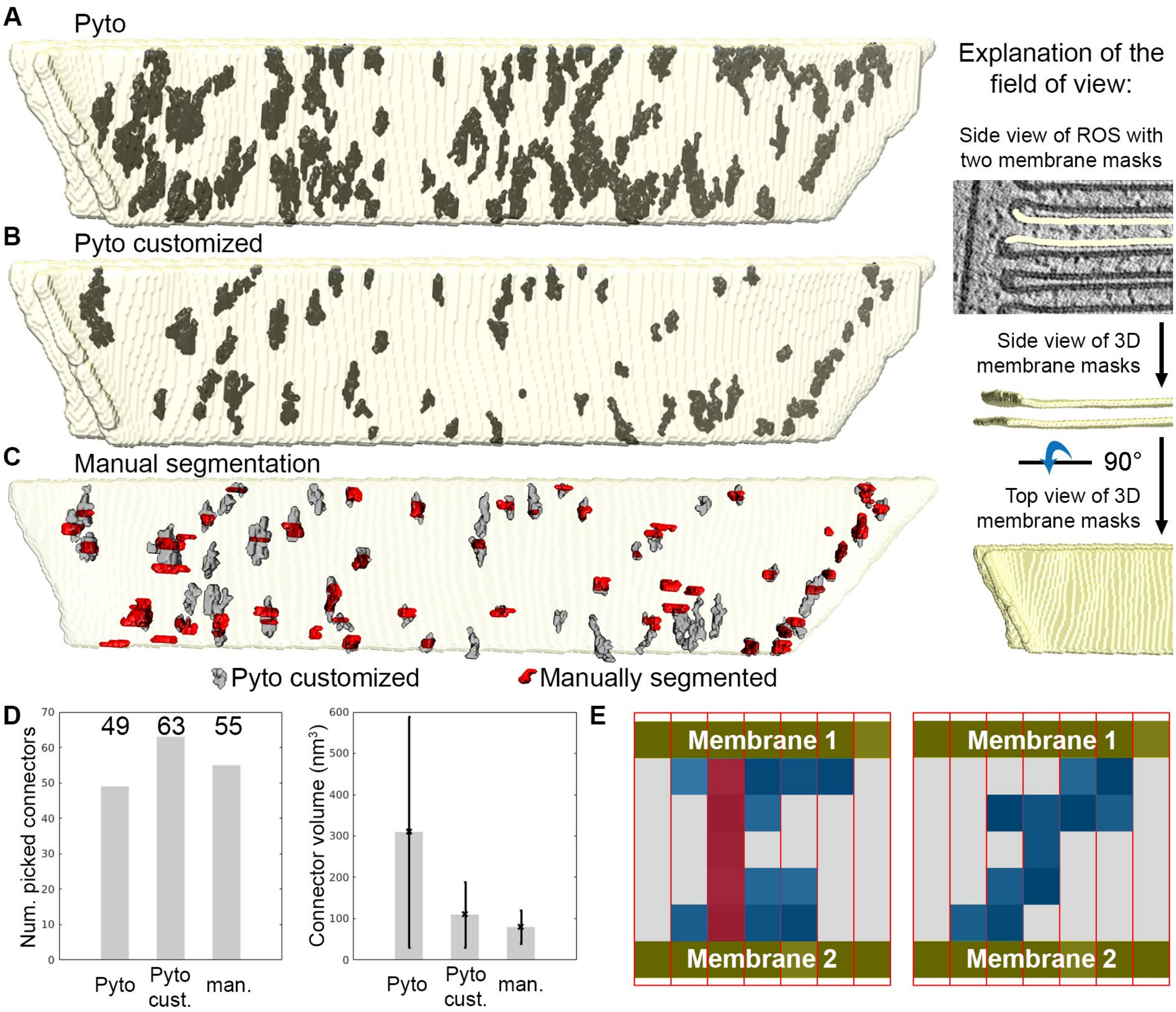

Figure 19: Connector segmentation for one pair of disk membranes viewed from the top. **A)** Segmentation Results of the original Pyto workflow. The neighboring membranes of adjacent disks are depicted in yellow. They are viewed from the top (along the ROS axis). The segmented connectors are black. **B)** Results with the customized Pyto workflow. **C)** Comparison of results in B with manual segmentation. The right panel explains the viewing direction in A-C. **D)** Number of picked connectors and average connector volume throughout the segmentation methods. **E)** Sketch of connectors to illustrate the reason for difference between manual and automated segmentation. The membrane pair is viewed from the side (perpendicular to ROS axis). Red rectangles represent tomographic slices. Manually and automatically segmented voxels are filled red and blue, respectively. The membranes are yellow. The Left panel indicates why manual selected connectors have a smaller volume. The right panel illustrates an inclined connector. In none of the slices it is observed as straight connector. Therefore, it can be missed in the manual segmentation.

To assess the quality of the customized Pyto segmentation approach, the results were compared to a manual segmentation (Figure 19 C). Two major differences are apparent (Figure 19 D): First, the connectors selected automatically were bulkier than manually picked connectors. This is caused by the algorithm that picks voxels based on their grey value and their connectivity and evaluates all voxels at once, not in a slice-by-slice manner (Figure 19 E). Second, fewer connectors were picked manually. This is likely due to inclined structures, which were not observed as connectors in one single tomographic slice, but several successive slices. Consequently, they could be missed manually (Figure 19 E). Therefore, picking of connectors with the automated segmentation approach is more reliable than the manual segmentation. 90% of the connectors were picked by both methods and the error of the determined connector coordinates was below 2 nm. This error is small compared to the pixels size of 1 nm and the size of membrane patches with diameters of 500 to 1000 nm. Overall, the shapes of connectors segmented in noisy tomograms are not reliable and additional variability is likely caused by their flexibility. However, they could be picked with the customized Pyto workflow and their arrangement analyzed in 3D.

3.4.2 Two distinct types of connectors exist between disk membranes of wild type mice.

The customized segmentation with Pyto was used on 5 tomograms of the $WT_{VPP\text{-}inf}$ dataset. The total number of 7000 picked connectors were divided based on their proximity to the disk rim into two groups: 800 disk rim connectors, residing within 40 nm from the outer periphery of the disk rim, and 6200 disk interior connectors, located at the remaining membrane surface (Figure 20 A). Statistical analysis indicated that rim connectors have shorter nearest-neighbor distances (Figure 20 B), are shorter (Figure 20 C) and have a lower grey value, i.e. represent a more dense structure (Figure 20 D) when compared to the disk interior connectors. These results imply the existence of two distinct structures forming the connectors. Furthermore, the density of 190 and 920 molecules per μm^2 disk membrane was calculated for the disk rim and interior connectors, respectively (Figure 20 E).

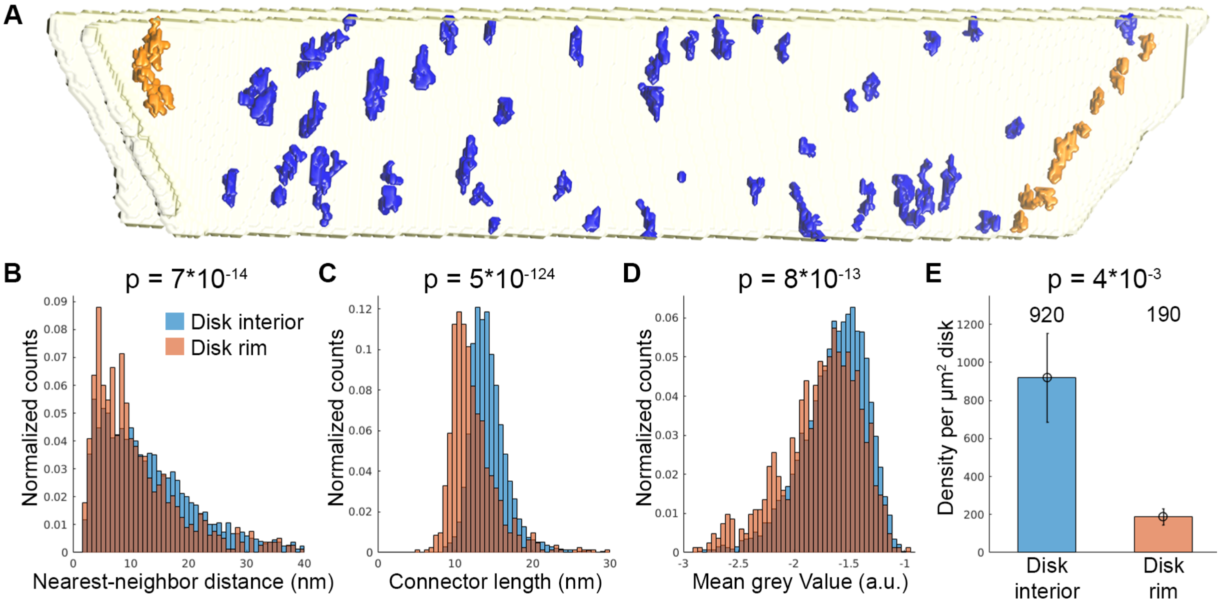

Figure 20: Statistical analysis of disk connectors in WT mice.
A) Definition of connector types on the example of one membrane pair viewed from the top (along ROS axis). Connectors within 40 nm of the outer disk periphery were defined as disk rim connectors (orange), connectors in between the parallel membrane planes as disk interior connectors (blue). **B-D)** Statistical analysis of connectors. Normalized histograms of the nearest-neighbor distances in B, the connector length in C and the mean grey value in D indicate significant differences between the two species. **E)** Connector density per µm² of disk membrane. All p-Values were calculated according to the two sample Kolmogorov-Smirnov test.

The presented segmentation does not allow to determine the molecular identity of the disk connectors. Therefore, the segmentation results in combination with available data on ROS proteins were used to hypothesize. The most prevalent ROS proteins have been quantified previously (Kwok et al., 2008; Skiba et al., 2013) and their positions within ROS localized (Goldberg et al., 2016). Furthermore, the potential candidates for molecular connectors must fulfill the following criteria:

1. Connectors must be transmembrane, or membrane-associated proteins.
2. The abundance should agree with the results of the segmentation.
3. They must have a sufficiently large cytosolic domain or the tendency to form oligomers to span the gap between adjacent disks.
4. Connectors are suspected to be of importance for the structural integrity of ROS. Therefore, the mutation of genes for the protein were expected to cause phenotypes with disordered ROS.

With these criteria at hand, the literature was searched for potential protein candidates for the connectors. The *CNGB1* gene encodes three glutamic acid-rich proteins (GARPs) (Colville et al., 1996): the β-subunit of the cyclic nucleotide gated (CNG) cation channel and the alternatively-spliced proteins GARP1 and GARP2. All three GARPs are exclusively localized to disk rims (Körschen et al., 1999) or the ROS PM. The CNG channel mediates the cation conductance of the ROS PM in response to light (Colville et al., 1996; Pugh et al., 2000). GARP1 and GARP2, on the other hand, are soluble proteins which are tightly bound to membranes under physiological conditions by an unknown mechanism (Körschen et al., 1999). Loss of CNG channels has only a minor impact on the ROS architecture and does not perturb ROS morphogenesis (Hüttl et al., 2005). However, knockout of all three GARP-proteins destabilizes the diameter of the disks and results in the misalignment of disk rims throughout the disk stack (Y. Zhang et al., 2009). These results suggest that of the three GARP isoforms, only GARP1 and GARP2 might be involved in the organization of the disk stack and more specifically its outer periphery. The estimated abundance of GARP2 is with ~500 molecules per μm^2 disk in the order of the 190 disk rim connectors per μm^2 estimated by the segmentation, while GARP1 is 20x less abundant (Batra-Safferling et al., 2006). Still, the density of disk rim connectors is less than expected for GARP2 and the hydrodynamic radius of GARP2 was determined to be ~5 nm (Batra-Safferling et al., 2006) is too small to span the 8 nm gap between disk rims. However, sedimentation experiments of GARP2 suggest an equilibrium between GARP2 monomers, dimers, and tetramers. Therefore, it is possible that GARP2 proteins connect adjacent rims as oligomers which makes them a good candidate for the disk rim connectors.

On the other hand, absence of all GARP isoforms and thus the putative disk rim connector does not abolish disk stacking (Y. Zhang et al., 2009). Presumably, a connector in the disk interior can compensate for this function. A plausible candidate for the disk interior connector is phosphodiesterase 6 (PDE6). It is a 215 kDa enzyme involved in phototransduction. PDE6 is a heterotetramer composed one α- and one β-subunit, both catalytically active, and two small, regulatory γ-subunits (Figure 21 A). The C-termini of both catalytic subunits are anchored to one disk membrane (Pugh et al., 2000). The distance from the C- to the N-termini is around 15.4 nm (Gulati et al., 2019), allowing PDE6 to bridge the space of 14.4 nm between adjacent disks (Figure 21 B). However, whether PDE6 forms of such a connector, how its N-termini interact with the membrane and whether this is of structural relevance for ROS remains to be elucidated. It is clear, that the N-termini of the PDE6 α- and β-subunit are exposed to the neighboring disk membrane. Several scenarios are plausible for protein-membrane interactions. The N-terminal loops of PDE6 contain non-polar resides (Figure 21 C) which could directly insert into the membrane or form an amphipathic helix. However, these interactions typically induce membrane curvature which is not observed for the parallel disk membranes in the disk interior. On the other hand, peripheral membrane proteins can interact with membranes in various other ways for example via the lipid head groups (Monje-Galvan et al., 2016). Co-sedimentation or co-floatation assays (Mattila et al., 2007; H. Zhao et al., 2012) with vesicles comprising the precise lipid composition as ROS disk membranes (Poincelot et al., 1970) can probe the putative interactions of the PDE6 N-termini with membranes. Molecular dynamics simulations can then provide further insights how this interaction is established at the molecular level (Hollingsworth et al., 2018; Monje-Galvan et al., 2016). The importance of this interaction for the structural integrity of ROS can be tested with N-terminal truncation mutants of PDE6. In these mutant strains a phenotype with distorted ROS or impaired ROS formation would be expected. However, to make this conclusion, it must be assured that the truncated PDE6 is still catalytically active because it is known that inactive but otherwise structurally intact PDE6 already induces retinal degeneration (Chang et al., 2002).

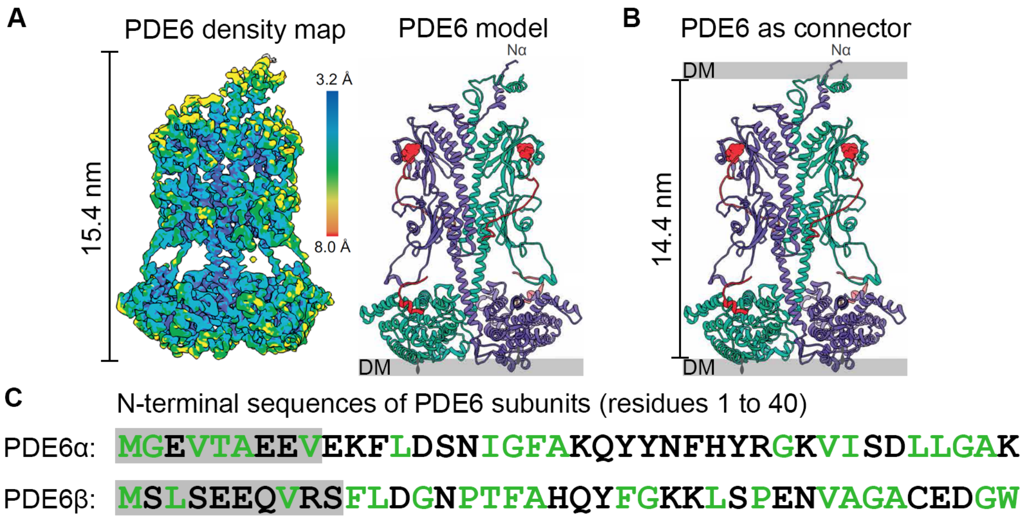

N-terminal sequences of PDE6 subunits (residues 1 to 40)

PDE6α: MGEVTAEEVEKFLDSNIGFAKQYYNFHYRGKVISDLLGAK

PDE6β: MSLSEEQVRSFLDGNPTFAHQYFGKKLSPENVAGACEDGW

Figure 21: Hypothesis of PDE6 as disk interior connector:
A) Cryo-EM density map (left panel) and model (right panel) for PDE6 adopted from (Gulati et al., 2019). In the model, PDE6α is depicted in purple, PDE6β in cyan and PDE6γ in red. Disk membranes (DM) are shown in grey. **B)** Hypothesis of PDE6 as connector. PDE6 is known to be attached by the lipid modified C-termini of its α- and β-subunit to one disk membrane. It is large enough to span the distance between adjacent disk and its N-terminus may link it to the neighboring disk membrane. **C)** The 40 N-terminal residues of the PDE6 α- and β-subunit (UniProtKB P27664 and P23440, respectively). Non-polar residues are marked in green. Residues which are not included in the model in A are boxed in grey.

The segmentations indicate a 1:5 ratio of the putative GARP2 rim connectors and the interior PDE6 densities, while they are known to be present at equal amounts in ROS (Batra-Safferling et al., 2006). This supports the hypothesis that GARP2 forms oligomers *in vivo* to span the 8 nm space between rims of adjacent disk rims. However, previous proteomics studies showed that PDE6 has a concentration of ~500 molecules/μm^2 (Pugh et al., 2000) while the analysis here identified 920 molecules/μm^2 (Figure 20 E). The difference could be caused by the error-prone segmentation in the crowded environment of ROS. It is not unlikely that a substantial number of connectors are false positives. The interpretation of the presented connector segmentation proved limited. Therefore, further experiments were conducted to test the hypothesis and to elucidate the quality of the connector segmentation.

3.4.3 The connector segmentation in ROS of *rd1/+* mice could not confirm PDE6 as disk interior connector.

A potential model system to test the hypothesis of PDE6 as disk interior connector are heterozygous *rd1/+* mice. Mice homozygous for the *rd1* mutation suffer from early onset photoreceptor and retinal degeneration caused by a mutation of the *PDE6b* gene (Chang et al., 2002). However, heterozygous *rd1/+* show no sign of photoreceptor degeneration (Farber et al., 1994). Western blots against PDE6 prepared in the Palczewski lab (UCI, California, USA) indicated that the expression level of PDE6 is significantly lower in *rd1/+* mice compared to the WT. If the hypothesis of PDE6 as disk interior connector and the results of the western blot are correct, the density of disk interior connectors is expected to be lower in ROS of *rd1/+* compared to the WT while the density of the disk rim species remains unaffected.

A new strain of *rd1/+* mice was prepared by the animal facility at the Max Planck Institute of Biochemistry. First objective was to reproduce the Western blots against PDE6 and to confirm the result with mass spectrometry. Retinas were extracted from WT and *rd1/+* mice and lysed. A fraction of the lysates was used for western blotting. The proteins contained in the lysates were separated by SDS-PAGE (Figure 22 A) and transferred from the gel onto a PVDF membrane (Figure 22 B). The membrane was blocked with skim milk and incubated with antibodies against the β-subunit of PDE6 (PDE6β) and β-Actin as loading control. Western blots were developed with the alkaline phostphatase reaction, digitized by scanning (Figure 22 C) and the grey values of the protein bands integrated. The ratio of PDE6β divided by the β-Actin intensity is a measure for the expression level of PDE6. The remaining lysate was analyzed by mass spectrometry. The retina lysates were prepared in three conditions:

1. in RIPA buffer which is not compatible with mass spectrometry,
2. in mass spectrometry compatible buffer,
3. in mass spectrometry compatible buffer with probe sonication.

Only RIPA buffer solubilized retinas completely. With the mass spectrometry compatible buffer, a large pellet remained after lysis while additional ultrasonication fully solubilized the retinal pellet. However, after sonication, the stained SDS-gels after protein transfer revealed that a large protein fraction did not enter the gel lanes and were not transferred onto the PVDF membrane (Figure 22 D). This indicates incomplete solubilization of retinal protein contents. The difference in the expression level of PDE6 detected in western blots of mass spectrometry compatible lysates was not significant with respect to the 5% significance level (Figure 22 E). Label-free quantification of the protein contents in the lysates by mass spectrometry (MS) (Cox et al., 2014) provided similar ambiguous results. MS detected similar amounts of rhodopsin WT and *rd1/+* mice which was expected. Slightly lower amounts were observed for all three subunits of PDE6 in *rd1/+* mice. However, given the variance of the MS measurements, the differences for PDE6β were not significant while the differences for the PDE6 α- and γ-subunit were at the border line just above the 5% significance level (Figure 22 F). Only the Western blots obtained with

RIPA buffer lysates indicated significantly lower expression of PDE6 in *rd1/+* mice. Overall, the results derived from different lysates were contradictory. However, the RIPA buffer performed best in terms of lysis as the entire retina was solubilized and the protein transfer onto the PVDF membrane was complete. Therefore, it was assumed that the results with RIPA buffer are most reliable and that PDE6 indeed has a lower expression level in *rd1/+* mice compared to the WT. This experiment illustrates a major problem of western blotting and MS for proteomics experiments. Both methods are highly sensitive for protein detection and can yield quantitative results. But they are dependent on comparable and reproducible solubility of proteins in the sample.

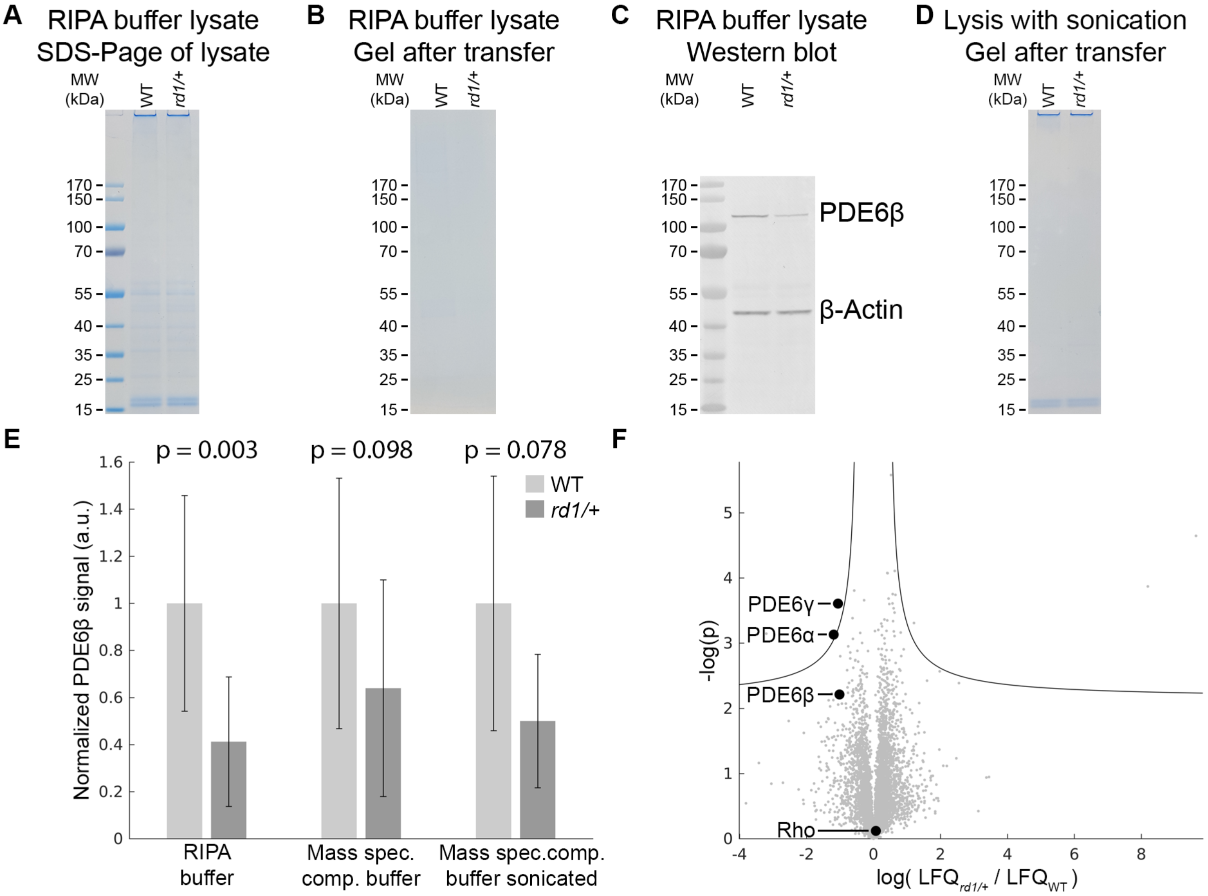

Figure 22: Western blots against PDE6 and results of mass spectrometry.
A-C) Western blots against PDE6β of retina lysates in RIPA buffer. Stained gel with lysates after SDS-PAGE in A, stained gel after protein transfer onto PVDF membrane in B, Western blot against PDE6β and β-Actin after development with alkaline phosphatase reaction in C. **D)** Gel loaded with retina lysate in mass spec compatible buffer with sonication after protein transfer onto the PVDF membrane. The strong stain in the loading pocket indicates incomplete protein transfer. **E)** Western blot analysis of PDE6 expression. The p-Values are calculated according to the two sample Kolmogorov-Smirnov test. **F)** Volcano plots derived from mass spectrometry data obtained from lysis with probe sonication. LFQ means label-free quantification. Differences in the detected amount of the PDE6 subunits are not or barely significant with respect to the 5% significance level. Here, differences are significant when the corresponding datapoints are above the black hyperbole.

After confirming the lower expression of PDE6 in *rd1/+* mice they were used to test the PDE6 hypothesis. ROS were extracted from *rd1/+* mice and prepared for cryo-ET as described before. Tomographic data was acquired with VPP in focus (*rd1/+*$_{\text{VPP-inf}}$). The ROS disk stack in *rd1/+* mice appeared identical to the WT (Figure 23 A). Connectors were segmentated and analyzed in 5 tomograms. The connector properties derived from the segmentation (Figure 23 B) and total numbers of picked connectors were comparable in WT and *rd1/+*. If PDE6 has lower expression levels in ROS of *rd1/+* mice and if PDE6 forms a connector between adjacent disks, it was expected that less connectors are picked in the disk interior. However, the density of disk interior connectors showed no significant difference between WT and *rd1/+* (Figure 23 C).

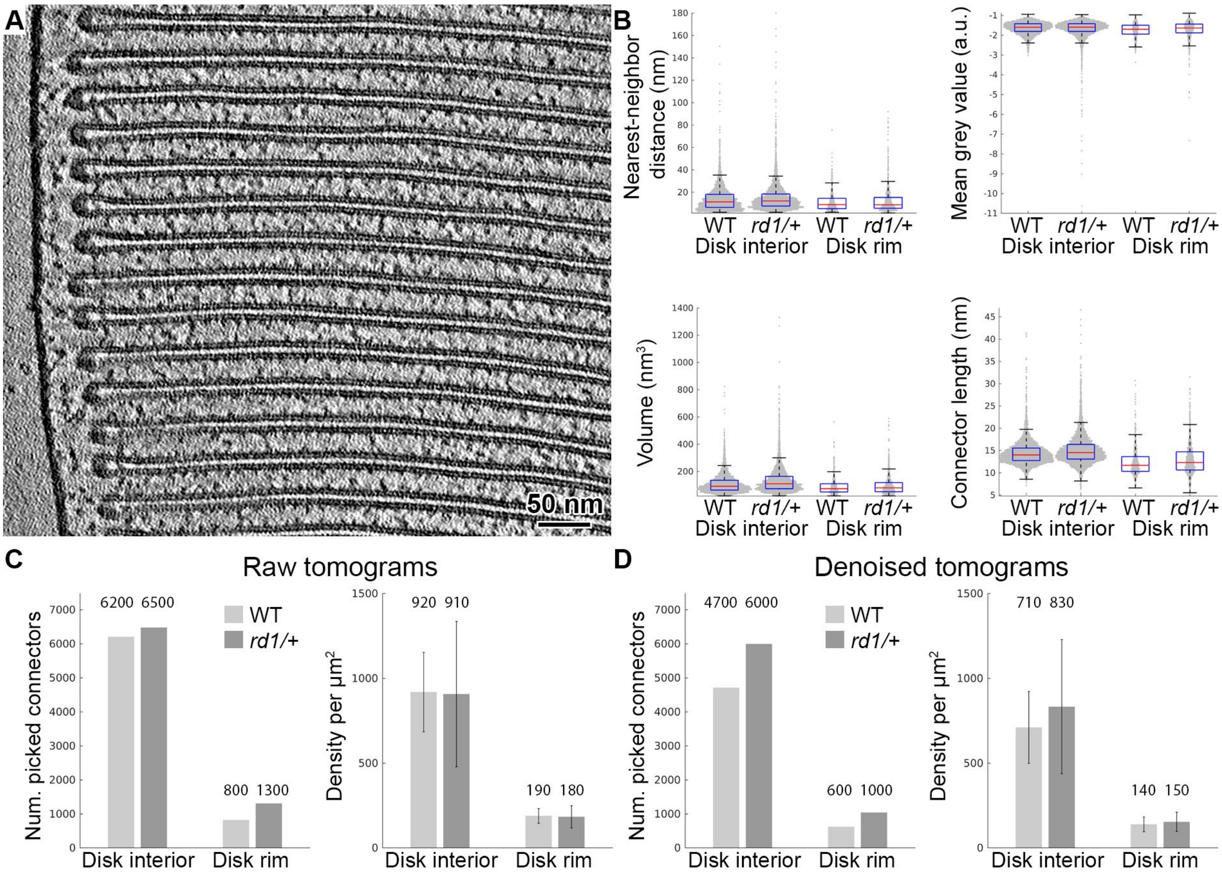

Figure 23: Connector segmentation in *rd1/+* mice.
A) Tomographic slice of ROS from *rd1/+* mouse. **B)** Box plot of connector properties segmented in WT and *rd1/+* mice. The connector properties are similar in both genotypes. **C)** and **D)** connectors densities in WT and *rd1/+* mice extracted from raw and denoised tomograms, respectively. In both cases, there is no significant difference in the density of disk interior connectors between WT and *rd1/+*.

This result allows three possible conclusions:

1. The hypothesis is wrong and PDE6 is not forming connectors between adjacent disks.
2. The chosen segmentation approach is too error prone to test the hypothesis.

The segmentation of densities in tomograms is error prone. The combination of the high noise levels, the crowded molecular landscape of ROS and the close proximity of neighboring disks increases the probability to pick false positives. For example, the segmentation algorithm cannot distinguish between two membrane-attached, densities protruding into the cytosol from opposite sides of adjacent disks and occasionally contacting each other from an actual connector. The noise levels can be reduced with denoising algorithms like Cryo-CARE (Buchholz et al., 2019). Denoising improves the quality of tomograms tremendously (Figure 15) and it is easier to distinguish continuous from two separate densities by visual inspection. Hence, the segmentation was repeated on denoised tomograms. The tendency to pick less false positives is reflected by the overall lower number of segmented connectors. But the results still suggest similar connector densities in ROS of *rd1/+* and WT mice (Figure 23 D).

The connector segmentation alone failed to confirm the PDE6 hypothesis. It is hard to say whether the initial hypothesis is wrong or the segmentation approach not suitable. However, the structure of PDE6 is known and the segmentation identified positions of putative PDE6 positions in the tomograms. Therefore, other image processing tools were employed aiming to elucidate the quality of the segmentation and to obtain direct confirmation of PDE6 as disk interior connector.

3.4.4 Subvolume averaging of disk interior connectors unveils the imperfection of the segmentation but supports that disk interior connectors exist.

Recently, methods have been established for the reference-free detection and classification of membrane-attached densities (Martinez-Sanchez et al., 2020). Maximum-likelihood algorithms proved to be suitable tools for subvolume alignment and classification of heterogeneous cryo-EM dataset (Scheres, 2016). Here, a hybrid approach was chosen to sort the structural heterogeneity of the picked connectors by classification and to distinguish true connectors from false positives. The more homogeneous classes where then aligned to obtain a subvolume average which could be compared with the high-resolution density map of PDE6 (Gulati et al., 2019) to confirm the identity of the connectors.

First, the $\mathrm{WT}_{\mathrm{VPP\text{-}inf}}$ dataset was analyzed. Subvolumes extraction points were defined at the contact points of the segmented connectors with the two disk membranes which resulted in two extraction points per connector. Two of the three Euler angles were determined by aligning disk membrane of all subvolumes with respect to each other and by orienting the subvolume z-axis parallel to the normal vector of the membrane. The angle of the in-plane rotation was randomized. Averages using this initial orientation displayed a density protruding into the cytosol (Figure 24 A). However, the signal of the cytosolic density was rather weak which indicates heterogeneity of the protein signals contributing to the average.

Simple alignment and classification of all initially extracted 3D subvolumes in Relion was unsuccessful. The obtained class averages remained featureless densities protruding from the disk membrane into the cytosol. Subvolume alignment of ROS densities is challenging for several reason.

1. The targeted proteins are small. Currently, complexes below 500 kDa are considered small for subvolume averaging (Turk et al., 2020). PDE6 is the biggest expected cytosolic protein in ROS with a molecular weight of 215 kDa, while most of the other proteins are smaller than 100 kDa.
2. The angle of the in-plane rotation and orientation along the ROS axis of putative connectors are not known *a priori*.
3. The strong membrane signals complicate the alignment.
4. ROS have a crowded molecular landscape.
5. The connector densities are heterogeneous and contain false positives.
6. The proteins forming a connector are probably flexible.

7. Data was acquired with VPP which is suboptimal for high resolution subvolume averaging and processing with currently available software packages (Turoňová et al., 2020).

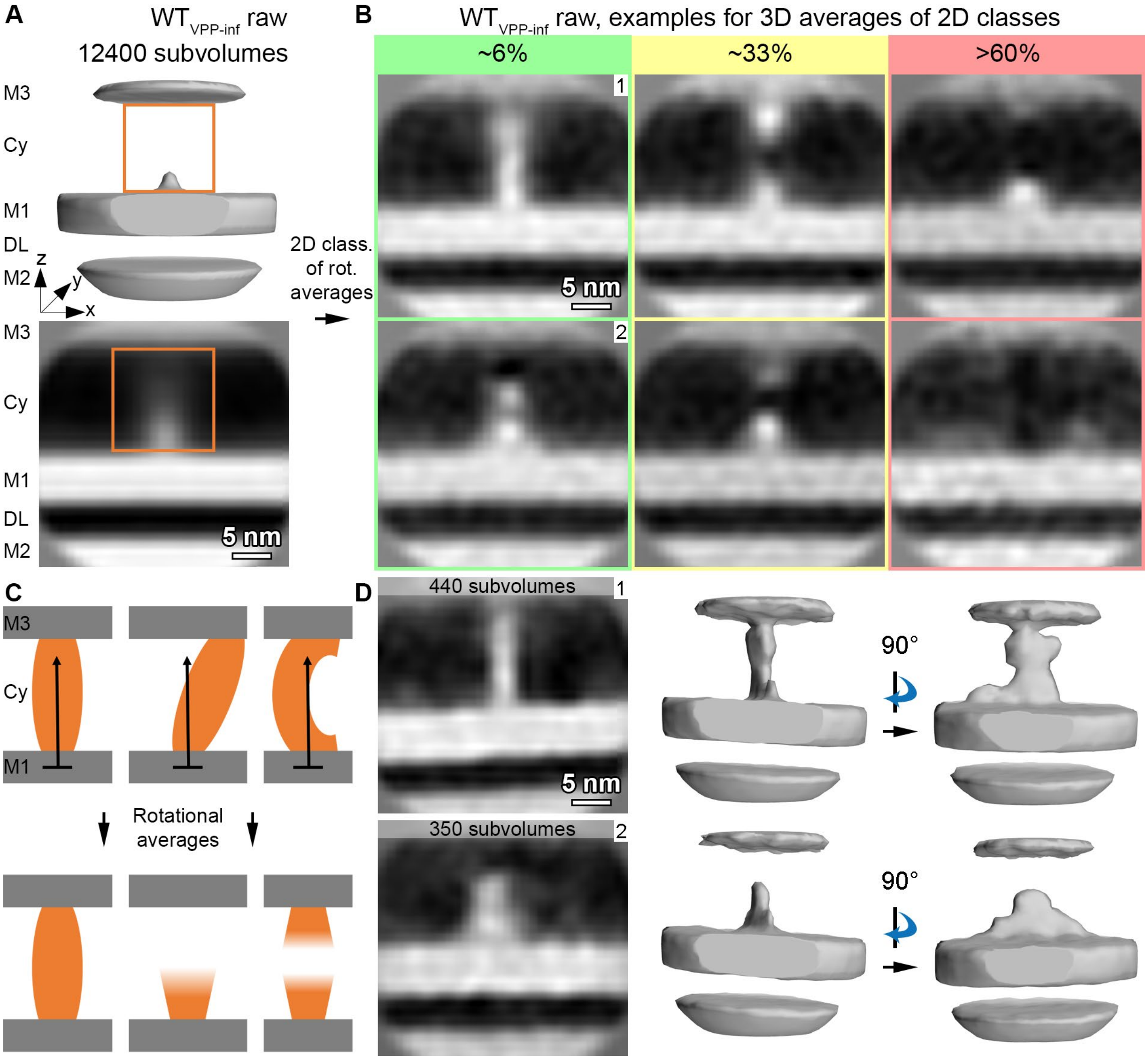

Figure 24 Averaging and classification of the WT$_{\text{VPP-inf}}$ disk interior connectors.
A) Initial average of all WT$_{\text{VPP-inf}}$ disk interior connector as isosurface representation and xz-slice through the center of the average in the top and bottom panel, respectively. M1 indicates the membrane at which the subvolume was extracted, M2 the second membrane within the same disk, M3 the neighboring disk, Cy the cytosol and DL the disk lumen. The orange box marks the outline of the mask used for classification. **B)** Examples for 3D class averages obtained by 2D classification of rotational averages as implemented in (Martinez-Sanchez et al., 2020). Promising classes which appear as straight connectors are boxed in green, ambiguous classes in yellow and false positives in red. **C)** Sketch of connectors and the corresponding 2D rotational averages. Only a straight connector is immediately observed as connector in the class averages. An inclined connector will be resolved as density attached to one membrane. **D)** Alignment of subvolumes in most promising 2D classes. The resulting averages remain featureless blobs.

The first four points are problems concerning the alignment method. Proper masking can minimize the influence of membranes and neighboring densities on the alignment of the target density. The angular search can be tuned to exhaustively sample the in-plane rotation while the search for the other two Euler angles is constrained. The main limiting factors are points five and six. The protein signal must have components above the noise level to drive the alignment (Rosenthal et al., 2003). This depends on the size of the protein and the quality of the data. Particularly VPP tomograms show an unprecedented level of detail and exhibit strong signals at low spatial frequencies. However, heterogeneity and false positives impair the alignment. This is the reason for the unsuccessful alignment of all initially picked connectors. To address the heterogeneity of biological molecules in cryo-EM, classification approaches have been developed. Relion is a powerful tool as it can treat the class assignment as a hidden variable without the *a Priori* knowledge about references (Scheres, 2016), but classification in Relion did not improve the results. Presumably, the algorithm was not able to sort heterogeneity of the data based on 3D subvolumes. Therefore, another approach was chosen. For each subvolume, a rotational average around the membrane normal vector was calculated with a cylindrical mask centered around the cytosolic density which cut out the signal of the membranes (Figure 24 A). The resulting 2D images were classified using a reference-free machine learning algorithm (Martinez-Sanchez et al., 2020). Examples of the obtained classes are depicted in Figure 24 B and can be used to evaluate the quality of the connector segmentation. Only 6% of the initial subvolumes were assigned to classes which could be identified as straight connectors. 39% of the subvolumes contribute to classes that resemble membrane-attached densities protruding from either one or both sides into the cytosol, but without direct contact to the neighboring disk. These classes are ambiguous, as the rotational averaging of inclined densities will result in averages without direct contact between neighboring membranes (Figure 24 C). The visual inspection of tomograms showed that many connectors appear inclined. This type of 2D classification suffers from the same problem as the connector segmentation: In the crowded environment of ROS, it is impossible to distinguish an actual connector from two separate densities bumping into each other from opposite disk membranes. However, more than 60% of the initial subvolumes were identified as false positives, because the class average showed only a small membrane-attached density or no density at all. This suggests that the results of the connector segmentation are erroneous and the calculated connector densities overestimated. The subvolumes in the most promising classes were aligned in Relion (Figure 24 D). The resulting averages did not have enough features to allow interpretation or comparison to the density map of PDE6.

There are three possible factors limiting the results of subvolume averaging: (i) the data acquisition scheme, (ii) the heterogeneity of the data and (ii) the small number of subvolumes, as the promising classes contained only a few hundred subvolumes. A known problem for subvolume averaging of VPP data is the improper spatial frequency weighting which causes density maps to appear less detailed than the FSC suggests (Turoňová et al., 2020). To avoid this, connector subvolumes were picked and extracted in conventional tomograms of the WT_{conf} dataset which were denoised with Cryo-Care. The 2D classification of rotational averages revealed again three categories of classes: clear connectors with 20%, ambiguous species with 55% and false positives with 45% of all subvolumes (Figure 25 A). The promising classes were extracted from non-denoised tomograms, preprocessed in Warp and aligned in Relion. However, the resulting averages were again of low quality indicating that the limiting factor was not the acquisition scheme.

The connector segmentation was repeated with denoised VPP tomograms and connectors subjected to classification (Figure 25 B). The results are similar to the denoised WT_{conf} dataset. 20% of the subvolumes were in classes that appeared as straight connectors which is much higher than in tomograms without denoising (6%, Figure 24 A). This suggests that the disk interior connectors indeed exist and are not an artifact caused by the segmentation in noisy tomograms of crowded ROS. Furthermore, the number of false positives is reduced from above 60% to less than 50%, implying that denoising is beneficial for the segmentation. However, all attempts to gain further structural information about the putative disk interior connectors failed. Most likely due to the heterogeneity, the small size of the proteins and the limited number of subvolumes. Perhaps, a larger dataset and an acquisition at higher magnification would be beneficial. More subvolumes and a finer sampling of the features would assist the classification and the subsequent alignment. Still, subvolume averaging of the cytosolic densities in ROS is a computational problem at the edge of what is possible with currently available software - or even beyond it.

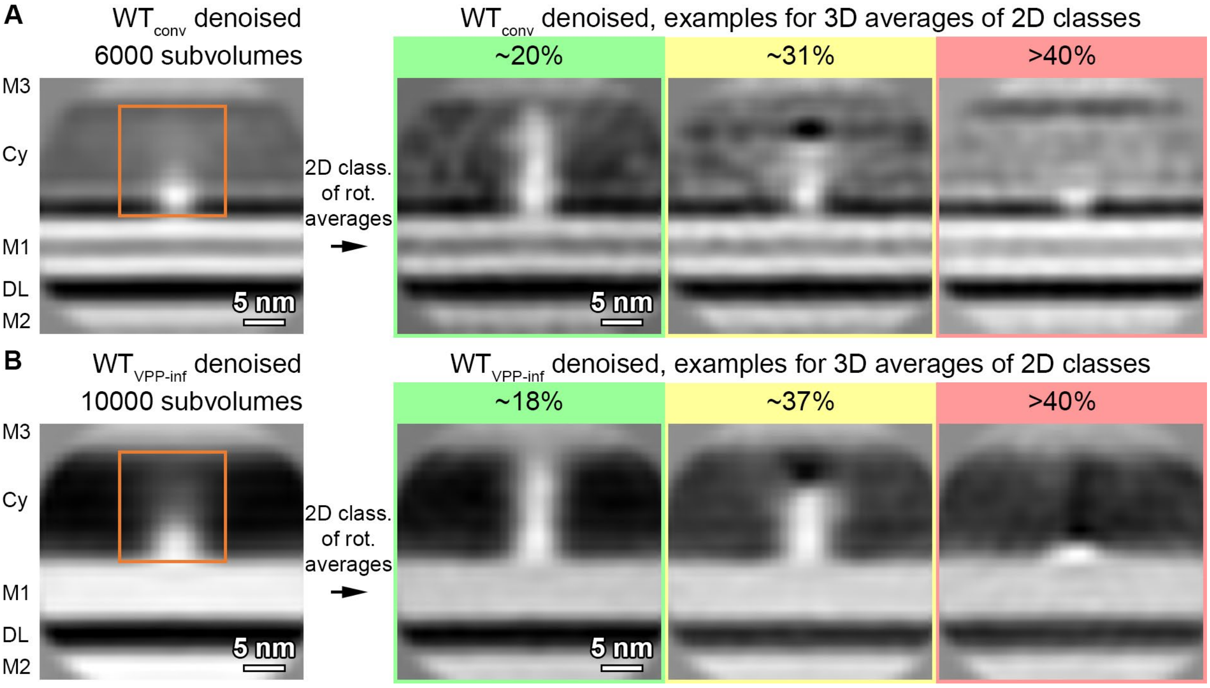

Figure 25: Classification of disk interior connectors in denoised tomograms.
A) and **B)** cross-sections through initial average and exemplary class averages of connectors segmented and extracted from the denoised WT_{conv} and denoised $WT_{VPP\text{-}inf}$ dataset, respectively. The number of subvolumes in classes that appear as false positives is lower while the number in classes of clear, straight connectors is higher compared to the segmentation in raw, non-denoised tomograms. The orange box in the left panels marks the outline of the mask used for classification. Color code: promising, ambiguous and false positive class averages are boxed in green, yellow and red, respectively.

As a final attempt to check the PDE6 hypothesis, disk interior connectors segmented in *rd1/+*$_{VPP\text{-}inf}$ were subjected to the same workflow of alignment (Figure 26 A) and classification of rotational averages (Figure 26 B) as conducted for $WT_{VPP\text{-}inf}$. If the identified true connectors are formed by PDE6 and if PDE6 has a lower abundance in ROS of *rd1/+* mice, it would be expected to find a smaller fraction of subvolumes in classes of that appear as connectors. This is again not the case (Figure 26 B). With 7% and 35% of the initial subvolumes assigned to the straight connector or ambiguous classes, respectively, the populations in *rd1/+* are comparable the WT (6% and 39%). Overall, the segmentation and the classification of connector subvolumes found no significant differences between ROS of WT and *rd1/+* mice. The results suggest that a connector in the disk interior exists. However, due to the error prone segmentation the quantification of its abundance is ambiguous and the and its identity could not be elucidated.

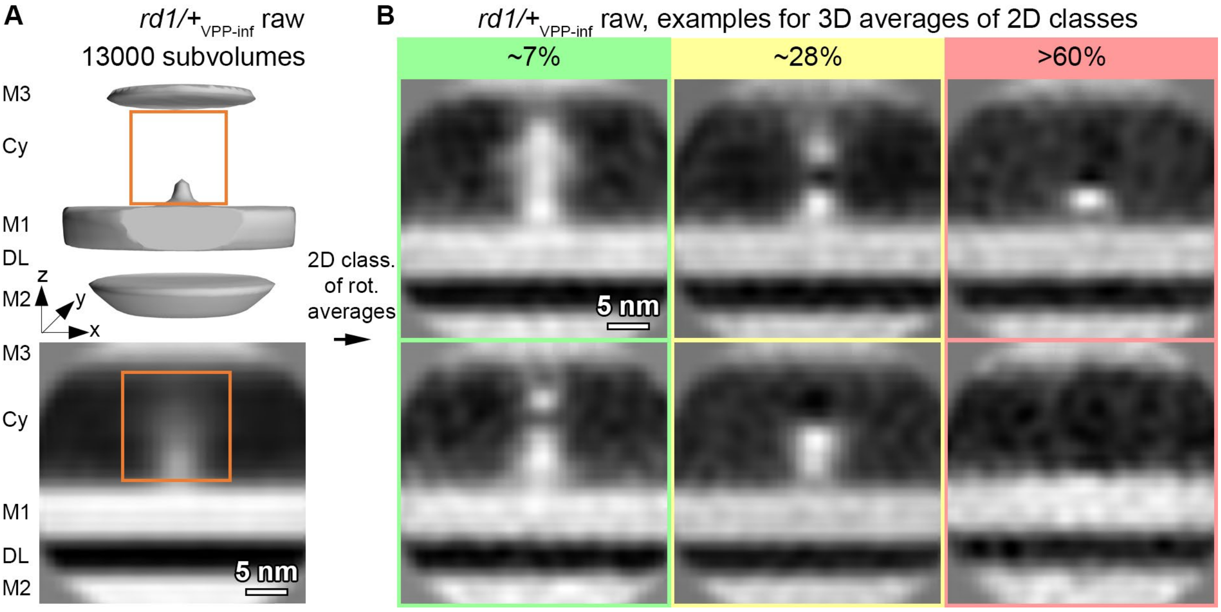

Figure 26: Classification of disk interior connectors in *rd1/+* mice.
A) Initial average of all disk interior connector subvolumes from *rd1/+*$_{\text{VPP-inf}}$ as isosurface and xz-slice through the center of the average in the top and bottom panel, respectively. The orange box marks the outline of the mask used for classification. **B)** Examples for 3D averages of classes obtained by 2D classification of rotational averages as implemented in (Martinez-Sanchez et al., 2020). Color code: promising, ambiguous and false positive classes are boxed in green, yellow and red, respectively.

3.4.5 Subvolume averaging of disk rim connectors indicates that their position at the rim is more variable than previously proposed.

A similar pipeline for subvolume analysis as used for the disk interior connectors was applied to the disk rim connectors. Extraction points were defined at membrane contact points but in contrast to the interior connectors, the angle of the in-plane rotation could be determined by aligning the subvolumes with respect to the disk rim. The resulting average shows a membrane-attached density in proximity to the disk rim (Figure 27 A) which becomes weaker further into the cytosol. This indicates the flexibility of the molecular connector and fluctuations of distances between adjacent rims. Additionally, the high membrane curvature of the hairpin-like disk rim is only partially resolved which suggest a distribution of how far in the disk interior the connector contacts the membrane. This distribution is roughly centered 16 nm away from the outer disk periphery. However, this is contradictory to the previously described terminal loop complex, organized in a lattice and composed of connectors in proximity to the rim, which are anchored by a transmembrane component to a density at the rim inside the disk lumen (Corless et al., 1987). The *in-situ* data presented here suggest more heterogeneity, as the connectors distance towards the outer periphery of disks (Figure 27 A) and the distances between neighboring rim connectors (Figure 20 B) vary considerably.

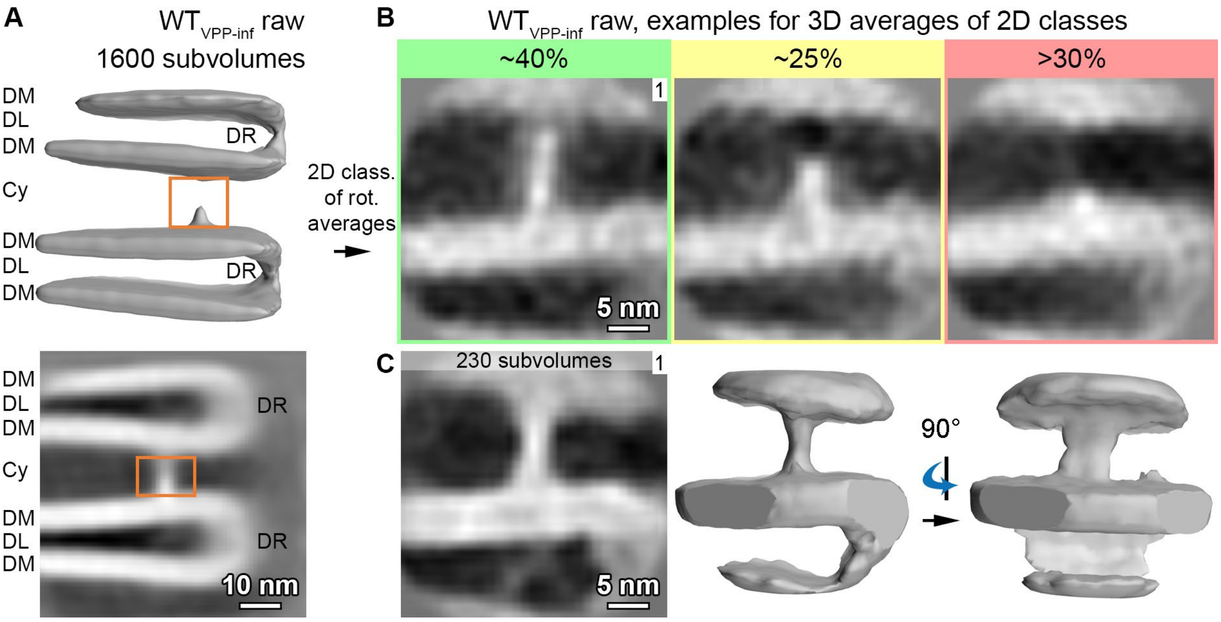

Figure 27: Alignment and classification of disk rim connectors in WT mice.
A) Initial alignment of all disk rim connectors. The isosurface represetation of the average is shown in the upper panel, the cross-section through the center in the lower panel. DM denotes disk membranes, DL the disk lumen, Cy the cytosol and DR the disk rim. The orange box marks the outline of the mask used for classification. **B)** 3D averages of 2D classes. A promising class which appears as straight connector is boxed in green, an ambiguous class in yellow and a false positives class in red. **C)** Subvolume alignment of the promising classes. The left panel shows a cross section through the center of the average, middle and right panel isosurface representations from two orientations. They display a clear connector between neighboring disk rims, but no further structural information can be inferred.

The 2D classification of rotational averages indicated a substantial number of false positives. But with 35% this contribution is smaller than for the disk interior connectors (61%), while 40% of the rim connector subvolumes were assigned to classes with averages that appear as straight connectors (Figure 27 B). Therefore, the segmentation of the disk rim connectors is still error prone but more reliable than for the interior connectors. The most promising classes were further subjected to subvolume alignment. The final average displays a straight connector between adjacent disk rims. However, no further structural information can be inferred from it. This is most likely due to the small number of 230 subvolumes contributing to the average. Furthermore, the molecules forming the disk rim connector must be flexible to adjust to varying distances between adjacent rims. Here it was suggested that GARP2 proteins form the connector in an oligomeric state. About 80% of the GARP2 sequence is predicted to be disordered (Batra-Safferling et al., 2006). In that case, subvolume averaging would not be suitable to recover high resolution information about the structure of the rim connector. However, the average also does not indicate a structured membrane contact or ordered transmembrane domain which links the connector to a crescent density at the perimeter of the rim in the lumen as proposed previously (Corless et al., 1987). But a better average would be required to ultimately proof this.

3.5 Elongated, membrane-attached densities are found at the plasma membrane and disk rims but could not be unambiguously assigned to continuous connectors.

The widely accepted but incomplete model for the organization of the ROS disk stack involves the existence of spacer between the plasma membrane (PM) and the disk rims. These connectors were observed in freeze fracture and metal shadowing experiments (Roof et al., 1982), in metal stained, plastic embedded EM micrographs (Townes-Anderson et al., 1988) and in cryo-ET data (Nickell et al., 2007). Later it was proposed that the GARP-part of the cyclic nucleotide gated cation channel (CNG-channel) forms these connectors (Poetsch et al., 2001).The proteins used in those experiments were purified from mammalians. In this work it is shown that the distance between disk rim to and PM is 25 nm in mice. However, the model (Batra-Safferling et al., 2006) assumes a distance of 10 nm between rim PM which is only true for in amphibians (Roof et al., 1982). Therefore, the model is based on wrong assumptions. Additionally, obvious connectors were not observed in ROS tomograms here which motivated an in-depth search for densities between PM and disk rims. The high contrast of VPP tomograms acquired in focus ($WT_{VPP\text{-}inf}$) was beneficial for particle picking but the inability to correct for the CTF prevented the use of state-of-the-art preprocessing software. Therefore, for the PM connectors a VPP dataset acquired with a defocus of 3 µm and thus compatible with WARP was analyzed ($WT_{VPP\text{-}def}$).

Two methods were employed to search for connectors. First, membranes of disk rims and PM were segmented and the Pyto software utilized to pick densities linking the two membrane boundaries together. Subsequently, subvolumes were extracted at the contact points of the connectors with the PM. The initial average comprised a small membrane-associated density (Figure 28 A). Classification of rotational averages with a mask focusing on the cytosol revealed three types of classes: Around 34% of all segmented connectors were false positives, 48% were assigned to ambiguous classes and 18% indicated a large, straight membraneattached density protruding more than 10 nm into the cytosol (Figure 28 A).

For the second method, splines along the outer periphery of disk rims were manually selected. Subvolumes were extracted every 5 Å along the spline and aligned. The initial average of the aligned subvolumes resampled the shape of the disk rim with no further features in the cytosol (Figure 28 B). The classification of rotational averages focused on that area gave similar results as for subvolumes picked at the PM. One fraction was identified as false positives, some classes were ambiguous and a small fraction had a large, straight density attached to the disk rim (Figure 28 B). The ratio of subvolumes assigned to classes without density is with 88% much higher than for subvolumes extracted at the PM. This is caused by the oversampling along the spline of disk rims which includes many random positions while the Pyto software picked more selectively densities between PM and rim. However, 4% of the subvolumes contribute to classes with rim-attached densities spanning more than 10 nm into the cytosol. Therefore, large membrane-attached densities could be found at the disk rim and the PM and the number of subvolumes in these most promising classes was similar.

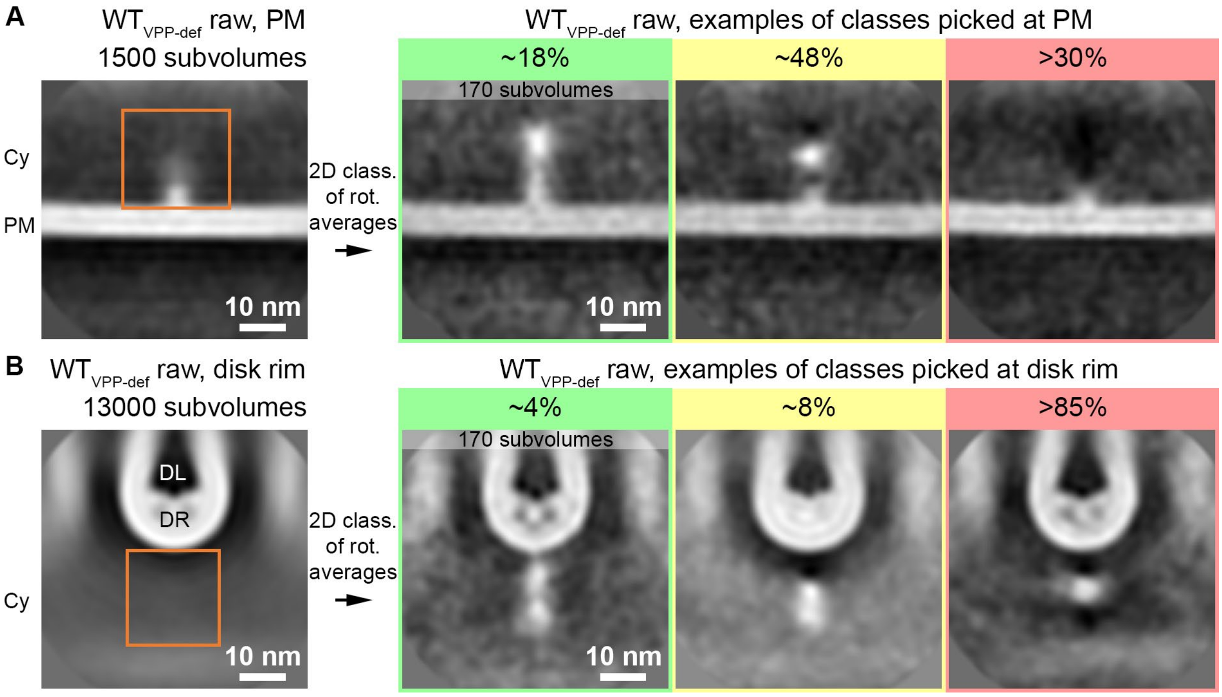

Figure 28: Classification of connectors between the disk rim and the plasma membrane.
A) and **B)** Averaging and classification of connectors picked by segmentation at the disk rim and densities picked at the outer periphery of the disk rim, respectively. The left panel shows the initial average. The right panel 3D averages of 2D classes. Some classes indicate large densities protruding several nanometers into the cytosol. The orange box in the left panels marks the outline of the mask used for classification. Cy denotes the cytosol, PM the plasma membrane, DR the disk rim and DL the disk lumen. Color code: promising, ambiguous and false positive class averages are boxed in green, yellow and red, respectively.

If the picked densities were the CNG- channel, the low number of 170 subvolumes would be expected due to the low abundance of CNG channels. With only 500 molecules/µm² of PM (Pugh et al., 2000), only 20 to 50 CNG channels were estimated to be found in the field of view per tomogram. Caused by this low number of subvolumes, classification and alignment in Relion was not able to recover more structural features. This raised the question whether the elongated structures separately picked at rim or PM belonged to the same protein complex. In that case, the coordinates would be colocalized. Therefore, the positions of the subvolumes were pasted back into the original tomograms. An overview image revealed that the positions were overall not localized in close proximity (Figure 29 A). Closer inspection by eye identified three distinct cases:

1. In rare cases, densities were picked on opposite sides at the rim and at the PM while the tomogram indicated a straight density in between both positions (Figure 29 B).
2. Often a large density was observed in tomograms between rim and PM but it was not picked by either method. Figure 29 C shows an example. This particular density was not picked at the rim because it is attached to the side of the rim and not its front-most part. Pyto did not segment the density because it is not continuous between both membranes within the threshold ramp used for segmentation. However, whether it is a false negative or a random cytosolic density cannot be determined.
3. Figure 29 D depicts two positions: one at the rim and one at the PM. They are in close proximity but belong to two independent, not connected densities.

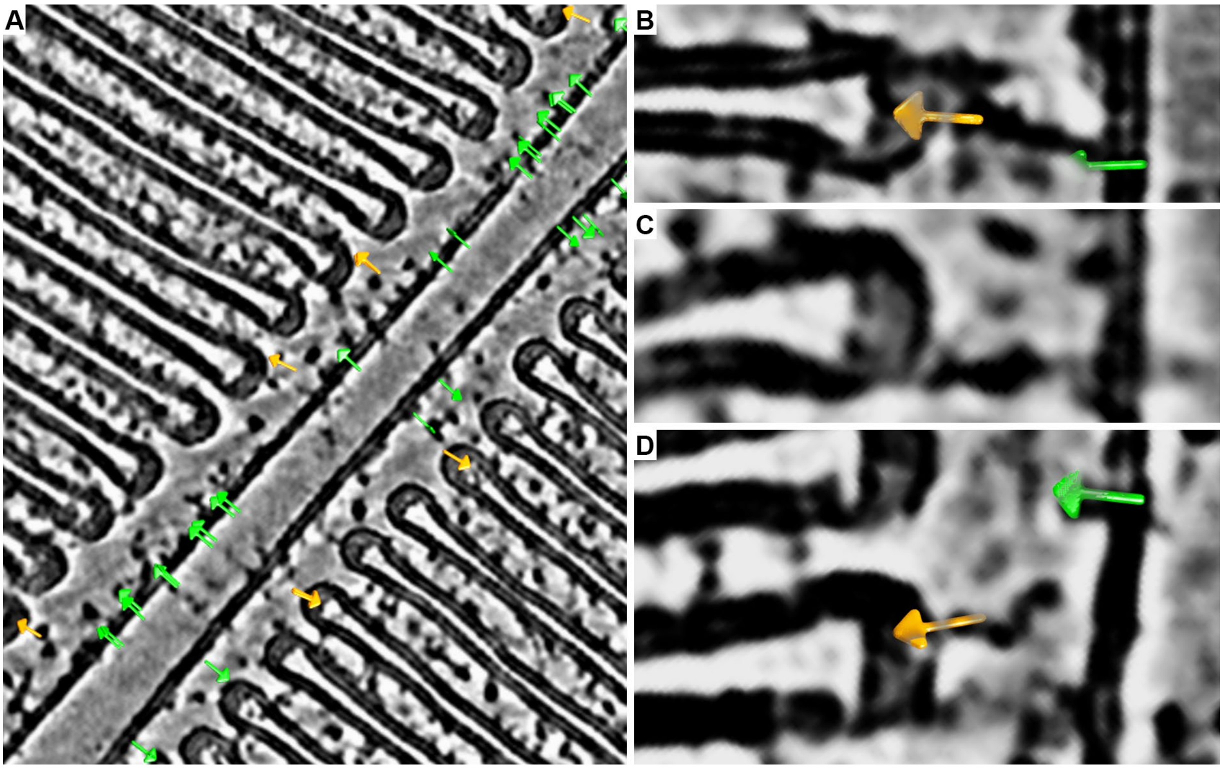

Figure 29: Coordinates of densities picked at rim or PM mapped back into a tomogram.
A) Overview image showing a slice of a denoised $WT_{VPP-def}$ tomogram. The green and orange arrows represent the positions of large densities picked at the PM and the disk rim, respectively, in 3D. Hence, the position of an arrow does not necessarily overlap with a density in the shown tomographic slice. Overall, the localization of both is not correlated. **B)** Rare example of clear, straight connector between PM and disk rim that was picked by both methods. **C)** A strong density seemingly attached to the disk rim which was not picked at disk rim or PM. **D)** Two densities in close proximity, one at the disk rim, one at the PM but they are not connected to each other. The density at the rim is protruding far into the cytosol but appears different from the density in B.

All three cases together illustrate the heterogeneity of the data which complicates the analysis. As the segmentation was able to pick densities between PM and disk rim, it seems likely that connectors exist as the previous model suggests. However, picking these connectors was ambiguous and subsequent averaging and sorting of the small number of subvolumes into the large membrane-attached and random cytosolic densities was impaired.

To exclude negative effects of the VPP data acquisition and the low subvolume numbers on subvolume alignment, a large conventional dataset WT_{conv} was analyzed. 550000 subvolumes were picked along splines of disk rims and 2D images of their rotational averages were classified. Similar to $WT_{VPP-def}$, class averages containing 2% of the subvolumes appeared to have an elongated structure attached to the disk rim (Figure 30 A). This comprised several thousand subvolumes but their alignment again did not produce useful averages, as the signal of the cytosolic density became weaker throughout the alignment iterations (Figure 30 B).

Additionally, the subvolume positions were shifted to the adjacent PM where new subvolumes were extracted. After their membrane signal was brought into register, 2D classification of rotational averages was used to identify densities at the plasm membrane. The 9700 subvolumes from the most promising classes were combined. Their average indicated a density protruding more than 15 nm into the cytosol, which was completely lost during alignment in Relion (Figure 30 C). Likely the signal of the cytosolic density was not strong enough or too heterogeneous to drive subvolume alignment.

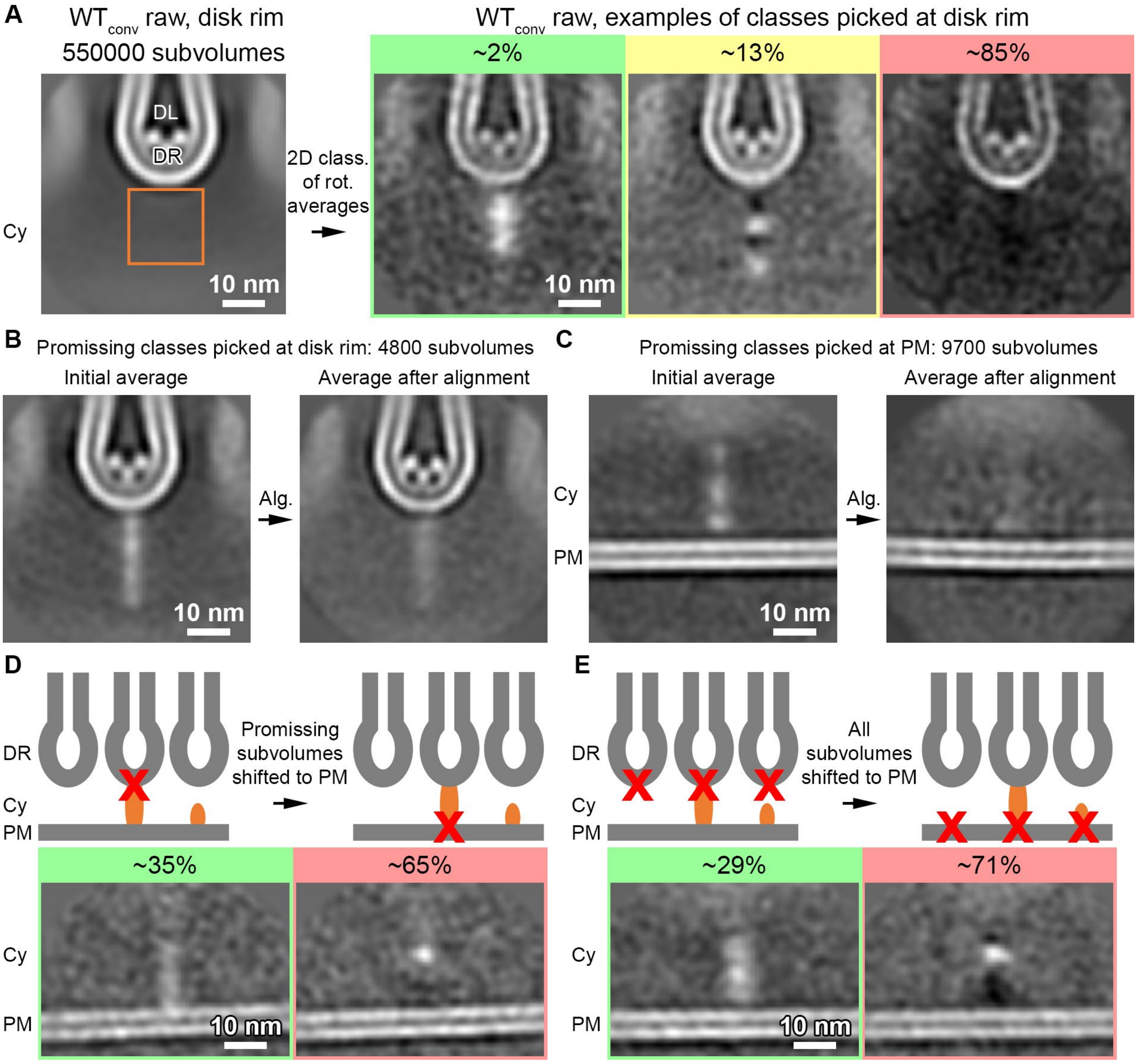

Figure 30: Classification of densities between PM and disk rim in conventional tomograms.
A) Averaging and classification of densities picked at the outer periphery of the disk rim. The left panel shows the initial average. The orange box marks the outline of the mask used for classification. The right panel shows 3D averages of 2D classes. Some classes indicate large densities protruding several nanometers into the cytosol. **B)** and **C)** illustrate the alignment of promising classes at disk rim and at the PM, respectively. **D)** and **E)** Comparison of the probability to pick up an elongated, membrane-attached density at the PM opposite of the disk rim. In D when a large density was already detected at the rim or in E for all initial disk rim positions. Cy denotes the cytosol, PM the plasma membrane, DR the disk rim and DL the disk lumen. Color code: promising, ambiguous and false positive class averages are boxed in green, yellow and red, respectively.

Furthermore, it was checked how likely is it to find a density at the PM when the rim on the opposite side had density attached to it. This was the case in 35% of the most promising subvolumes (Figure 30 D) and was slightly higher compared to the 29% probability to pick a density attached to the PM opposite of a random position at the disk rim (Figure 30 E). This can be another indication for the existence of molecular connector between the rims and PM. However, only in 15% of all subvolumes no density was detected between rim and PM. This raised the question whether the 2D classification can distinguish a random cytosolic density from a membrane-attached density in the crowded environment of ROS.

So far, a main limiting factor for subvolume averaging in this work was the small size of the proteins. In the case of the putative connector between PM and disk rim which was proposed to be the cyclic nucleotide gated cation channel (CNGC), it is different. The CNGC with more than 600 kDa is the largest protein complex residing in ROS (Pugh et al., 2000). Large densities were picked at the PM and at disk rim, but subvolume averaging did not yield interpretable results. The problem is the heterogeneity and the flexibility of the picked densities which is illustrated in Figure 29 B and D. It is possible that CNGCs form a connector, but that its intrinsically disordered GARP-part (Batra-Safferling et al., 2006) was not resolved in tomograms as straight connector. Additionally, the presented segmentation and classification approaches cannot distinguish a random cytosolic density from a true connector in the crowded molecular landscape of ROS. This makes a reliable analysis of connectors and the alignment of subvolumes virtually impossible.

3.6 Subvolume analysis of cytosolic, disk membrane-attached densities provided uninterpretable results.

Until here, subvolume analysis focused on the connectors between ROS membranes. These structures must be flexible to adapt to fluctuations in the membrane distances which results in heterogeneity. In combination with the small number of subvolumes and the difficulty to identify a homogeneous species of true connectors, this makes it a particularly difficult task for subvolume averaging. However, the VPP tomograms reveal a wealth of other cytosolic densities which are most likely proteins involved in the signal cascade of phototransduction. The most abundant protein species in ROS were previously identified (Table 1). For many of the proteins involved in phototransduction, high resolution structural information was obtained (Gao et al., 2019; Gulati et al., 2019; Kang et al., 2015; Singh et al., 2008) indicating that these proteins assume stable folds and are potentially less flexible than the connectors discussed in the previous chapter. Furthermore, the majority of them are membrane associated or transmembrane proteins (Table 1). A suitable workflow to pick and classify subvolumes of membrane densities was already used here. Hence, it was tempting to search for the visual proteins in ROS tomograms.

First, a wild type dataset acquired with VPP and defocus ($\mathrm{WT}_{\mathrm{VPP\text{-}def}}$) was analyzed. Densities were picked within disk membranes, the corresponding coordinates projected onto the central membrane plane and distance cleaned. The resulting coordinates had a minimal distance of 3 nm between nearest neighbors and were used as subvolume extraction points. The subvolume z-axis was aligned perpendicular to the disk membrane while the in-plane rotation was randomized. Initially, 460000 subvolumes were extracted from 4x binned tomograms (pixel size = 10.48 Å). Without further alignment, the subvolume average exhibited a strong transmembrane density but the membrane bilayer was poorly resolved (Figure 31 A). This indicates that the extraction points were located at different heights across the membrane. Therefore, the subvolumes were aligned to the initial average as common reference while shifts were only allowed perpendicular to the membrane. This step aligned the membrane signal of the subvolumes with respect to each other. The membrane bilayers were clearly resolved in the resulting average, but the signal of the transmembrane density was lost (Figure 31 A) which allows two conclusions:

1. The initially picked densities are random noise fluctuations within the membrane with no common, underlying protein signal.
2. Most of the picked membrane densities correspond to Rhodopsin (Rho). It is by far the most abundant protein in ROS membranes and occupies the largest fraction the disk membrane area (Palczewski, 2006). Rho is a 36 kDa protein that is almost completely embedded in the membrane. The transmembrane density could be lost during the alignment because the Rho signal is weak compared to the membrane and could not drive subvolume alignment.

As an alternative approach, it was tried to identify subvolumes with additional cytosolic densities attached to the disk membrane. Direct classification of 3D subvolumes did not produce consistent or interpretable results. Therefore, rotational averages were calculated for each subvolume and the resulting 2D images classified (Martinez-Sanchez et al., 2020). The classification focused on the cytosol in proximity to the membrane. The 2D class averages indicated a variety of structures (Figure 31 B). Amongst them four groups were apparent: several classes that contained 10% of the subvolumes had a small density and 4% had a larger density both in direct contact with the membrane. Most of the other classes also indicated densities but with no link to the membrane. Only a minority of the classes had no density in proximity to the membrane. This illustrates the molecular crowding in ROS and the heterogeneity of the data. It further suggests the difficulty to distinguish membrane-attached densities from soluble, cytosolic densities. Most likely even after classification, subvolumes were not sorted into very homogeneous classes.

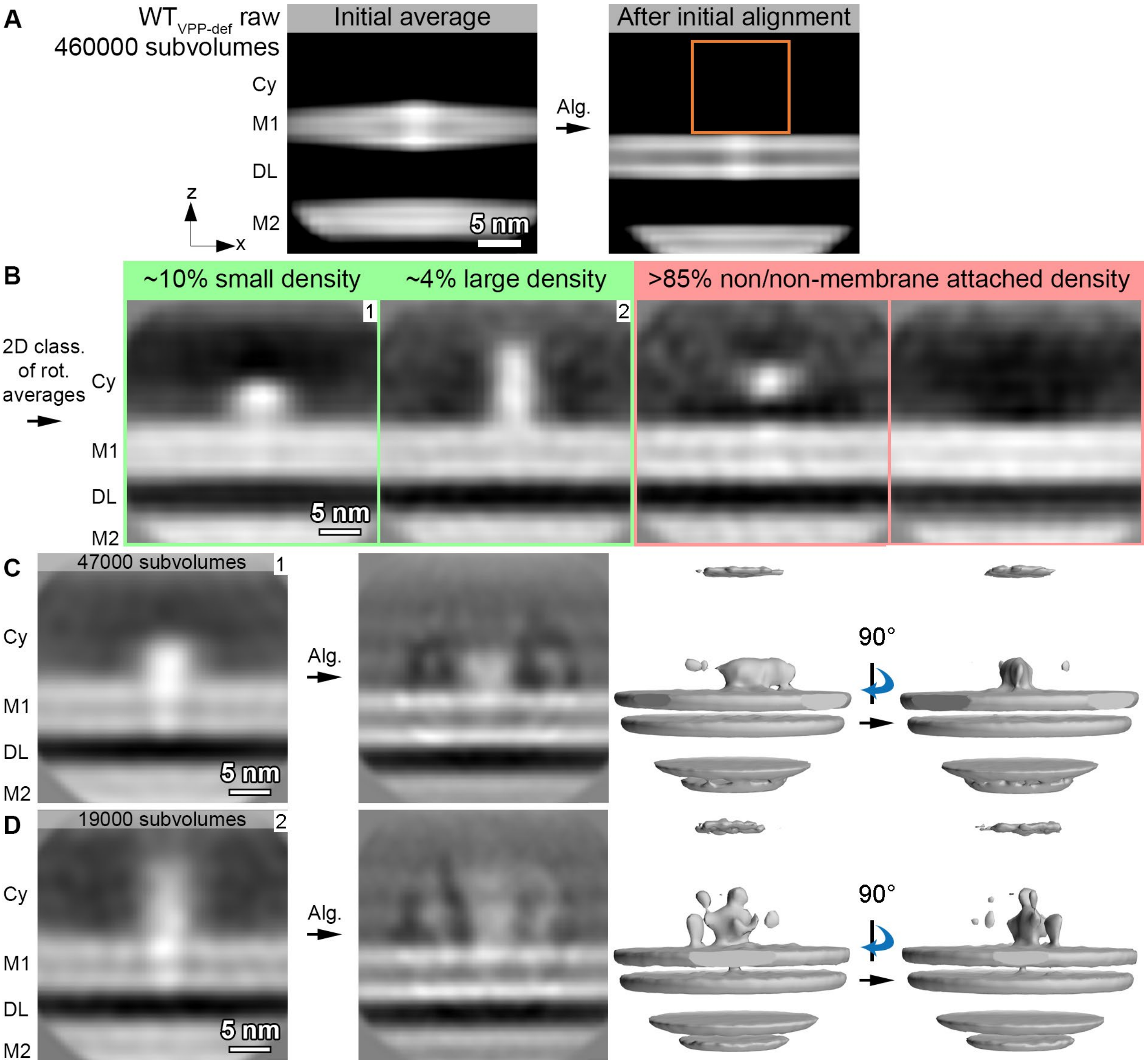

Figure 31: Alignment of cytosolic, disk membrane-attached densities in WT$_{\text{VPP-def}}$ tomograms.
A) Alignment of initially picked membrane densities. M1 and M2 label the first and the second membrane within one disk, respectively, Cy the cytosol and DL the disk lumen. The orange box in the right panel marks the outline of the cylindrical mask used for 2D classification of rotational averages. **B)** Examples for 3D averages of 2D classes. **C)** and **D)** Subvolume alignment of all classes with small and large membrane-attached density, respectively. The left panel shows the initial average of all subvolumes, the right panel the central slice and isosurface representations of the average after alignment in Relion.

All 47000 subvolumes in classes with a small, membrane-attached densities were combined, extracted from 2x binned tomograms (pixel size = 5.24 Å) with Warp and aligned in Relion (Figure 31 C).

However, the subvolume average remained featureless and did not reveal further structural information. Only 19000 subvolumes were assigned to classes with a large membrane-attached density but the stronger signal of the cytosolic density could benefit the alignment. Still, the resulting average did not reveal more structural features (Figure 31 D).

To assess whether the data acquisition with VPP impeded to resolve finer details in the subvolume averages (Turoňová et al., 2020), a similar workflow was performed on a conventional dataset of WT ROS ($\mathrm{WT_{conv}}$). Initially, 303000 subvolumes were extracted. The initial average indicated a strong transmembrane density which was lost during alignment of the subvolumes (Figure 32 A). 2D classification of rotational averages gave similar results as for $\mathrm{WT_{VPP\text{-}def}}$: 8% of the subvolumes were assigned to classes with small density and 3% with a large density attached to the membrane (Figure 32 B). However, alignment of these classes which contained thousands of subvolumes resulted in low-resolution averages that could not be correlated with existing structures of visual proteins.

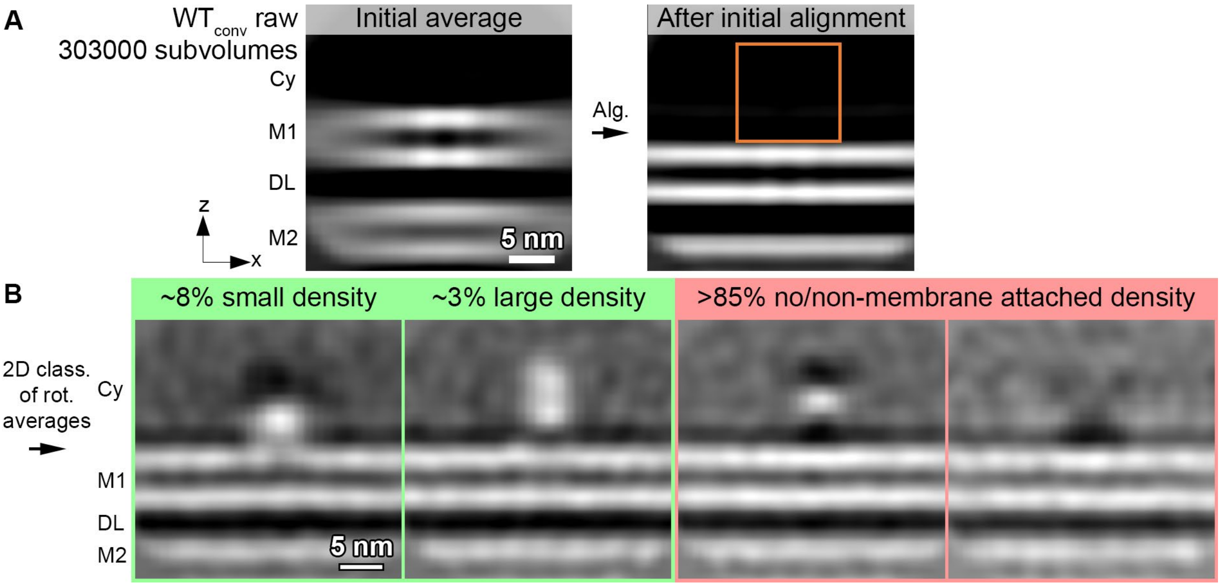

Figure 32: Alignment of cytosolic, disk membrane-attached densities in $\mathrm{WT_{conv}}$ tomograms.
A) Alignment of initially picked transmembrane densities to the disk membrane. The orange box in the right panel marks the outline of a cylindrical mask used for 2D classification of rotational averages. **B)** Examples for 3D averages of 2D classes. M1 and M2 label the first and the second membrane within one disk, respectively, Cy the cytosol and DL the disk lumen.

Again, subvolume averaging of disk membrane-attached densities did not produce results which could be interpreted. The problem was not with the acquisition scheme. Also picking of membrane-attached densities and an initial classification via rotational averages was possible. Furthermore, averaging was not limited by the low amounts of subvolumes as it was the case for disk connectors. But the poor results suggest that the data itself was not suitable for subvolume averaging. Most likely, the currently available alignment and classification software is not able to process heterogeneous, membrane-attached proteins with sizes below 100 kDa in the crowded environment of ROS.

3.7 The molecular organization of the ROS disk rim.

A dominating structural feature of the ROS architecture is the high curvature at the disk rim. There, the bilayer of the disk membrane is bend to a 12 nm radius of curvature which is extraordinarily high. Already in 1987 a crescentic density within the luminal loop was reported as part of a structure referred to as terminal loop complex (Corless et al., 1987). It was proposed that this complex is involved in the organization of the disk rim. But the identification of the proteins giving rise to it and the molecular mechanism of membrane curvature formation remain elusive until today. This chapter describes a subvolume averaging pipeline used to visualize a protein scaffold at disk rim. Then the scaffold is characterized, and the question addressed what protein complex is forming it. In the end the findings are summarized in a model for the 3D organization of the disk rim and a mechanism for the formation of the high membrane curvature is proposed. All datasets, analyzed in this work are summarized in Table 5.

3.7.1 Subvolume averaging reveals a continuous, highly ordered protein scaffold at disk rims.

Subvolume averaging and alignment was employed to study the disk rim in 3D. First, the conventional dataset of ROS in WT mice (WT_{conv}) was analyzed. The initial alignment was performed on 4x binned tomograms (pixel size = 10.48 Å). Splines along the disk rim were manually picked. Initial subvolume extraction points were defined with a distance of 1 nm along the splines. The initial orientations were chosen to align the subvolume z-axis along the spline, while the angle of the in-plane rotation was randomized. The resulting subvolume average contained no features apart from a cylindrical density along the z-axis (Figure 33 A). Subvolumes were aligned to this common reference. After a few iterations, the symmetry was broken, and the average assumed the expected hairpin-like shape of the disk rim. Additionally, three densities inside the disk lumen were resolved, that form continuous rows along the disk rim (Figure 33 B). This first alignment step coarsely determined the angle of the in-plane rotation and the particle positions converged onto the splines (Figure 33 B).

The extraction points were recentered and subvolumes cropped from 2x binned tomograms (pixel size = 0.524 Å). To take a potential symmetry of the scaffold into account, subvolumes were reoriented to align their z-axis perpendicular to the ROS axis, pointing towards the center of the disk and the y-axis parallel to ROS axis. After several alignment iterations, the average indicated a periodic repeat with a length ~4.1 nm along all three rows of density (Figure 33 C). The positions of subvolumes converged to lattice points along the disk rim splines with multiples of 4 nm as predominant distance between nearest neighbors (Figure 33 D). This confirms that the repeat of ~4.1 nm measured in the subvolume average is not an artifact but a feature characteristic to the disk rim scaffold. With this information the number of extraction points was reduced by so-called distance cleaning: amongst all subvolumes only those with the highest similarity to the average determined by the cross-correlation score were retained, while all neighbors within a distance of 4 nm and a lower score were discarded. Furthermore, subvolumes were inspected visually to remove misaligned positions.

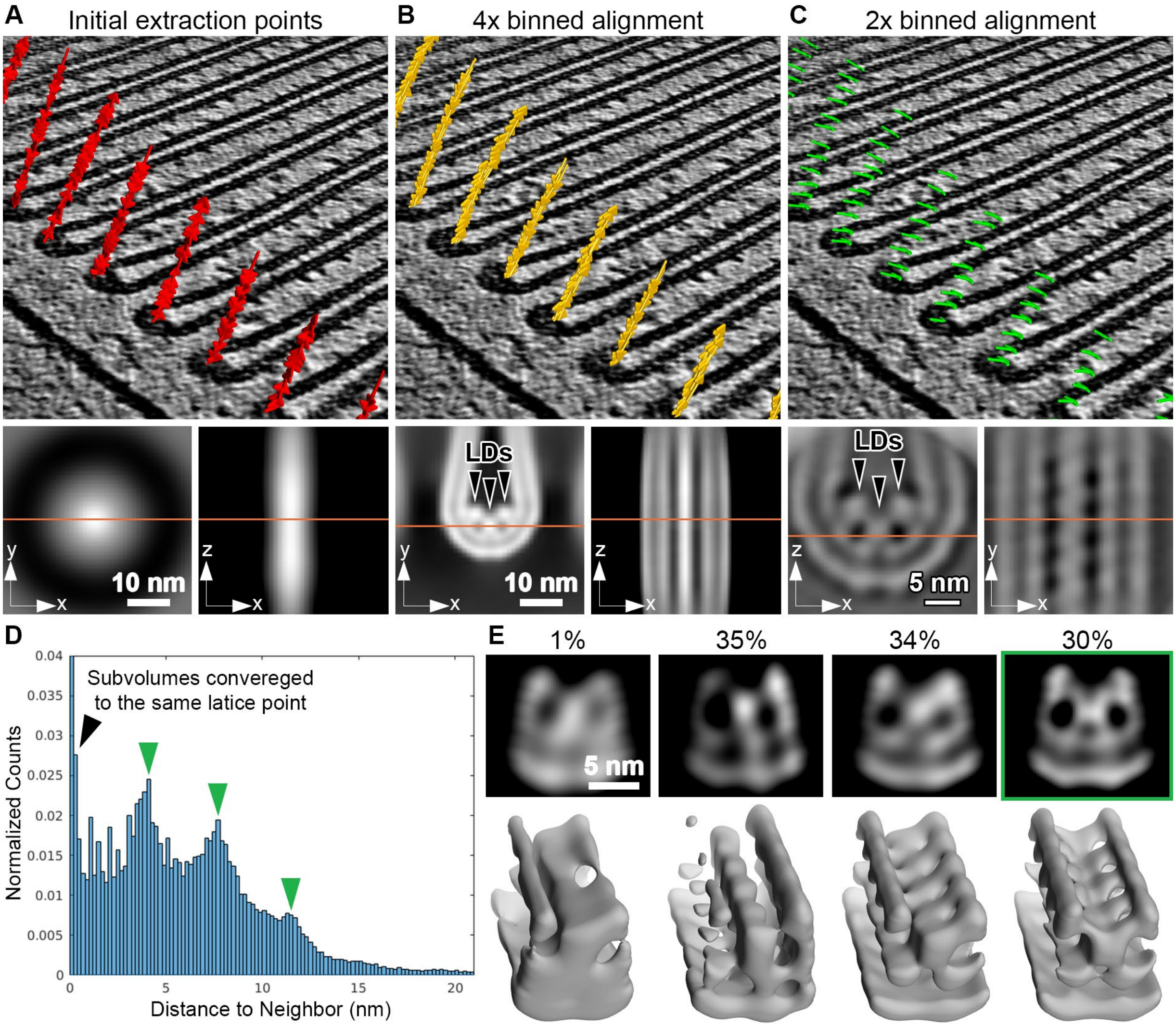

Figure 33: Alignment of disk rim subvolumes in conventional tomograms of WT mice (WT_{conv}).
A-C) Positions and orientations of subvolumes with the corresponding averages for different alignment steps. In the top panel, each arrow represents the position of one subvolume and the arrow direction coincides with the subvolume z-axis. The bottom panel depicts two orthogonal sections through the corresponding subvolume average. The location of the slices through the average are indicated by orange lines. The initial extraction points are shown in A, the refined positions after alignment of 4x binned subvolumes in B and the distance-cleaned positions after alignment of 2x binned subvolumes in C. Luminal densities (LDs) are indicated by black arrowheads. **D)** Histogram of distance to 10 nearest neighbors for positions of 2x binned particles before distance cleaning. Green arrowheads indicate peaks at multiples of 4 nm for subvolumes partially converged into lattice points. **E)** Examples for class averages obtained by classification of 3D subvolumes in Relion (Scheres, 2016). The upper panel shows a slice through the center of the average, the lower panel the isosurface representation. The class highlighted in the green frame was used for further processing.

The remaining subvolume extraction points were centered on the central row of density, extracted from unbinned (pixel size = 0.262 nm) tomograms and preprocessed in Warp (Tegunov et al., 2019). Subsequently, the subvolumes were aligned, averaged and classified by the regularized likelihood optimization algorithms implemented in Relion (Bharat et al., 2015). The mask used for alignment and classification was wedge-shaped, centered around the central row of density and contained 4 repeats along the row of density. The classification (Scheres, 2016) was crucial as it revealed the intrinsic heterogeneity of the disk rim. This step was needed to separate subvolumes containing the signal of the highly ordered scaffold from patches which were distorted or deformed. Furthermore, slight variations in the rim diameters are forcing the scaffold into different conformations. This heterogeneity is a mayor limiting factor to resolve the rim scaffold at high resolution. Figure 33 E depicts examples of class averages obtained with Relion. Three of the four classes appear less symmetric than the previous average of 2x binned particles (Figure 33 C), probably because the corresponding subvolumes contained the signal of corrupted patches of the disk rim. However, one class indicates a high degree of order. Subvolumes of this classes were chosen and separately aligned in Relion. The refined subvolume positions and orientations were imported into the *M* software which uses the information to refine the alignment of the tomographic tilt-series (Tegunov et al., 2020). Last step was to extract unbinned subvolumes from tomograms with refined tilt-series alignment and to run another round of alignment and classification in Relion.

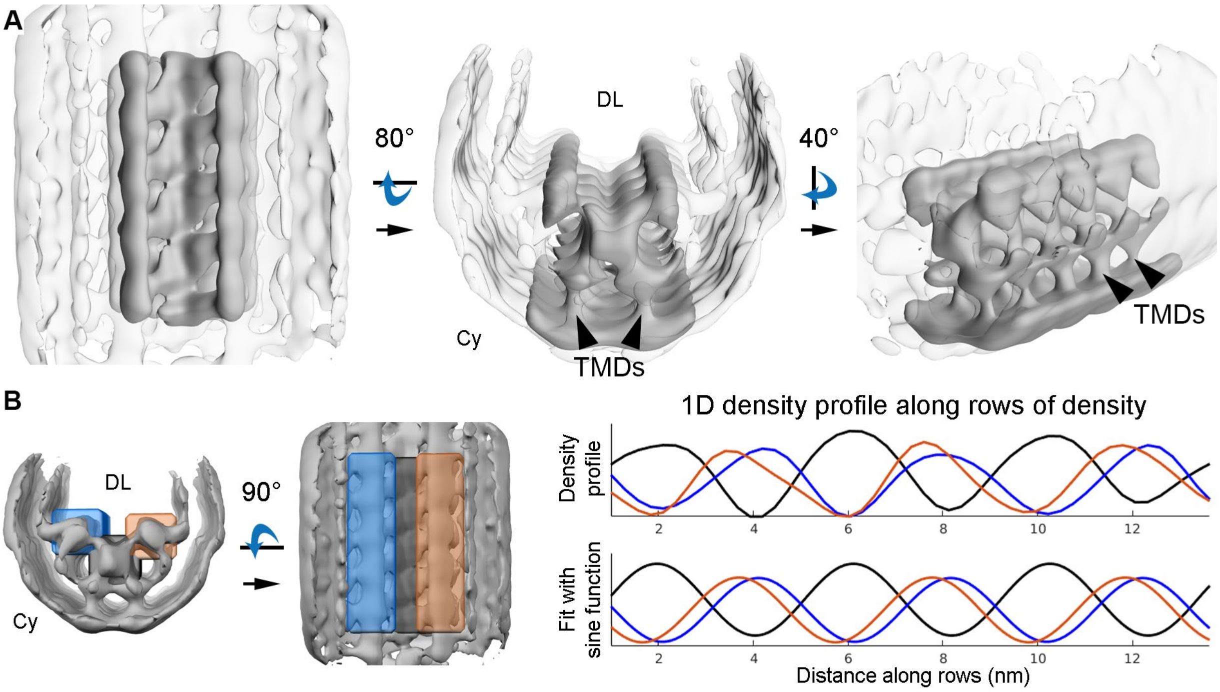

Sine function used for the fit: $y(x) = y_0 + A \sin(w_0 x + p)$

row	y_0 (a.u.)	A (a.u.)	w_0 (1/pix)	p	R^2	Repeat length (nm)	Offset to center (repeats)
central	0.52	0.40	0.40	0.90	0.96	4.1	-
clockwise	0.41	0.36	0.4	4.40	0.91	4.1	0.56
counterclockwise	0.41	0.36	0.41	3.70	0.96	4.1	0.45

Figure 34: Subvolume average of the central density row for the WT_{conv} dataset.
A) Isosurface representation of the average from different perspectives. The central row of density with its contacts to the peripheral rows is depicted in solid grey and the signal of the whole disk rim in transparent grey. Black arrowheads indicate transmembrane densities (TMDs). **B)** Density profiles along the three density rows. The left panel indicates the orientation of the three masks used to calculate the 1D density profiles in the right panel. The top right panel shows the actual 1D signals and the middle right panel the fitted sine-functions. The parameters of the fit are listed in the bottom panel. DL denotes the disk lumen and Cy the cytosol.

The resulting average indicates a highly ordered array of repeats organized in three interconnected rows which form a continuous belt along the disk rim (Figure 34 A). The view from the disk lumen onto the scaffold shows a C2 symmetry with respect to an axis perpendicular the ROS axis, pointing towards the center of the disk. However, at the achieved low resolution this cannot be confirmed and taking C2 symmetry into account during subvolume alignment did not improve the global resolution. Fitting the density profiles along the rows with sine functions shows a repeat length of 4.1 nm for all three rows and a shift of half a repeat between the central and peripheral rows (Figure 34 B).

The repeat has a height of ~11 nm, stretching from the cytosol into the disk lumen (along z-axis in Figure 35 A). Slices taken at different z-height reveal further structural features of the repeat (Figure 35 A). Each repeat contributes two cytosolic densities. This 1.4 nm cytosolic domain is followed by a transmembrane domain extending over 5.5 nm with two diverging densities. The two separate densities converge inside the disk lumen into a globular domain with a height of 2.6 nm. There, the whole row of repeats seems to be in close contact. Further into the disk lumen the density within one repeat splits into two diverging arms which connects the central to the peripheral rows. A single repeat of the central row contacts two peripheral repeats on each of the peripheral rows that are located diagonally with respect to the central repeat. The head domain has a height of 1.6 nm (Figure 35 A).

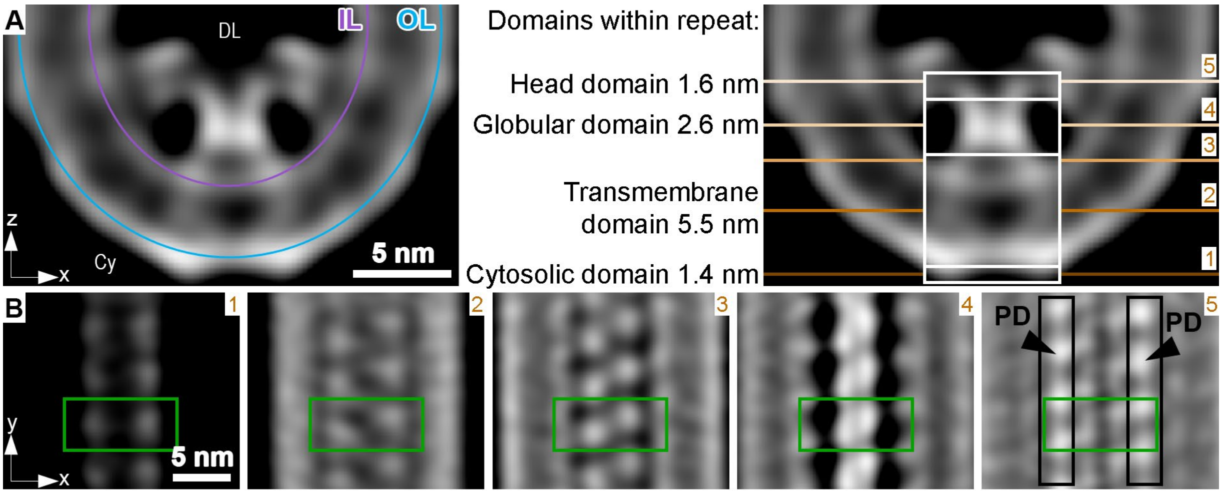

Figure 35: Structure of the individual repeat.
A) Cross-section through the disk rim and the domains of the repeat in the central row. The signal of the inner- (IL) and outer leaflet (OL) are indicated by a purple and blue line, respectively. **B)** Orthogonal slices of the central density row at different z-height. The green box is centered on the same repeat throughout the slices. In the right panel, the signal of the peripheral densities (PD) is marked by black boxes. The location of the slices is indicated by orange, numbered lines in the right panel of A. DL denotes the disk lumen and Cy the cytosol.

The density of the peripheral rows was aligned and averaged in a similar way using Warp, Relion and *M*. Initially, the clockwise and counterclockwise row were aligned with respect to each other. This required for the clockwise row (CW) a rotation of 63° about the y-axis and for the counterclockwise row (CCW), first a rotated of 180° about the z-axis followed by 63° about the y-axis (Figure 10 B). Afterwards the extraction points centered on the respective row. The subvolumes of the CW and CCW row were aligned separately and together (CW + CCW). The global resolution of CW + CCW was with 18.2 Å slightly higher in comparison to the average for each row alone (Figure 36 A). The symmetry operation required to combine the CW and CCW dataset and the higher quality of the resulting average further indicate the C2 symmetry of the disk rim scaffold. The shape (Figure 36 B) and the dimensions (Figure 36 C) of repeats in the peripheral row are similar to the central row with one major difference: inside the lumen, a pronounced density connects the repeats on the outside of the scaffold opposite of the contact to the central density (Figure 36 D).

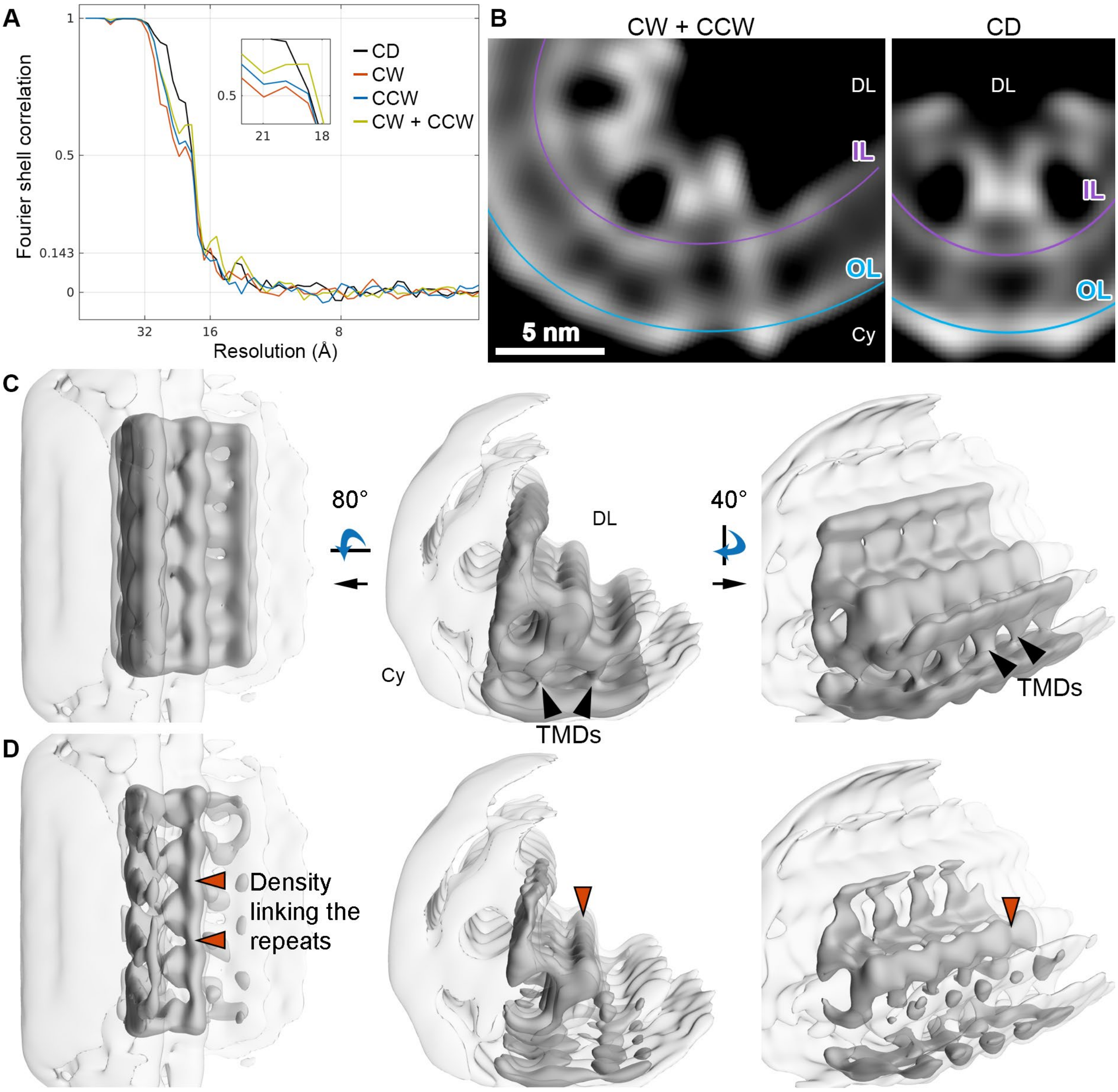

Figure 36: Subvolume average of the peripheral density rows for the WT$_{\mathrm{conv}}$ dataset.
A) Fourier shell correlation (FSC) curve for the averages of central density (CD) row, clockwise (CW) and counterclockwise (CCW) rows separate and both peripheral rows combined (CW + CCW). **B)** Cross-section through the average for the combined peripheral rows (left panel) and the central density row (right panel). The signal of the inner (IL) and outer leaflet (OL) are indicated by a purple and blue line, respectively. **C)** Isosurface representations of the average for the peripheral rows from different perspectives. The peripheral row and its contact to the neighboring row is shown in solid grey, the signal of the full disk rim in transparent grey. Black arrowheads indicate transmembrane densities (TMDs). **D)** Same perspectives as in C but with isosurface representations at higher threshold. The density which links repeats of the peripheral row is highlighted by orange arrow heads. DL denotes the disk lumen and Cy the cytosol.

The final averages for the central and the peripheral row are resolved to the same global resolution of ~19 Å (Figure 36 B). However, the overall map quality for the peripheral rows is worse than for the central row even though 5x more subvolumes contributed to the final average (Table 5). This indicates two aspects:

1. The achieved resolution is not limited the by number of subvolumes used for averaging but rather the flexibility and heterogeneity of the disk rim.
2. The peripheral rows lock the central row in a more stable environment while they are themselves more flexible.

To avoid limitations due to the flexibility of an entire densities row comprising 4 repeats, various software packages were used to focus the alignment on individual repeats, which did not further improve the resolution. This indicates that the heterogeneity is inherent to the repeat and does not only arise from the flexibility of the whole disk rim scaffold.

A reason for the unexpectedly low resolution of the apparently highly ordered disk rim scaffold could be polarity. For example, cytoskeletal actin filaments assemble with a certain directionality (Pollard, 2016). A recent cryo-ET study of actin filaments was only able to obtain high-resolution averages after the polarity of the individual subvolumes was considered during alignment (Burbaum et al., 2020). Averaging of subvolumes with random polarity produced a featureless density map. In the case of the disk rim, polarity would exclude the C2 symmetry in the way it was proposed here. However, averaging subvolumes with random polarity could produce a density map that appears to have C2 symmetry. The quality of the ROS data does not allow to observe polarity directly in the tomograms or to determine it *a priori*. Other experiments are required to investigate the existence of polarity in the disk rim scaffold. One possibility are *in vitro* assembly experiments of the isolated scaffold protein. However, the identity of the scaffold protein was only hypothesized previously but never solidly confirmed.

3.7.2 Absence of the disk rim protein ABCA4 does not change the structure of the disk rim scaffold.

The question what proteins are forming the scaffold at the disk rim was still open. Mammalian ROS contain three abundant membrane proteins with large disk luminal domains that localize exclusively to the disk rim. First, the rod cell-specific ATP-binding cassette transporter (ABCA4), which is important for the long-term viability of the retina but is not known to be of strutural importance (Tsybovsky et al., 2013). Second, the two small transmembrane proteins Peripherin-2 (PRPH2) (Molday et al., 1987) and ROS membrane protein 1 (ROM1) (Bascom et al., 1992). They are homologs (Kevany et al., 2013) and are known to associate non-covalently into homo- and hetero-tetramers (Goldberg et al., 1996). *In vitro,* they form oligomers through disulfide bond stabilization (C. J. R. Loewen et al., 2000) and further induce membrane curvature when reconstituted into lipid vesicles (Kevany et al., 2013). Therefore, PRPH2 and ROM1 represented reasonable candidates to be involved in the formation of the high-curvature disk rim.

To clarify the protein identity of the building blocks in the rim scaffold, ROS of homozygote ABCA4 knockout (*Abca4*$^{-/-}$) mice were investigated. ROS were extracted and prepared for cryo-ET as described for the WT. Due to an error in the ROS extraction, the frozen biological material on the grids was thinner than for the WT. Even single ROS were rarely found in the SEM, in contrast to WT preparations where ROS were tightly packed on grids and even formed occasionally multi-layers. The single isolated ROS in *Abca4*$^{-/-}$ preparations were exposed to strong forces during blotting and their disk stacks widespread damaged. Furthermore, the thin material complicated FIB-milling. The lack of support by surrounding material caused many lamellae to bend or break. Thus, the overall quality of the lamellae was worse than for the WT and less positions suitable for data acquisition were found. Tilt-series were acquired with Volta phase plate (VPP) in focus. This dataset will be referred to as *Abca4*$^{-/-}$$_{\text{VPP-inf}}$. The ultrastructure of ROS in the rare, well-preserved regions appeared identical to the WT (Figure 37 A).

The disk rims of the *Abca4*$^{-/-}$$_{\text{VPP-inf}}$ dataset were analyzed similar to the WT. Initial subvolume extraction points were selected along splines at the outer periphery of the disk rim. Initial alignment was performed on 4x binned data, the results distance cleaned, and the remaining particles inspected visually. Particle positions where recentered and subvolumes extracted from unbinned tomograms. Subvolume alignment and classification was performed with a wedge-shaped mask around the central density row which comprised 4 repeats. As the data was acquired in focus (Danev et al., 2016), the CTF could not be fitted and corrected which is a requirement for certain software packages. Therefore, Warp and *M* could not be used for data processing. To compare the subvolume average of disk rims in *Abca*$^{-/-}$$_{\text{VPP-inf}}$, a VPP dataset of WT ROS was acquired in focus as control (WT$_{\text{VPP-inf}}$). For the analysis of WT$_{\text{VPP-inf}}$ disk rims, the same microscope settings and processing pipeline was used as for *Abca4*$^{-/-}$$_{\text{VPP-inf}}$.

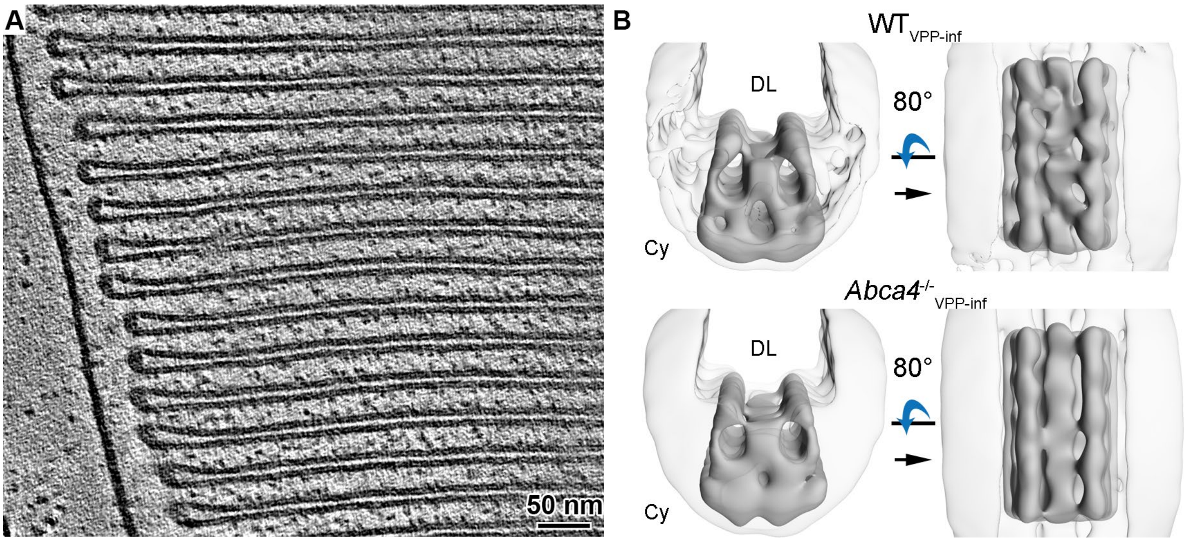

Figure 37: ROS architecture and disk rim averages of ROS in the *Abca4*$^{-/-}$$_{\text{VPP-inf}}$ dataset.
(A) Slice of VPP tomogram showing ROS from *Abca4*$^{-/-}$ mice. The ultrastructure appears similar to the WT.
(B) Isosurface representations of disk rim subvolume averages derived from VPP datasets. Averages of WT$_{\text{VPP-inf}}$ as control and *Abca4*$^{-/-}$$_{\text{VPP-inf}}$ are depicted in the top and bottom panel, respectively. The central row with its contacts to the peripheral rows are illustrated in solid grey, the signal of the whole disk rim in transparent grey. DL denotes the disk lumen and Cy the cytosol.

The resulting subvolume averages are similar in appearance. In both cases, three densities protruding into the disk lumen were observed which form continuous, interconnected rows along the disk rim (Figure 37 B). This is in good agreement with the average obtained from conventional tomograms WT$_{\text{conv}}$ and suggests that disk rim scaffold has the same organization in WT and *Abca4*$^{-/-}$ mice. But in contrast to WT$_{\text{conv}}$ the scaffold appears less ordered and the repeat is not as pronounced. The estimated global resolution for the VPP averages is with 23 Å and 28 Å for WT$_{\text{VPP-inf}}$ and *Abca4*$^{-/-}$$_{\text{VPP-inf}}$, respectively, worse than for WT$_{\text{conv}}$ with 19 Å (Figure 38 A). However, at these resolutions better than 30 Å, the repeats with a distance of 41 Å should be clearly resolved which is not the case for the VPP averages (Figure 37 B). Previously, it was reported that the estimated resolution of VPP averages did not correspond to the level of detail which was observed visually in the averages (Turoňová et al., 2020). As a likely reason for this, the authors suggest inaccurate spatial frequency weighting particularly of the heavily oversampled low frequencies which are further amplified by using the VPP. This in combination with the smaller amount and the overall lower quality of the *Abca4*$^{-/-}$$_{\text{VPP-inf}}$ dataset can explain why the repeat along the rows were only vaguely resolved. However, the comparison of cross-sections perpendicular to the central row reveals a similar structure for the disk rim scaffold in WT$_{\text{conv}}$ and the two VPP datasets. In all three averages, the central row exhibits two small cytosolic densities, two diverging transmembrane domains and a globular domain in the disk lumen which establishes the contact to the peripheral rows (Figure 38 B).

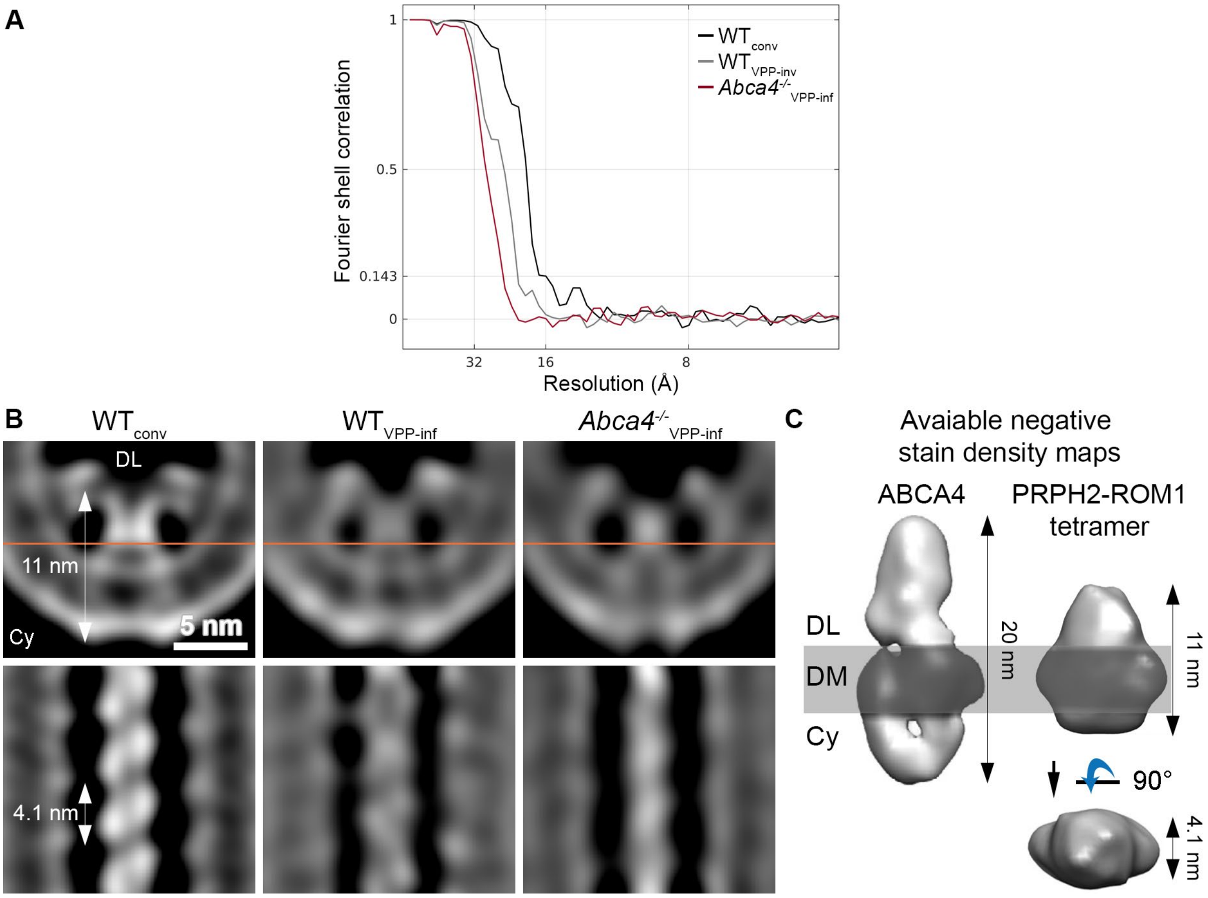

Figure 38: Comparison of disk rim averages obtained from WT and *Abca4*$^{-/-}$ mice.
A) Fourier shell correlation for the averages of conventional WT dataset (WT$_{\text{conv}}$), and the two VPP datasets acquired in focus: on ROS of WT mice (WT$_{\text{VPP-inf}}$) and on *Abca4*$^{-/-}$ mice (*Abca4*$^{-/-}$$_{\text{VPP-inf}}$). **B)** Orthogonal slices through disk rim averages. The orange line in the upper panel indicates the location of the slice in the bottom panel. **C)** Available negative stain density maps for protein complexes located at the disk rim. The density map of ABCA4 was adapted from (Tsybovsky et al., 2014) and for the PRPH2-ROM1 tetramer from (Kevany et al., 2013). DL indicates the disk lumen, DM the disk membrane and Cy the cytosol.

Therefore, it was concluded that the absence of ABCA4 does not change the protein scaffold at the disk rim and the apparent differences between averages were caused by the varying data quality and the data collection method. Furthermore, the shape of the three densities in the disk rim cross sections fits the dimensions of the negative stain density map associated with PRPH2-ROM1 tetramers (Kevany et al., 2013), while it is distinctly different from the negative stain density map determined for ABCA4 (Tsybovsky et al., 2013) (Figure 38 B). Hence, it was proposed that PRPH2-ROM1 tetramers are the basic building block of the disk rim scaffold as there is no other protein complex located at disk rims that is abundant enough to form the observed continuous protein scaffold along the disk rim.

3.7.3 A new model for the disk rim organization: the high membrane curvature is enforced by three interconnected rows of PRPH2-ROM1 tetramers.

The results of subvolume averaging reveal a repetitive protein scaffold at the disk rim. In terms of the global resolution the final average is worse than for previously reported protein scaffolds (Dodonova et al., 2017; Schur et al., 2016). Still, the data provides new insight into the architecture and organization of the ROS disk rim at an hitherto unprecedented level of detail. The findings are summarized in the following model.

The disk rim scaffold is composed of three interconnected rows of density which form a continuous belt along the disk rim. The three rows have a translational symmetry with a repeat distance of 4.1 nm along the disk rim and the peripheral rows have a shift of half a repeat with respect to the central row. The angle between the repeats of peripheral and central rows is ~63° (Figure 39 A). Each repeat represents a PRPH2-ROM1 tetramer which spans 11 nm from the cytosol into the disk lumen and resemble the shape of a tooth (Figure 39 B). In the case of the central row the roots of the tooth are composed of two separate small cytosolic densities, followed by two diverging transmembrane densities which converge inside the disk lumen into a globular domain. Here, the neighboring tetramers within a row are in contact with each other which probably holds them together. Furthest into the disk lumen, the tooth-shaped repeat has a small head domain. There, two diverging densities are observed which form the only apparent contacts to tetramers on neighboring rows. One tetramer of the central row is connected to two other repeats. One of them are on each peripheral row located on a diagonal with respect to the tetramer in the center. Tetramers in the peripheral rows have a similar shape but are connected differently to neighbors. The contact to the central row is only formed in the inside of the scaffold. On the outside, the neighboring tetramers within the same row are linked to each other. At the current resolution, the rim scaffold seems to have a C2 symmetry which is compatible with the C2 symmetry that was proposed for the PRPH2-ROM1 tetramer based on the negative stain map (Kevany et al., 2013) and would exclude the possibility of a rim scaffold with polarity. However, an average of higher quality is required to confirm that. The low resolution of the resulting averages can have different reasons. The disk rim is a flexible structure with varying diameters which implies that the scaffold needs to be flexible to adapt to these variations. Additionally, ignoring the flexibility of the whole rim by focusing the alignment on the individual repeat instead of several repeats did not improve the global resolution. This indicates that the repeat itself is heterogeneous or flexible. The tetramers isolated from native source are not strictly composed of two PRPH2 and two ROM1 proteins but can have different stoichiometries including homo-tetramers which already introduces a degree of heterogeneity (C. J. R. Loewen et al., 2000).

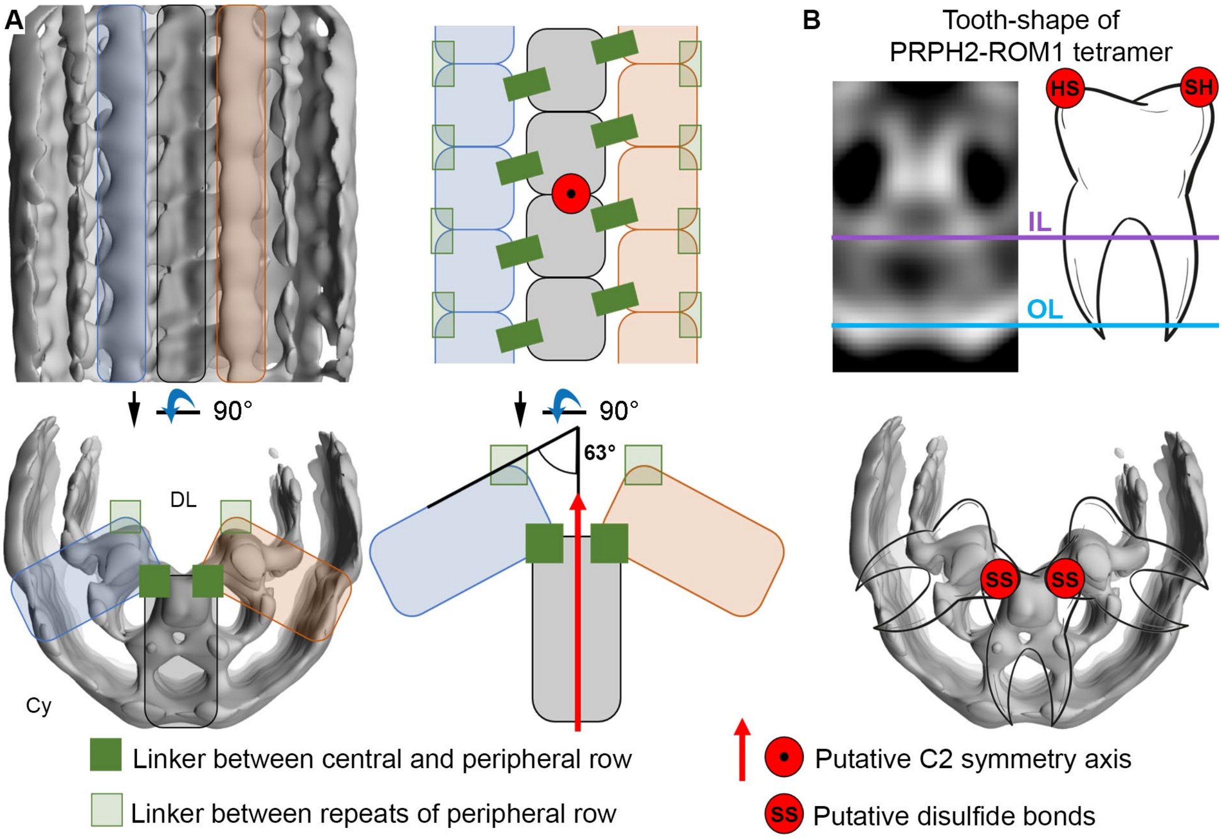

Figure 39: Model for the organization of the ROS disk rim scaffold.
A) The general organization of the disk rim scaffold. **B)** The shape of the repeats. The repeats are hypothesized to be PRPH2-ROM1 tetramers which resample the shape of a tooth. PRPH2-ROM1 tetramers form disulfide bond stabilized oligomers. The responsible residues are hypothesized to be in head domain of the tetramer. DL denotes the disk lumen and Cy the cytosol.

Apart from this general characterization of the disk rim scaffold, some assumptions can be made based on previous experiments. Polymers of PRPH2-ROM1 tetramers are known to be stabilized by disulfide bonds (C. J. R. Loewen et al., 2000). Presumably, the necessary residues are in the head domain of tetramers and responsible for the formation of the contacts between rows and between neighboring tetramers in the peripheral rows. The model presented here hypothesizes that the repeats are tetramers formed by PRPH2 and ROM1 monomers. However, only two densities per repeat are resolved in the subvolume averages (Figure 35 B). It is known that the tetramer assemble via dimers (C. J. Loewen et al., 2001). Therefore, it seems reasonable to assume that the two densities within a single repeat correspond to two PRPH2-ROM1 dimers.

Based on the data presented, a mechanism of curvature formation is proposed. The disk rim is organized by a scaffold of three rows of PRPH2-ROM1 tetramers. The binding interface of the tetramers and the individual rows is realized in the luminal domain of the tetramer whereas the contacts between the rows are facilitated by disulfide bonds. Each tetramer contributes two diverging transmembrane densities, which displace lipids in the inner membrane leaflet of the disk rim by protein. A single tetramer cannot induce membrane curvature to the observed extend. It requires a scaffold of three tightly associated rows of tetramers to force the membrane into this highly curved geometry. This hypothesis is compatible with the observation that many pathological mutations of PRPH2 affect its luminal domain (Kevany et al., 2013). It seems possible that these mutations impair the formation of tetramers, rows of tetramer or the disulfide bond stabilized oligomerization of tetramers which can cause disk distortions during morphogenesis or completely prevent formation of ROS disks. This can disrupt the structural integrity of ROS, compromise the viability of the retina and ultimately lead to blindness (Boon et al., 2008; Kevany et al., 2013).

4 Conclusion and outlook

The aim of this thesis was to answer fundamental questions about the molecular organization of ROS using WT mice as a study model. First, a novel ROS preparation for cryo-ET was established for faster, easier and gentler handling of the tissue than previously reported (Gunkel et al., 2015; Nickell et al., 2007). In the future, ROS damage could further be reduced by high-pressure freezing entire isolated retinas. This would allow volume imaging of the retina by cryo-serial milling and block face imaging, and lift-out methods could be used to obtain optimally preserved lamellae. Still, the presented ROS cryo-preparation produced structurally well-preserved ROS which were used for imaging. The resulting tomograms revealed the supramolecular organization and the molecular landscape of ROS at an unprecedented level of detail.

The analysis of cytosolic densities was only briefly touched as the small size, flexibility and heterogeneity of the proteins made subvolume averaging in the crowded membrane environment of ROS a task beyond the abilities of current software. The identification of these cytosolic densities will likely require data acquisition at higher magnification with a more sophisticated tilt-scheme like the Hagen scheme (Turoňová et al., 2020). This also holds true for studies of the Rhodopsin organization within disk membranes. Rho is a 36 kDa transmembrane protein that is almost fully immersed in the membrane, making it particularly challenging to resolve. A Rho dimers structure derived from an EM map is available and could be used for Rho template-matching in tomograms (D. Y. Zhao et al., 2019).

The membrane architecture of ROS was characterized, providing a refined measurement of distances characteristic of the ROS disk stack. Two key features were identified: (i) the close stacking of membrane disks and (ii) the high membrane curvature at disk rims. For the maintenance of the close disk stacking, two main mechanisms have previously been proposed. On the one hand, it was suggested that membranes of neighboring disks are continuous (Robertson, 1965). This hypothesis was rejected by demonstrating that it was based on a misinterpretation of 2D TEM images. On the other hand, it was proposed that molecular connectors are involved in the maintenance of the disk stack (Goldberg et al., 2016). Here, two types of connectors were resolved between disks. A short and abundant species were located at the disk rim and was assigned to GARP2. Noteworthy, no obvious transmembrane component links the disk rim connectors to the scaffold at the outer disk periphery as suggested in (Corless et al., 1987). Longer and scarcer connectors were found in the disk interior which were hypothesized to be PDE6 in accordance with previous results. This hypothesis, however, could not be confirmed based solely on the data presented in this work. In the future, cryo-ET analysis of truncation mutants for PDE6 and GARP2 should allow for their unambiguous assignment and highlight their contribution to the structural integrity of ROS.

Large densities attached to both the disk rims and the PM were observed but they could not be assigned to continuous connectors linking both membrane domains. Such connectors were previously suggested to be formed by CNGC proteins. Noteworthy, the underlying and widely accepted model assumes a distance of 10 nm between PM and disk rims (Figure 40 A, (Batra-Safferling et al., 2006)) which was measured in amphibians (Roof et al., 1982) but is different in vertebrates like mice where the distance is 25 nm.

The high curvature at disk rims was investigated by subvolume averaging revealing a repetitive protein scaffold composed of three interconnected rows of density forming a continuous belt along the disk rim. Evidence is provided that the scaffold repeats are PRPH2-ROM1 tetramers whereas ABCA4 is likely excluded from this highly ordered scaffold. The tooth-like shape of the tetramers suggests that oligomerization of PRPH2 and ROM1 is achieved by their disk luminal domains, while their transmembrane domains, in combination with the three tightly associated rows of tetramers, force the membrane into a highly curved geometry. This finding is in accordance with the observation that many pathological mutations of PRPH2 are located in its disk luminal domain (Boon et al., 2008). These mutations may perturb formation or oligomerization of tetramers and thus compromise the integrity of ROS or even prevent ROS morphogenesis. This can cause progressive retinal degeneration and lead to blindness. Unfortunately, the low resolution of the obtained density maps did not permit for atomic model building which would, ultimately, have been required to confirm PRPH2 and ROM1 as building blocks of the rim scaffold. To achieve this, studies of purified PRPH2-ROM1 tetramers by cryo-EM single particle analysis or tetramers reconstituted into lipid vesicles by cryo-ET may prove fruitful.

In summary, this thesis describes the molecular architecture of ROS at an unprecedented level of detail. The findings enhance our understanding of how the highly ordered stack of ROS disk membranes is maintained and provides insights into how certain mutations perturb ROS ultrastructure. An updated model for the ROS organization is shown in Figure 40 B.

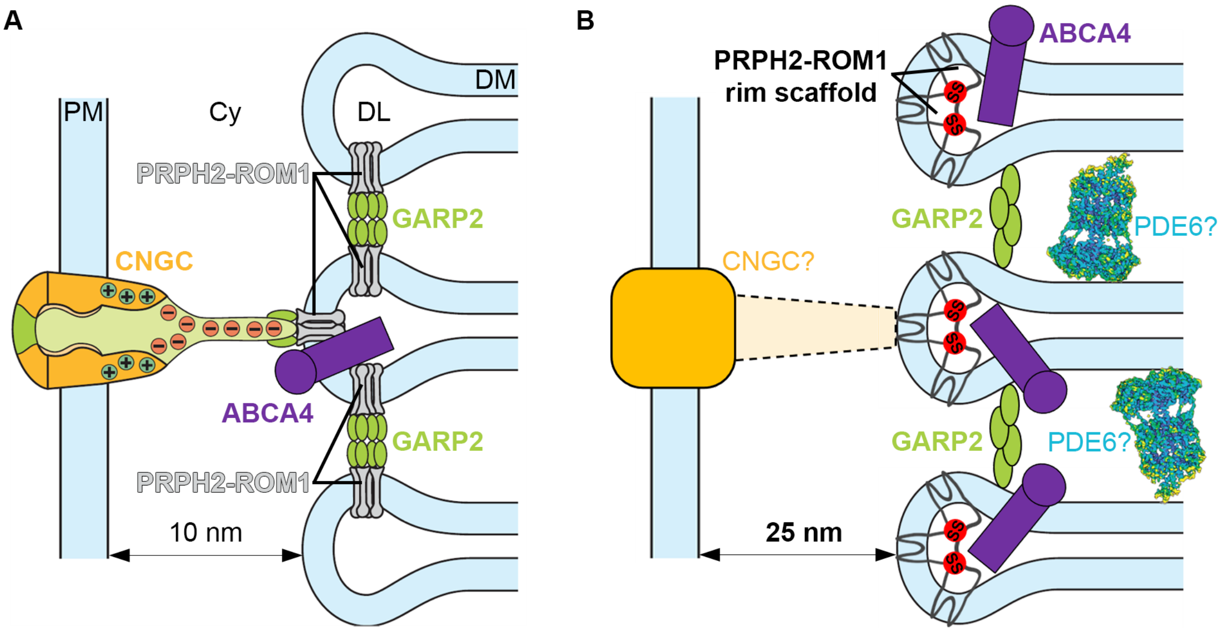

Figure 40: An updated model for the organization of the ROS disk stack in mammalians.
A) Model for ROS disk stack organization as previously proposed in (Batra-Safferling et al., 2006). The distance of 10 nm between PM and disk rim is only true for amphibians but not vertebrates. **B)** An updated model for the disk stack organization as described in this work. The hypothesis of CNGC and PDE6 as connectors between disk rims and PM or between disk, respectively, could not be confirmed (indicated by question mark). The PDE6 density map was adapted from (Gulati et al., 2019). PM denotes the plasma membrane, Cy the cytosol, DL the disk lumen and DM the disk membrane.

5 Appendix

5.1 Abbreviations

Table 7: List of abbreviations.

1D, 2D, 3D	One-, two- and three-dimensional
ABCA4	Photoreceptor cell specific ATP binding cassette transporter
$\mathit{Abca4}^{-/-}$	ABCA4 knockout mice
$\mathit{Abca4}^{-/-}_{\text{VPP-inf}}$	Dataset acquired with VPP in focus on ROS of $\mathit{Abca4}^{-/-}$ mice
AP	Alkaline phosphatase
Arr	Arrestin
ATP	Adenosine triphosphate
CC	Connecting cilium
CCD	Charged coupled device
CCW	Counterclockwise row of disk rim scaffold
CD	Central density row of disk rim scaffold
cG	Cyclic guanosine monophosphate
CNGC	Cyclic nucleotide gated cation channel
cryo-EM	Cryo-electron microscopy
cryo-ET	Cryo-electron tomography
cryo-SMBFI	Cryo-serial milling and block face imaging
CTF	Contrast transfer function
CW	Clockwise density row of disk rim scaffold
Cy	Cytosol
DED	Direct electron Detectors
DI	Disk incisure
DL	Disk lumen
DM	Disk membrane
DR	Disk rim
EM	Electron microscopy
ET	Electron tomography
FIB	Focused ion beam
FT	Fourier transform
GARP	Glutamic acid-rich protein
GC	Guanylyl cyclase
GMP	Guanosine monohosphate
Gt	Transducin
GTP	Guanosine triphosphate
Gα	α-subunit of transducin

IL	Inner leaflet of membrane bilayer
LD	Luminal density
LFQ	Label-free quantification
LM	Light microscopy
MS	Mass spectrometry
OL	Outer leaflet of membrane bilayer
PD	Peripheral density rows of disk rim scaffold (meaning CW and CCW)
PDE6	Phosphodiesterase 6
PDE6α,β,γ	α,β,γ-subunit of PDE6
Ph	Photon
PM	Plasma membrane
PRPH2	Peripherin-2
PSF	Point spread function
Pt	Platinum
PVDF	Polyvinylidendifluorid
rd1/+	Mice heterozygous for the *rd1* mutation
rd1/+$_{\text{VPP-inf}}$	Dataset acquired with VPP in focus on ROS of *rd1/+* mice
Rho	Rhodopsin
RIS	Rod inner segment
RK	Rhodopsin Kinase
ROM1	ROS membrane protein 1
ROS	Rod outer segment
SDS-PAGE	Sodium dodecyl sulfate polyacrylamide gel electrophoresis
SEM	Scanning electrom microscope
SNR	Signal-to-Noise ratio
SPA	Single particle analysis
std	Standard deviation
TEM	Transmission electron microscope
TMD	Transmembrane density
VPP	Volta phase plate
WT	Wild type mice
WT$_{\text{conv}}$	Conventional dataset acquired without VPP on ROS of WT mice
WT$_{\text{VPP-def}}$	Dataset acquired with VPP and defocus on ROS of WT mice
WT$_{\text{VPP-inf}}$	Dataset acquired with VPP in focus on ROS of WT mice

5.2 Bibliography

Adrian, M., Dubochet, J., Lepault, J., & McDowall, A. W. (1984). Cryo-electron microscopy of viruses. *Nature*, *308*(5954), 32–36.

Al-Amoudi, A., Studer, D., & Dubochet, J. (2005). Cutting artefacts and cutting process in vitreous sections for cryo-electron microscopy. *Journal of Structural Biology*, *150*(1), 109–121.

Arnold, J., Mahamid, J., Lucic, V., … P., J. M. (2016). Site-Specific Cryo-focused Ion Beam Sample Preparation Guided by 3D Correlative Microscopy. *Biophysical Journal*, *110*(4), 860–869.

Bascom, R. A., Manara, S., Collins, L., … McInnes, R. R. (1992). Cloning of the cDNA for a novel photoreceptor membrane protein (rom-1) identifies a disk rim protein family implicated in human retinopathies. *Neuron*, *8*(6), 1171–1184.

Batra-Safferling, R., Abarca-Heidemann, K., Körschen, H. G., … Kaupp, U. B. (2006). Glutamic acid-rich proteins of rod photoreceptors are natively unfolded. *The Journal of Biological Chemistry*, *281*(3), 1449–1460.

Bharat, T. A. M., Russo, C. J., Löwe, J., … Scheres, S. H. W. (2015). Advances in Single-Particle Electron Cryomicroscopy Structure Determination applied to Sub-tomogram Averaging. *Structure*, *23*(9), 1743–1753.

Bharat, T. A. M., & Scheres, S. H. W. (2016). Resolving macromolecular structures from electron cryo-tomography data using subtomogram averaging in RELION. *Nature Protocols*, *11*(11), 2054–2065.

Böhm, J., Frangakis, A. S., Hegerl, R., … Baumeister, W. (2000). Toward detecting and identifying macromolecules in a cellular context: Template matching applied to electron tomograms. *Proceedings of the National Academy of Sciences*, *97*(26), 14245 LP – 14250.

Boon, C. J. F., den Hollander, A. I., Hoyng, C. B., … Keunen, J. E. E. (2008). The spectrum of retinal dystrophies caused by mutations in the peripherin/RDS gene. *Progress in Retinal and Eye Research*, *27*(2), 213–235.

Briggman, K. L., & Bock, D. D. (2012). Volume electron microscopy for neuronal circuit reconstruction. *Current Opinion in Neurobiology*, *22*(1), 154–161.

Brilot, A. F., Chen, J. Z., Cheng, A., … Grigorieff, N. (2012). Beam-induced motion of vitrified specimen on holey carbon film. *Journal of Structural Biology*, *177*(3), 630–637.

Buchholz, T., Jordan, M., Pigino, G., & Jug, F. (2019). Cryo-CARE: Content-Aware Image Restoration for Cryo-Transmission Electron Microscopy Data. *2019 IEEE 16th International Symposium on Biomedical Imaging (ISBI 2019)*, 502–506.

Burbaum, L., Schneider, J., Scholze, S., … Jasnin, M. (2020). Molecular-scale visualization of sarcomere contraction within native cardiomyocytes. *BioRxiv*, 2020.09.09.288977.

Calvert, P. D., Govardovskii, V. I., Krasnoperova, N., … Makino, C. L. (2001). Membrane protein diffusion sets the speed of rod phototransduction. *Nature*, *411*(3), 90–94.

Chang, B., Hawes, N. L., Hurd, R. E., … Heckenlively, J. R. (2002). Retinal degeneration mutants in the mouse. *Vision Research*, *42*(4), 517–525.

Chang, B., Hawes, N. L., Hurd, R. E., … Heckenlively, J. R. (2005). Mouse models of ocular diseases. *Visual Neuroscience*, *22*(5), 587–593.

Cheng, A., Tan, Y. Z., Dandey, V. P., … Carragher, B. (2016). Strategies for Automated CryoEM Data Collection Using Direct Detectors. *Methods in Enzymology, 579, 87–102.*

Colville, C. A., & Molday, R. S. (1996). Primary Structure and Expression of the Human -Subunit and Related Proteins of the Rod Photoreceptor cGMP-gated Channel. *The Journal of Biological Chemistry*, *271*(51), 32968–32974.

Cong, Y., & Ludtke, S. J. (2010). Single Particle Analysis at High Resolution. *Methods in Enzymology, 482, 211–235.*

Corless, J. M., Fetter, R. D., Zampighi, O. B., … Wall-Buford, D. L. (1987). Structural features of the terminal loop region of frog retinal rod outer segment disk membranes: II. Organization of the terminal loop complex. *Journal of Comparative Neurology*, *257*(1), 9–23.

Corless, J. M., & Schneider, T. G. (1987). Patterns of interdisk connections within the lamellar domains of retinal rod outer segment disks: Observations relevant to the axial propagation of incisures. *Experimental Eye Research*, *45*(6), 883–905.

Cornell, C. E., Mileant, A., Thakkar, N., … Keller, S. L. (2020). Direct imaging of liquid domains in membranes by cryo-electron tomography. *Proceedings of the National Academy of Sciences*, *117*(33), 19713 LP – 19719.

Cox, J., Hein, M. Y., Luber, C. A., … Mann, M. (2014). Accurate Proteome-wide Label-free Quantification by Delayed Normalization and Maximal Peptide Ratio Extraction, Termed MaxLFQ. *Molecular &Amp; Cellular Proteomics*, *13*(9), 2513 LP – 2526.

Cox, J., & Mann, M. (2008). MaxQuant enables high peptide identification rates, individualized p.p.b.-range mass accuracies and proteome-wide protein quantification. *Nature Biotechnology*, *26*(12), 1367–1372.

Daiger, S. P., Sullivan, L. S., & Bowne, S. J. (2013). Genes and mutations causing retinitis pigmentosa. *Clinical Genetics*, *84*(2), 132–141.

Danev, R., & Baumeister, W. (2016). Cryo-EM single particle analysis with the Volta phase plate. *ELife*, *5*(e13046), 1–14.

Danev, R., & Baumeister, W. (2017). Expanding the boundaries of cryo-EM with phase plates. *Current Opinion in Structural Biology*, *46*, 87–94.

Danev, R., Buijsse, B., Khoshouei, M., … Baumeister, W. (2014). Volta potential phase plate for in-focus phase contrast transmission electron microscopy. *Proceedings of the National Academy of Sciences*, *111*(44), 15635–15640.

Dodonova, S. O., Aderhold, P., Kopp, J., … Briggs, J. A. G. (2017). 9Å structure of the COPI coat reveals that the Arf1 GTPase occupies two contrasting molecular environments. *ELife*, *6*, e26691.

Dubochet, J., Adrian, M., Chang, J. J., … Schultz, P. (1988). Cryo-electron microscopy of vitrified specimens. *Quarterly Reviews of Biophysics*, *21*(2), 129–228.

Erickson, H. P., Klug, A., Huxley, H. E., & Klug, A. (1971). Measurement and compensation of defocusing and aberrations by Fourier processing of electron micrographs. *Philosophical Transactions of the Royal Society of London. B, Biological Sciences*, *261*(837), 105–118.

Farber, D. B., Flannery, J. G., & Bowes-Rickman, C. (1994). The rd mouse story: Seventy years of research on an animal model of inherited retinal degeneration. *Progress in Retinal and Eye Research*, *13*(1), 31–64.

Fukuda, Y., Laugks, U., Lučić, V., … Danev, R. (2015). Electron cryotomography of vitrified cells with a Volta phase plate. *Journal of Structural Biology*, *190*, 143–154.

Gallagher, J. R., Kim, A. J., Gulati, N. M., & Harris, A. K. (2019). Negative-Stain Transmission Electron Microscopy of Molecular Complexes for Image Analysis by 2D Class Averaging. *Current Protocols in Microbiology*, *54*(1), e90.

Gao, Y., Hu, H., Ramachandran, S., … Skiniotis, G. (2019). Structures of the Rhodopsin-Transducin Complex: Insights into G-Protein Activation. *Molecular Cell*, *75*(4), 781-790.e3.

Glaeser, R. M. (2016). Specimen Behavior in the Electron Beam. *Methods in Enzymology, 579, 19–50*.

Goldberg, A. F. X., & Molday, R. S. (1996). Subunit Composition of the Peripherin/rds−Rom-1 Disk Rim Complex from Rod Photoreceptors: Hydrodynamic Evidence for a Tetrameric Quaternary Structure. *Biochemistry*, *35*(19), 6144–6149.

Goldberg, A. F. X., Moritz, O. L., & Williams, D. S. (2016). Molecular basis for photoreceptor outer segment architecture. In *Progress in Retinal and Eye Research* (Vol. 55, pp. 52–81). Pergamon.

Grant, T., & Grigorieff, N. (2015). Measuring the optimal exposure for single particle cryo-EM using a 2.6 Å reconstruction of rotavirus VP6. *ELife*, *4*, e06980–e06980.

Guizar-Sicairos, M., Thurman, S. T., & Fienup, J. R. (2008). Efficient subpixel image registration algorithms. *Optics Letters*, *33*(2), 156–158.

Gulati, S., Palczewski, K., Engel, A., … Kovacik, L. (2019). Cryo-EM structure of phosphodiesterase 6 reveals insights into the allosteric regulation of type I phosphodiesterases. *Science Advances*, *5*(2), eaav4322.

Gunkel, M., Schöneberg, J., Alkhaldi, W., … Al-Amoudi, A. (2015). Higher-order architecture of rhodopsin in intact photoreceptors and its implication for phototransduction kinetics. *Structure (London, England : 1993)*, *23*(4), 628–638.

Hagen, W. J. H., Wan, W., & Briggs, J. A. G. (2017). Implementation of a cryo-electron tomography tilt-scheme optimized for high resolution subtomogram averaging. *Journal of Structural Biology*, *197*(2), 191–198.

Harauz, G., & van Heel, M. (1986). Exact Filters for General Geometry Three Dimensional Reconstruction. *Optik*, *78*(4), 146–156.

Heberle, F. A., Doktorova, M., Scott, H. L., … Levental, I. (2020). Direct label-free imaging of nanodomains in biomimetic and biological membranes by cryogenic electron microscopy. *Proceedings of the National Academy of Sciences*, *117*(33), 19943 LP – 19952.

Hollingsworth, S. A., & Dror, R. O. (2018). Molecular Dynamics Simulation for All. *Neuron*, *99*(6), 1129–1143.

Hrabe, T., Chen, Y., Pfeffer, S., … Förster, F. (2012). PyTom: A python-based toolbox for localization of macromolecules in cryo-electron tomograms and subtomogram analysis. *Journal of Structural Biology*, *178*(2), 177–188.

Hüttl, S., Michalakis, S., Seeliger, M., … Biel, M. (2005). Impaired Channel Targeting and Retinal Degeneration in Mice Lacking the Cyclic Nucleotide-Gated Channel Subunit CNGB1. *The Journal of Neuroscience*, *25*(1), 130–138.

Ingram, N. T., Sampath, A. P., & Fain, G. L. (2016). Why are rods more sensitive than cones? *The Journal of Physiology*, *594*(19), 5415–5426.

Jarsch, I. K., Daste, F., & Gallop, J. L. (2016). Membrane curvature in cell biology: An integration of molecular mechanisms. *The Journal of Cell Biology*, *214*(4), 375–387.

Kang, Y., Zhou, X. E., Gao, X., … Xu, H. E. (2015). Crystal structure of rhodopsin bound to arrestin by femtosecond X-ray laser. *Nature*, *523*(7562), 561–567.

Kevany, B. M., Tsybovsky, Y., Campuzano, I. D. G., … Palczewski, K. (2013). Structural and functional analysis of the native peripherin-ROM1 complex isolated from photoreceptor cells. *The Journal of Biological Chemistry*, *288*(51), 36272–36284.

Körschen, H. G., Beyermann, M., Müller, F., … Kaupp, U. B. (1999). Interaction of glutamic-acid-rich proteins with the cGMP signalling pathway in rod photoreceptors. *Nature*, *400*(6746), 761–766.

Koster, A. J., Grimm, R., Typke, D., … Baumeister, W. (1997). Perspectives of Molecular and Cellular Electron Tomography. *Journal of Structural Biology*, *120*(3), 276–308.

Kremer, J. R., Mastronarde, D. N., & McIntosh, J. R. (1996). Computer Visualization of Three-Dimensional Image Data Using IMOD. *Journal of Structural Biology*, *116*(1), 71–76.

Krivanek, O. L., & Mooney, P. E. (1993). Applications of slow-scan CCD cameras in transmission electron microscopy. *Ultramicroscopy*, *49*(1), 95–108.

Kwok, M. C. M., Holopainen, J. M., Molday, L. L., … Molday, R. S. (2008). Proteomics of Photoreceptor Outer Segments Identifies a Subset of SNARE and Rab Proteins Implicated in Membrane Vesicle Trafficking and Fusion. *Molecular &Amp; Cellular Proteomics*, *7*(6), 1053–1066.

Lenz, F. A. (1971). Transfer of Image Information in the Electron Microscope. In *Electron Microscopy in Material Science* (pp. 538–569).

Li, X., Mooney, P., Zheng, S., … Cheng, Y. (2013). Electron counting and beam-induced motion correction enable near-atomic-resolution single-particle cryo-EM. *Nature Methods*, *10*(6), 584–590.

Liang, Y., Fotiadis, D., Maeda, T., … Palczewski, K. (2004). Rhodopsin signaling and organization in heterozygote rhodopsin knockout mice. *The Journal of Biological Chemistry*, *279*(46), 48189–48196.

Loewen, C. J., Moritz, O. L., & Molday, R. S. (2001). Molecular characterization of peripherin-2 and rom-1 mutants responsible for digenic retinitis pigmentosa. *The Journal of Biological Chemistry*, *276*(25), 22388–22396.

Loewen, C. J. R., & Molday, R. S. (2000). Disulfide-mediated oligomerization of peripherin/Rds and Rom-1 in photoreceptor disk membranes. *The Journal of Biological Chemistry*, *275*(8), 5370–5378.

Lučić, V., Fernández-Busnadiego, R., Laugks, U., & Baumeister, W. (2016). Hierarchical detection and analysis of macromolecular complexes in cryo-electron tomograms using Pyto software. *Journal of Structural Biology*, *196*, 503–514.

Mahamid, J., Pfeffer, S., Schaffer, M., … Baumeister, W. (2016). Visualizing the molecular sociology at the HeLa cell nuclear periphery. *Science*, *351*(6276), 969–972.

Mahamid, J., Schampers, R., Persoon, H., … Plitzko, J. M. (2015). A focused ion beam milling and lift-out approach for site-specific preparation of frozen-hydrated lamellas from multicellular organisms. *Journal of Structural Biology*, *192*(2), 262–269.

Makino, C. L., Wen, X. H., Michaud, N. A., … Caruso, G. (2012). Rhodopsin expression level affects rod outer segment morphology and photoresponse kinetics. *PloS One*, *7*(5), e37832.

Marko, M., Hsieh, C., Moberlychan, W., … Frank, J. (2006). Focused ion beam milling of vitreous water: prospects for an alternative to cryo-ultramicrotomy of frozen-hydrated biological samples. *Journal of Microscopy*, *222*(1), 42–47.

Marko, M., Hsieh, C., Schalek, R., … Mannella, C. (2007). Focused-ion-beam thinning of frozen-hydrated biological specimens for cryo-electron microscopy. *Nature Methods*, *4*(3), 215–217.

Martinez-Sanchez, A., Garcia, I., Asano, S., … Fernandez, J. J. (2014). Robust membrane detection based on tensor voting for electron tomography. *Journal of Structural Biology*, *186*(1), 49–61.

Martinez-Sanchez, A., Kochovski, Z., Laugks, U., … Lučić, V. (2020). Template-free detection and classification of membrane-bound complexes in cryo-electron tomograms. *Nature Methods*, *17*(2), 209–216.

Mastronarde, D. N. (2005). Automated electron microscope tomography using robust prediction of specimen movements. *Journal of Structural Biology*, *152*, 36–51.

Mastronarde, D. N., & Held, S. R. (2017). Automated tilt series alignment and tomographic reconstruction in IMOD. *Journal of Structural Biology*, *197*(2), 102–113.

Mattila, P. K., Pykäläinen, A., Saarikangas, J., … Lappalainen, P. (2007). Missing-in-metastasis and IRSp53 deform PI(4,5)P2-rich membranes by an inverse BAR domain-like mechanism. *The Journal of Cell Biology*, *176*(7), 953–964.

McDonald, K., Schwarz, H., Müller-Reichert, T., … Morphew, M. (2010). Chapter 28 - “Tips and Tricks” for High-Pressure Freezing of Model Systems. In T. B. T.-M. in C. B. Müller-Reichert (Ed.), *Electron Microscopy of Model Systems* (Vol. 96, pp. 671–693). Academic Press.

McMullan, G., Faruqi, A. R., & Henderson, R. (2016). Direct Electron Detectors. *Methods in Enzymology, 579, 1–17.*

Meyer, F. (1994). Topographic distance and watershed lines. *Signal Processing*, *38*(1), 113–125.

Milestones in light microscopy. (2009). *Nature Cell Biology*, *11*(10), 1165.

Mitra, K., Ubarretxena-Belandia, I., Taguchi, T., … Engelman, D. M. (2004). Modulation of the bilayer thickness of exocytic pathway membranes by membrane proteins rather than cholesterol. *Proceedings of the National Academy of Sciences*, *101*(12), 4083 LP – 4088.

Molday, R. S., Hicks, D., & Molday, L. L. (1987). Peripherin. A rim-specific membrane protein of rod outer segment discs. *Investigative Ophthalmology & Visual Science*, *28*(1), 50–61.

Monje-Galvan, V., & Klauda, J. B. (2016). Peripheral membrane proteins: Tying the knot between experiment and computation. *Biochimica et Biophysica Acta (BBA) - Biomembranes*, *1858*(7, Part B), 1584–1593.

Moor, H. (1987). Cryotechniques in Biological Electron Microscopy. In *Theory and Practice of High Pressure Freezing* (pp. 175–191).

Nickell, S., Förster, F., Linaroudis, A., … Plitzko, J. M. (2005). TOM software toolbox: acquisition and analysis for electron tomography. *Journal of Structural Biology*, *149*(3), 227–234.

Nickell, S., Park, P. S. H., Baumeister, W., & Palczewski, K. (2007). Three-dimensional architecture of murine rod outer segments determined by cryoelectron tomography. *The Journal of Cell Biology*, *177*(5), 917–925.

Orlova, E. . V., & Saibil, H. R. (2011). *Structural Analysis of Macromolecular Assemblies by Electron Microscopy*. 7710–7748.

Palczewski, K. (2006). G protein-coupled receptor rhodopsin. *Annual Review of Biochemistry*, *75*, 743–767.

Papermaster, D. S., Schneider, B. G., Zorn, M. A., & Kraehenbuhl, J. P. (1978). Immunocytochemical localization of a large intrinsic membrane protein to the incisures and margins of frog rod outer segment disks. *The Journal of Cell Biology*, *78*(2), 415–425.

Passmore, L. A., & Russo, C. J. (2016). Specimen Preparation for High-Resolution Cryo-EM. *Methods in Enzymology, 579, 51–86.*

Pettersen, E. F., Goddard, T. D., Huang, C., … Meng, E. (2004). UCSF Chimera-A visualization system for exploratory research and analysis. *J Comput Chem*, *25*(13), 1605–1612.

Plitzko, J., & Baumeister, W. (2019). Cryo-Electron Tomography. In *Handbook of Microscopy* (pp. 189–228).

Poetsch, A., Molday, L. L., & Molday, R. S. (2001). The cGMP-gated Channel and Related Glutamic Acid-rich Proteins Interact with Peripherin-2 at the Rim Region of Rod Photoreceptor Disc Membranes. *The Journal of Biological Chemistry*, *276*(51), 48009–48016.

Poincelot, R. P., & Abrahamson, E. W. (1970). Fatty acid composition of bovine rod outer segments and rhodopsin. *Biochimica et Biophysica Acta (BBA) - Lipids and Lipid Metabolism*, *202*(2), 382–385.

Pollard, T. D. (2016). Actin and Actin-Binding Proteins. *Cold Spring Harbor Perspectives in Biology*, *8*(8), a018226.

Pugh, E. N., & Lamb, T. D. (2000). Phototransduction in vertebrate rods and cones: Molecular mechanisms of amplification, recovery and light adaptation. In D. G. Stavenga, W. J. DeGrip, & E. N. Pugh (Eds.), *Molecular Mechanisms in Visual Transduction* (Vol. 3, pp. 183–255). Elsevier Science.

Reimer, L. (1984). *Transmission Electron Microscopy*.

Rigort, A., Bäuerlein, F. J. B., Laugks, T., … Plitzko, J. M. (2010). A 360° Rotatable Cryo-FIB Stage for Micromachining Frozen-Hydrated Specimens for Cryo-Electron Tomography. *Microscopy and Microanalysis*, *16*(S2), 220–221.

Rigort, A., Bäuerlein, F. J. B., Leis, A., … Plitzko, J. M. (2010). Micromachining tools and correlative approaches for cellular cryo-electron tomography. *Journal of Structural Biology*, *172*(2), 169–179.

Ripstein, Z. A., & Rubinstein, J. L. (2016). Processing of Cryo-EM Movie Data. *Methods in Enzymology, 579, 103–124.*

Robertson, J. D. (1965). A possible ultrastructural Correlate of Function in the Frog Retinal Rod. *Proceedings of the National Academy of Sciences of the United States of America*, *53*(4), 860–866.

Roof, D. J., & Heuser, J. E. (1982). Surfaces of rod photoreceptor disk membranes: integral membrane components. *The Journal of Cell Biology*, *95*(2), 487–500.

Rosenthal, P. B., & Henderson, R. (2003). Optimal Determination of Particle Orientation, Absolute Hand, and Contrast Loss in Single-particle Electron Cryomicroscopy. *Journal of Molecular Biology*, *333*(4), 721–745.

Ruska, E. (1980). The early development of electron lenses and electron microscopy. *Microscopica Acta. Supplement*, *Suppl 5*, 1–140.

Schaffer, M., Mahamid, J., Engel, B. D., … Plitzko, J. M. (2017). Optimized cryo-focused ion beam sample preparation aimed at in situ structural studies of membrane proteins. *Journal of Structural Biology*, *197*(2), 73–82.

Schaffer, M., Pfeffer, S., Mahamid, J., … Plitzko, J. M. (2019). A cryo-FIB lift-out technique enables molecular-resolution cryo-ET within native Caenorhabditis elegans tissue. *Nature Methods*, *16*(8),

Scheres, S. H. W. (2016). Processing of Structurally Heterogeneous Cryo-EM Data in RELION. *Methods in Enzymology, 579, 125–157.*

Schertel, A., Snaidero, N., Han, H. M., … Möbius, W. (2013). Cryo FIB-SEM: Volume imaging of cellular ultrastructure in native frozen specimens. *Journal of Structural Biology*, *184*(2), 355–360.

Scherzer, O. (1949). The Theoretical Resolution Limit of the Electron Microscope. *Journal of Applied Physics*, *20*(1), 20–29.

Schindelin, J., Arganda-Carreras, I., Frise, E., … Cardona, A. (2012). Fiji: an open-source platform for biological-image analysis. *Nature Methods*, *9*(7), 676–682.

Schur, F. K. M., Obr, M., Hagen, W. J. . H., … Briggs, J. A. G. (2016). An atomic model of HIV-1 capsid-SP1 reveals structures regulating assembly and maturation. *Science (New York, N.Y.)*, *353*(6298), 506–508.

Singh, P., Wang, B., Maeda, T., … Tesmer, J. J. G. (2008). Structures of rhodopsin kinase in different ligand states reveal key elements involved in G protein-coupled receptor kinase activation. *The Journal of Biological Chemistry*, *283*(20), 14053–14062.

Sjöstrand, F. S. (1949). An electron microscope study of the retinal rods of the guinea pig eye. *Journal of Cellular and Comparative Physiology*, *33*(3), 383–403.

Sjöstrand, F. S. (1953). The ultrastructure of the outer segments of rods and cones of the eye as revealed by the electron microscope. *Journal of Cellular and Comparative Physiology*, *42*(1), 15–44.

Skiba, N. P., Spencer, W. J., Salinas, R. Y., … Arshavsky, V. Y. (2013). Proteomic Identification of Unique Photoreceptor Disc Components Reveals the Presence of PRCD, a Protein Linked to Retinal Degeneration. *Journal of Proteome Research*, *12*(6), 3010–3018.

Tegunov, D., & Cramer, P. (2019). Real-time cryo-electron microscopy data preprocessing with Warp. *Nature Methods*, *16*(11), 1146–1152.

Tegunov, D., Xue, L., Dienemann, C., … Mahamid, J. (2020). Multi-particle cryo-EM refinement with M visualizes ribosome-antibiotic complex at 3.7 Å inside cells. *BioRxiv*, 2020.06.05.136341.

Teller, D. C., Okada, T., Behnke, C. A., … Stenkamp, R. E. (2001). Advances in Determination of a High-Resolution Three-Dimensional Structure of Rhodopsin, a Model of G-Protein-Coupled Receptors (GPCRs). *Biochemistry*, *40*(26), 7761–7772.

Thon, F. (1966). Zur Defokussierungsabhängigkeit des Phasenkontrastes bei der elektronenmikroskopischen Abbildung. *Naturforschg.*, *21a*, 476–478.

Tinsley, J. N., Molodtsov, M. I., Prevedel, R., … Vaziri, A. (2016). Direct detection of a single photon by humans. *Nature Communications*, *7*.

Tivol, W. F., Briegel, A., & Jensen, G. J. (2008). An Improved Cryogen for Plunge Freezing. *Microscopy and Microanalysis*, *14*(5), 375–379.

Townes-Anderson, E., Dacheux, R. F., & Raviola, E. (1988). Rod photoreceptors dissociated from the adult rabbit retina. *The Journal of Neuroscience*, *8*(1), 320 LP – 331.

Trinick, J., & Berriman, J. (1987). Zero-loss electron microscopy with the Zeiss EM902. *Ultramicroscopy*, *21*(4), 393–397.

Tsybovsky, Y., Orban, T., Molday, R. S., … Palczewski, K. (2013). Molecular Organization and ATP-Induced Conformational Changes of ABCA4, the Photoreceptor-Specific ABC Transporter. *Structure*, *21*(5), 854–860.

Tsybovsky, Y., & Palczewski, K. (2014). Expression, purification and structural properties of ABC transporter ABCA4 and its individual domains. *Protein Expression and Purification*, *97*, 50–60.

Turk, M., & Baumeister, W. (2020). The promise and the challenges of cryo-electron tomography. *FEBS Letters*, *594*(20), 3243–3261.

Turoňová, B., Hagen, W. J. H., Obr, M., … Beck, M. (2020). Benchmarking tomographic acquisition schemes for high-resolution structural biology. *Nature Communications*, *11*(1), 876.

Turoňová, B., Marsalek, L., & Slusallek, P. (2016). On geometric artifacts in cryo electron tomography. *Ultramicroscopy*, *163*, 48–61.

Wan, W., & Briggs, J. A. G. (2016). Cryo-Electron Tomography and Subtomogram Averaging. *Methods in Enzymology*, *579*, 329–367.

Wan, W., Kolesnikova, L., Clarke, M., … Briggs, J. A. G. (2017). Structure and assembly of the Ebola virus nucleocapsid. *Nature*, *551*, 394–397.

Weng, J., Mata, N. L., Azarian, S. M., … Travis, G. H. (1999). Insights into the Function of Rim Protein in Photoreceptors and Etiology of Stargardt's Disease from the Phenotype in abcr Knockout Mice. *Cell*, *98*(1), 13–23.

Wilkins, M. H., Blaurock, A. E., & Engelman, D. M. (1971). Bilayer structure in membranes. *Nature: New Biology*, *230*(11), 72–76.

Williams, D. B., & Carter, C. B. (2009). *Transmission Electron Microscopy*.

Winey, M., Meehl, J. B., O'Toole, E. T., & Giddings, T. H. (2014). Conventional transmission electron microscopy. *Molecular Biology of the Cell*, *25*(3), 319–323.

Won, J., Shi, L. Y., Hicks, W., … Nishina, P. (2011). Mouse Model Resources for Vision Research. *Journal of Ophthalmology*, *2011*, 391384.

Zhang, K. (2016). Gctf: Real-time CTF determination and correction. *Journal of Structural Biology*, *193*(1), 1–12.

Zhang, Y., Molday, L. L., Molday, R. S., … Pittler, S. J. (2009). Knockout of GARPs and the β-subunit of the rod cGMP-gated channel disrupts disk morphogenesis and rod outer segment structural integrity. *Journal of Cell Science*, *122*(8), 1192–1200.

Zhao, D. Y., Pöge, M., Morizumi, T., … Palczewski, K. (2019). Cryo-EM structure of the native rhodopsin dimer in nanodiscs. *The Journal of Biological Chemistry*, *294*(39), 14215–14230.

Zhao, H., & Lappalainen, P. (2012). A simple guide to biochemical approaches for analyzing protein-lipid interactions. *Molecular Biology of the Cell*, *23*(15), 2823–2830.

Zheng, S. Q., Palovcak, E., Armache, J. P., … Agard, D. A. (2017). MotionCor2: anisotropic correction of beam-induced motion for improved cryo-electron microscopy. *Nature Methods*, *14*(4), 331–332.

Zhou, W., Apkarian, R. P., Wang, Z. L., & Joy, D. (2006). Fundamentals of Scanning Electron Microscopy (SEM). In Z. Weilie & L. W. Zhong (Eds.), *Scanning Microscopy for Nanotechnology* (pp. 1–39).

5.3 Acknowledgement

I always had a drive to understand living things, ideally by looking at them. My studies led me to cryo-ET, a fascinating method for exactly that, and I have been lucky in getting to learn it from the best, in the best imaginable environment. Now that my PhD is approaching its end, I am looking back on this amazing journey that was only possible with the help of many people. This section is devoted to them.

First and foremost, I want to thank Prof. Dr. Wolfgang Baumeister for giving me the opportunity to work in his department. Despite all his responsibilities, he never lost track of me and helped me when needed. Working in his lab has provided me with great microscope access and a network of talented co-workers, with vast depths of knowledge that they kindly shared with me. I, especially, want to thank my amazing advisors Dr. Julia Mahamid and Prof. Dr. Jürgen Plitzko. They took the time to explain to me the basics of EM directly at the instruments, which for me is the most productive way of learning. They gave me the opportunity to grow at my own pace without ever pressuring me and were always there when I needed guidance.

Many thanks to Dr. Philipp Erdmann, Günter Pfeifer and Dr. Miroslava Schaffer for support at the microscopes, allowing me to develop the confidence required to work with the machines independently. I would also like to thank Dr. Antonio Martinez-Sanchez who wrote scripts adapted to my needs and kindly shared his expertise with me. I am grateful to Dr. Vladan Lučić who helped me with all my segmentation problems along the way, and to Florian Beck for answering all kinds of data processing-related questions. Thanks to Dr. William Wan and Sagar Khavnekar for progressively improving the Tomoman and the Stopgap software, making our lives so much easier. I am also thankful to Dr. Andreas Schweizer and Dr. Marius Boicu, for all their help with the wet lab work. I would like to thank Birgit Book for her help with administrative tasks, Inga Wolf for hard- and software support and the workshop of the Baumeister department for the supply with in-house fabricated cryo-EM tools.

Additionally, I want to thank the animal- and the mass spectrometry facilities of the Max Planck Institute of Biochemistry for their great support with the animals and the proteomics measurements, respectively. Many thanks to Dr. Iuliia Iermak, Oda Schiøtz and Sven Klumpe for suffering through the first clumsy draft of this work. Without their productive feedback and discussions this thesis would not have become readable.

This project is a collaborative effort with immense contributions from other institutes. I am grateful to Prof. Dr. Krzysztof Palczewski and his group (UCI, California, USA), who are experts in the field of eye research and welcomed me several times in their lab to learn and share experience. Especially, I want to thank Dr. Sanae Sakami (Case Western Reserve University, Ohio, USA) for teaching me her gentle ROS extraction method and to Dr. David Salom (UCI, California, USA) for providing me with the protocol for the western blots against PDE6. I also want to thank Dr. Andreas Schertel (Carl Zeiss SMT, Oberkochen, Germany) for help with acquiring the serial milling and block face imaging data.

Of course, there are many more people to thank for all the fruitful discussions, help at the microscopes, hat crafting sessions, amazing lunch breaks, volleyball trainings and all the social activities that made my PhD an amazing, unforgettable experience. As this would make this a never-ending section, it will have to suffice to thank the Baumeister department and the people of the Max Planck Institute of

Biochemistry. It was my first time further away from home and I never really warmed up to the city of Munich. You people, however, welcomed me, made me comfortable and gave me the feeling of having arrived. Power to the Unicorns!

Finally, I want to thank my family. Even though none of them have scientific background, they have been fully supportive of me and my academic pursuits. Thank you all so much :-)